Study of the Decay $D^0 \rightarrow K^+\pi^-$ in FOCUS

By

Jonathan Marion Link
B.S. (University of California, Davis) 1993
M.S. (University of California, Davis) 1995

DISSERTATION

Submitted in partial satisfaction of the requirements for the degree of

DOCTOR OF PHILOSOPHY

in

Physics

in the

OFFICE OF GRADUATE STUDIES

of the

UNIVERSITY OF CALIFORNIA

DAVIS

Approved:

Prof. Philip Yager, Chair
Prof. Richard Lander
Prof. Steven Carlip

Committee in Charge

2001

Abstract

We present a study of the decay $D^0 \to K^+\pi^-$. Using a large sample of photoproduced charm mesons from the FOCUS experiment at Fermilab (FNAL-E831), we observe the decay $D^0 \to K^+\pi^-$ with a signal yield of 149 ± 31 events compared to an identically selected sample consisting of $36\,760 \pm 195$ $D^0 \to K^-\pi^+$ events. We measure the branching ratio of $D^0 \to K^+\pi^-$ to $D^0 \to K^-\pi^+$ to be $(0.404 \pm 0.085 \pm 0.025)\%$. We derive a relationship between the observed ratio and the doubly Cabibbo suppressed branching ratio for an arbitrary $D^0 - \overline{D}^0$ mixing model which is based on the acceptance of $K\pi$ events in the analysis. Using this relationship the data is split into high and low lifetime samples to obtain limits on the mixing parameter y' of $-0.130 < y' < 0.006$

To Theresa, Zachary, Nicholas and Baby

Acknowledgements

The success of the FOCUS experiment is due to many people and I would like to take this opportunity to thank each member of the FOCUS Collaboration for their dedicated effort. In addition several technicians and engineers, both at the lab and at collaborating institutions, are deserving of high praise and admiration. Thank you all, and I look forward to working with many of you in our future endeavors.

Within this group, several individuals must be singled out for their extraordinary contributions to the success of the experiment.

First, I'd like to recognize Francesco Prelz, Art Kreymer, Matteo Boschini and the rest of the DART team for designing and maintaining the data acquisition system, the heart of the experiment. Without their Herculean efforts shift taking would have been a nightmare.

Thanks to Marek Hamela who designed and built the straw tube detectors with a rag-tag band of clever undergraduate students.

Special thanks to Roy Justice for saving the straw project with his flawless cable repair effort. It went above and beyond the call of duty.

Thanks to John Cumalat and Luigi Moroni for their wise leadership, guiding through a successful data taking run and hopefully an even more successful run of physics analysis and publication.

There are many people whose sage advise, good counsel, and timely physics tutorials have been invaluable to me. Most notably Jim Wiss, Will Johns, Daniele Pedrini, Joel Butler, Harry Cheung, Luigi Moroni, John Cumalat, Peter Garbincius and Peter Kasper. Thank you!

I'd like to thank my paper review committee for their efforts in preparing this physics for publication: Paul Sheldon, Doris Kim, Joel Butler and Rob Kutschke. Also, thank you to Brian O'Reilly, Eric Vaandering, Kevin Stenson, and Peter Garbincius for carefully reading and commenting on the various versions of the draft paper.

Thanks to the whole Fermilab group for taking me in as one of their own, and giving me a safe place to test out all of my ideas and the feedback I needed to make them better.

I'd like to thank my fellow FOCUS graduate students for their support, friendship and shared experiences. Thanks to Eric Vaandering, Kevin Stenson, Topher Cawlfield, Amir Rahimi, Mike Hosak, Dan Engh, Paolo Dini, Maro Merlo, Eduardo Ramirez and Germano Bonomi.

Beyond the FOCUS collaboration, there are many people who helped to make my young physics experience great.

Thanks to Peter Klavins and Robert Shelton, for introducing me to the world of physics research and giving me my first job in physics.

Thanks to everyone in my graduate student class. Those first two years were a lot of work and I'm glad that we did it together. I'd especially like to thank my regular study partners and office mates: Dave Everitt, Gus Hart, John Pask, Pat Hession, Matt Enjalran, Anita Landon, Tom Gutierrez and Bill Caskey.

The physics department staff has always been helpful and supportive. In particular, thanks to Anneke Balics, Diane Vandepeute, Mary Reid and Lynn Rabena.

Thanks to the members of the UC Davis high energy group for their support and friendship. I'd especially like to thank Dick Lander for getting me started in HEP with his introductory course and by giving me a job that allowed me to do real high energy research.

I'd like to thank Phil Yager, for his endless support both financial and moral. Phil introduced me to perhaps the best group of scientific collaborators possible, and for that I am grateful. With his charm and personality, Phil cultivates tremendous working relationships with people throughout the lab and university. This has been a tremendous advantage to me both as a role model and as a positive introduction to people who have been extremely helpful.

Finally, thanks to my parents Bob and Nancy Link, for always believing in me even when I was no longer able to explain to them what I was doing. To my wife Theresa, who is always supportive and who was most affected by my decision to go to graduate school, move to Illinois and so on. I love you. And to my sons Zachary and Nicholas. I love you both.

Contents

List of Tables

List of Figures

Chapter 1

Physics Introduction

The decay $D^0 \to K^+\pi^-$ [1] may occur either through a rare process known as doubly Cabibbo suppressed decay, or by mixing to a $\overline{D}^0$ followed by the Cabibbo favored decay $\overline{D}^0 \to K^+\pi^-$. This chapter will discuss the theoretical foundation for these phenomena and review the relevant experimental evidence.

1.1 Hadronic Decays of Charm Mesons

Ground state mesons with non-zero flavor quantum numbers (like D mesons) decay via the weak force. These decays are mediated by $W^\pm$ bosons. Flavor changing decays with Z^0 bosons are subjected to a large cancellation known as the GIM mechanism [1]. The dominant weak interaction vertices involved in the decay of

[1] The charge conjugate mode will be implicitly included unless otherwise stated.

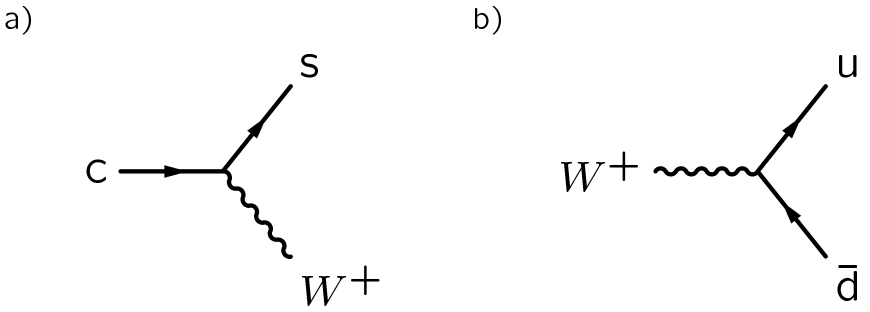

Figure 1.1: The Cabibbo favored weak vertices relevant for charm quark decays. **a)** The charm decay vertex and **b)** the W decay vertex.

the charm quark are shown in Figure 1.1.

The charm (c) quark decays into a down-type quark (either a strange s or down d quark) and a W boson as shown in Figure 1.1a. Transitions to the s quark — partner to the c in the second generation — are observed much more frequently than transitions to the lighter d quark of the first generation. This suppression of transitions between second and first generations is called Cabibbo suppression for Nicola Cabibbo who first parameterized the relative rate of $\Delta s = 1$ to $\Delta s = 0$ transitions with the angle $\theta_{\mathrm{C}} \simeq 0.22$ [2]. In the Standard Model (SM) these transitions between quark generations are attributed to quark mixing. This mixing occurs because the quark flavor eigenstates and mass eigenstates do not coincide. The flavor and mass eigenstates are related by a rotation in flavor space which, by convention, acts on the down-type quarks:

$$\begin{pmatrix} d' \\ s' \end{pmatrix} = \begin{pmatrix} \cos\theta_{\mathrm{C}} & \sin\theta_{\mathrm{C}} \\ -\sin\theta_{\mathrm{C}} & \cos\theta_{\mathrm{C}} \end{pmatrix} \begin{pmatrix} d \\ s \end{pmatrix}. \tag{1.1}$$

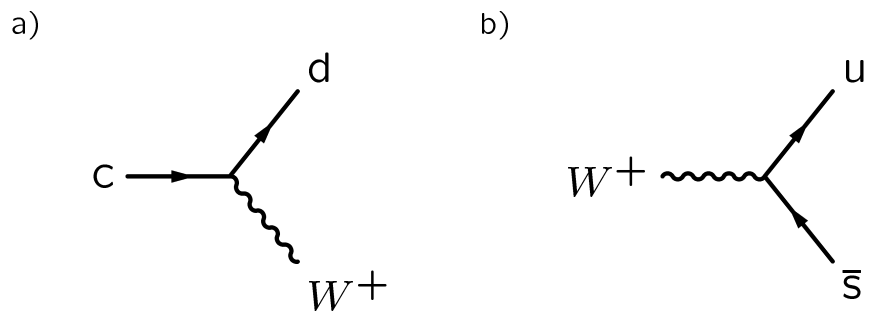

Figure 1.2: The Cabibbo suppressed weak vertices relevant for charm quark decays. **a)** The charm decay vertex and **b)** the W decay vertex.

In this model, the decay rate (which is proportional to the amplitude squared) for a Cabibbo suppressed decay relative to the topologically identical[2] Cabibbo favored (CF) decay goes as $\tan^2\theta_\mathrm{C}$. The Cabibbo suppressed weak vertices are shown in Figure 1.2. Decays in which both vertices are suppressed (such as $D^0 \to K^+\pi^-$) are known as doubly Cabibbo suppressed (DCS) decays, and have an expected decay rate relative to similar CF decays of $\tan^4\theta_\mathrm{C} \simeq 0.25\%$.

The four lowest order charm meson decay diagrams are shown in Figure 1.3. Figures 1.3a and b are known as spectator diagrams since the light quark does not participate. Figure 1.3b is suppressed by a factor of one third with respect to Figure 1.3a due to the requirement to match color with the external quarks. Figure 1.3c is a W boson exchange diagram, which is only possible for neutral D mesons. The quark annihilation diagram (Figure 1.3d) is only possible for charged D mesons. In addition to being Cabibbo suppressed for the $D^\pm$, annihilation is

[2] "Topologically identical" refers to a decay with the same Feynman diagrams but different final state quarks.

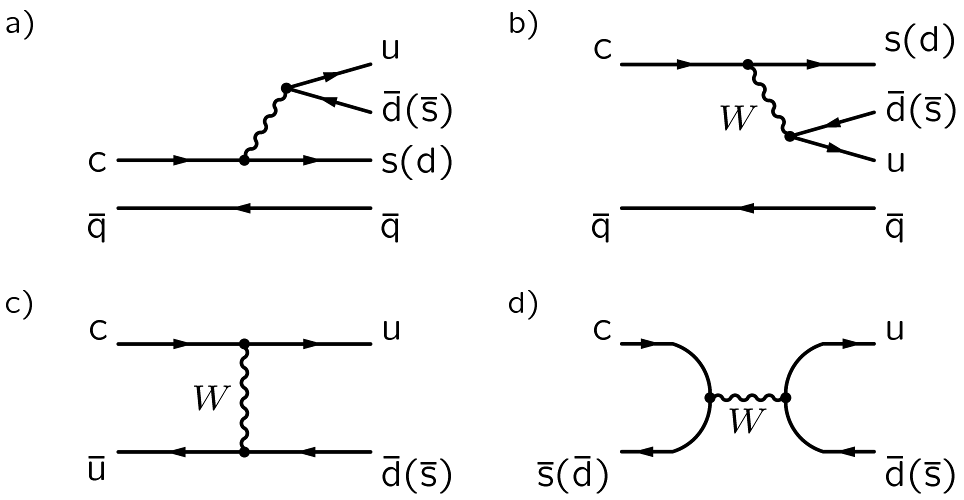

Figure 1.3: The lowest order Feynman diagrams for charm meson decay processes: **a)** external W boson emission, **b)** internal W emission, **c)** W boson exchange, and **d)** quark annihilation. Quarks associated with the Cabibbo suppressed processes are shown in parentheses.

also suppressed by helicity considerations. Figures 1.3a and c are the diagrams that may contribute to the decay $D^0 \to K^+\pi^-$.

1.1.1 Observations and Measurements of DCS Decays

Only two DCS decay modes have been reliably observed and reported in the literature. The decay $D^+ \to K^+\pi^-\pi^+$ was the first DCS mode to be reported. Originally observed by E687 [3], this decay mode is now well established and has been observed by at least two additional groups. The Particle Data Group (PDG) average for the $D^0 \to K^+\pi^-$ branching ratio relative to the CF decay, $D^+ \to K^-\pi^+\pi^+$ is $(0.75 \pm 0.16)\%$ or about $3\tan^4\theta_C$.

The second established DCS mode is $D^0 \to K^+\pi^-$. Prior to this study,

Table 1.1: Measurements of R_{DCS} with the assumption of no charm mixing and no CP violation.

Experiment	R_{DCS} (%) no Mixing	Events
CLEO [4]	$0.77 \pm 0.25 \pm 0.25$	19.1
E791 [5]	$0.68^{+0.34}_{-0.33} \pm 0.07$	34
Aleph [6]	$1.77^{+0.60}_{-0.56} \pm 0.31$	21.3
CLEO II.V [7]	$0.332^{+0.063}_{-0.065} \pm 0.040$	44.8
World Average PDG'00 [8]	0.38 ± 0.08	–

measurements of the DCS to CF branching ratio in this mode (R_{DCS}) had been reported by four groups. These measurements are listed in Table 1.1. Only the most recent result of CLEO II.V [7] is statistically significant and, in addition, the three earlier results are all higher than the world average by as much as $2\,\sigma$, which suggests a possible systematic problem with the earlier observations. In Section 6.1.3 we will examine several sources of background that can mimic the DCS signal and cause systematically high branching ratio measurements.

A preliminary observation of a third DCS decay $D^+ \to K^+K^-K^+$ mode has been reported by FOCUS [9].

1.1.2 Weak Decays in a Six Quark Theory

An extension of the quark mixing matrix to three quark generations was first proposed by Kobayashi and Maskawa [10]. This matrix is known as the the CKM matrix:

$$\begin{pmatrix} d' \\ s' \\ b' \end{pmatrix} = \begin{pmatrix} V_{ud} & V_{us} & V_{ub} \\ V_{cd} & V_{cs} & V_{cb} \\ V_{td} & V_{ts} & V_{tb} \end{pmatrix} \begin{pmatrix} d \\ s \\ b \end{pmatrix}, \tag{1.2}$$

where V_{ij} is the factor multiplying the amplitude for a weak vertex that involves quarks i and j. A useful parameterization for the CKM matrix comes from Wolfenstein [11]:

$$\mathbf{V}_{\text{CKM}} = \begin{pmatrix} 1-\lambda^2/2 & \lambda & A\lambda^3(\rho - i\eta) \\ -\lambda & 1-\lambda^2/2 & A\lambda^2 \\ A\lambda^3(1-\rho-i\eta) & -A\lambda^2 & 1 \end{pmatrix} \tag{1.3}$$

shown to order λ^3. In the Wolfenstein parameterization the strength of the matrix elements are expressed in powers of $\lambda = \sin\theta_{\text{C}}$. The three remaining parameters (A, ρ and η) are real numbers intended to be of order one.

1.2 D^0–$\overline{D}^0$ Mixing

The second path for the decay $D^0 \to K^+\pi^-$ is for the D^0 to change into a $\overline{D}^0$ through a process known as mixing. Then the $\overline{D}^0$ decays through the CF channel to $K^+\pi^-$. This process has not yet been unambiguously observed for the D^0, but it is well established in the neutral kaon system.

Mixing occurs because the neutral D mass eigenstates (or CP eigenstates in the limit of CP conservation) from which the mesons decay do not coincide with the flavor eigenstates at which they are produced. The flavor eigenstates, D^0 and $\overline{D}^0$, have the same mass and width, while the CP eigenstates may have slightly different masses and widths. The strength of mixing rate is determined by the size of the mass and width differences (Δm and $\Delta\Gamma$ respectively):

$$R_{\text{mix}} = \frac{1}{2}\left[\left(\frac{\Delta m}{\Gamma}\right)^2 + \left(\frac{\Delta\Gamma}{2\Gamma}\right)^2\right] \tag{1.4}$$

where Γ is the average width. Mixing is generally parameterized in terms of the two dimensionless quantities [12]

$$x = \frac{\Delta m}{\Gamma} \quad \text{and} \quad y = \frac{\Delta\Gamma}{2\Gamma} \tag{1.5}$$

such that $R_{\text{mix}} = \frac{1}{2}(x^2 + y^2)$.

It should be noted that the weak eigenstates are CP eigenstates only in the limit of CP conservation in the charm sector. This limit is assumed to be valid throughout this analysis. While charm sector CP violation is expected at some low level in the SM, all searches have produced negative results [13] and the existence of CP violation orders of magnitude below our sensitivity would not affect these results.

1.2.1 Short Range Mixing

The standard method to calculate the mixing rate is with the box diagrams shown in Figure 1.4. Mixing mediated by quark loops is known as short range mixing.

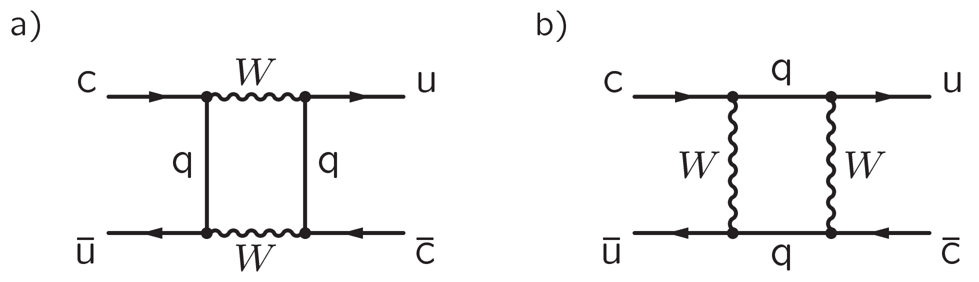

Figure 1.4: The box diagrams that give the lowest order contribution to $D^0-\overline{D}^0$ mixing.

Calculations based on box diagrams predict a $D^0-\overline{D}^0$ mixing rate R_{mix} of about 10^{-12} [14].

The relative strength of the box diagram amplitude for different neutral meson systems is driven by two factors. The first factor is the product of the CKM matrix elements from each of the four weak vertices $V_{Qq}^2 V_{Qq'}^2$, where Q is the quark in the loop and q and q' are the quarks in the neutral meson. The second factor is the mass squared ratio m_Q^2/M_W^2 [15, 16], where m_Q is the mass of the loop quark and M_W is the mass of the W boson. Only the most massive loop quarks will make a large contribution to the amplitude, but the CKM factor tends to suppress contributions from heavy loop quarks when the external quarks are light. Table 1.2 compares the amplitude factors for the different neutral systems. As is apparent in the table, the $D^0-\overline{D}^0$ system is expected to have the smallest mixing rate from short range effects.

Table 1.2: Comparison of the box diagram amplitude factors for different neutral mesons systems. The factor λ is from the Wolfenstein parameterization Equation (1.3).

	External Quarks (qq')	Loop Quark (Q)	m_Q^2/M_W^2	$V_{Qq}^2 V_{Qq'}^2$
K^0	sd	c	10^{-4}	$\lambda^2 \sim 0.05$
	sd	t	5	$\lambda^{10} \sim 10^{-7}$
D^0	cu	s	10^{-6} [a]	$\lambda^2 \sim 0.05$
	cu	b	10^{-3}	$\lambda^{10} \sim 10^{-7}$
B_d^0	bd	t	5	$\lambda^6 \sim 10^{-4}$
B_s^0	bs	t	5	$\lambda^4 \sim 10^{-3}$

[a] In computing this factor the momenta of the external legs can not be ignored. The correct suppression factor is $m_s^4/m_c^2 M_W^2$ [14].

1.2.2 Long Range Mixing

Another possible contribution to the mixing rate comes from interactions mediated by mesons instead of quarks. This is known as long range mixing because the hadronization of the intermediate states requires a larger scale. In the $D^0-\overline{D}^0$ system, the long range contribution may be significantly larger than the short range. This situation is markedly different from the $K^0-\overline{K}^0$ and $B^0-\overline{B}^0$ systems where in the former the short range and long range contributions are thought to be of comparable size, and in the latter the short range contribution dominates.

Exact calculations of long range mixing are not possible because of the non-perturbative nature of QCD at the light quark mass scale. Instead the long range contributions are approximated by the following methods.

Dispersive Approach

By considering hadronic decays modes that couple to both the D^0 and $\overline{D}^0$ (*e.g.* $K^-\pi^+$, K^+K^-, $\pi^+\pi^-$ and $K^+\pi^-$), one can crudely estimate an upper limit of the mixing rate, $R_{\text{mix}} \leq 2\tan^4\theta_{\text{C}} \simeq 0.5\%$ [17], which is just the expected Cabibbo suppression factor for a $\Delta\text{C} = 2$ process. A more careful analysis of the intermediate meson states indicates that there should be large GIM mechanism cancellations between the different modes. In the limit of flavor SU(3) symmetry, the GIM cancellation is complete. Dispersive analyses with appropriate SU(3) breaking predict $R_{\text{mix}} \simeq 10^{-7}$ [18].

Heavy Quark Effective Theory

Heavy quark effective theory (HQET) can also be used to estimate the strength of long range mixing. These studies indicate that the enhancement to D^0–$\overline{D}^0$ mixing from long range effects might be even smaller than predicted by the dispersive analyses [19]. Calculations of the four, six and eight quark operators with the leading order QCD corrections predict R_{mix} of order 10^{-10} [20].

The use of HQET to analyze D meson properties assumes that the mass of the charm quark is much larger than Λ_{QCD}. This rather dubious assumption may invalidate the HQET calculation, and is representative of the general difficulty involved in predicting the long range contribution to the $D^0-\overline{D}^0$ mixing.

1.2.3 Non-Standard Model Mixing

The most interesting aspect of $D^0-\overline{D}^0$ mixing is the possibility that the expected effect in the SM is very small. If true, any observation of $D^0-\overline{D}^0$ mixing at the current experimental sensitivity would require new physics, beyond the SM. While the current theoretical picture is not clear enough to rule out R_{mix} of order 10^{-3} in the SM, an observation of mixing at this level is generally unexpected and would stimulate further research.

There are numerous possible new physics contributions to the $D^0-\overline{D}^0$ mixing rate, and a detailed discussion of them is beyond the scope of this thesis. Instead, Figure 1.5 presents a compilation of 56 different published $D^0-\overline{D}^0$ mixing predictions, of which 31 are non-SM. The spread in these predictions covers 7 orders of magnitude in mixing amplitude.

1.3 Notation

The existence of two paths for the decays $D^0 \to K^-\pi^+$ makes referring to this process cumbersome. Therefore we will adopt the notation right sign (RS) to refer to the CF decay and wrong sign (WS) to refer to decays consistent with the DCS and mixed processes.

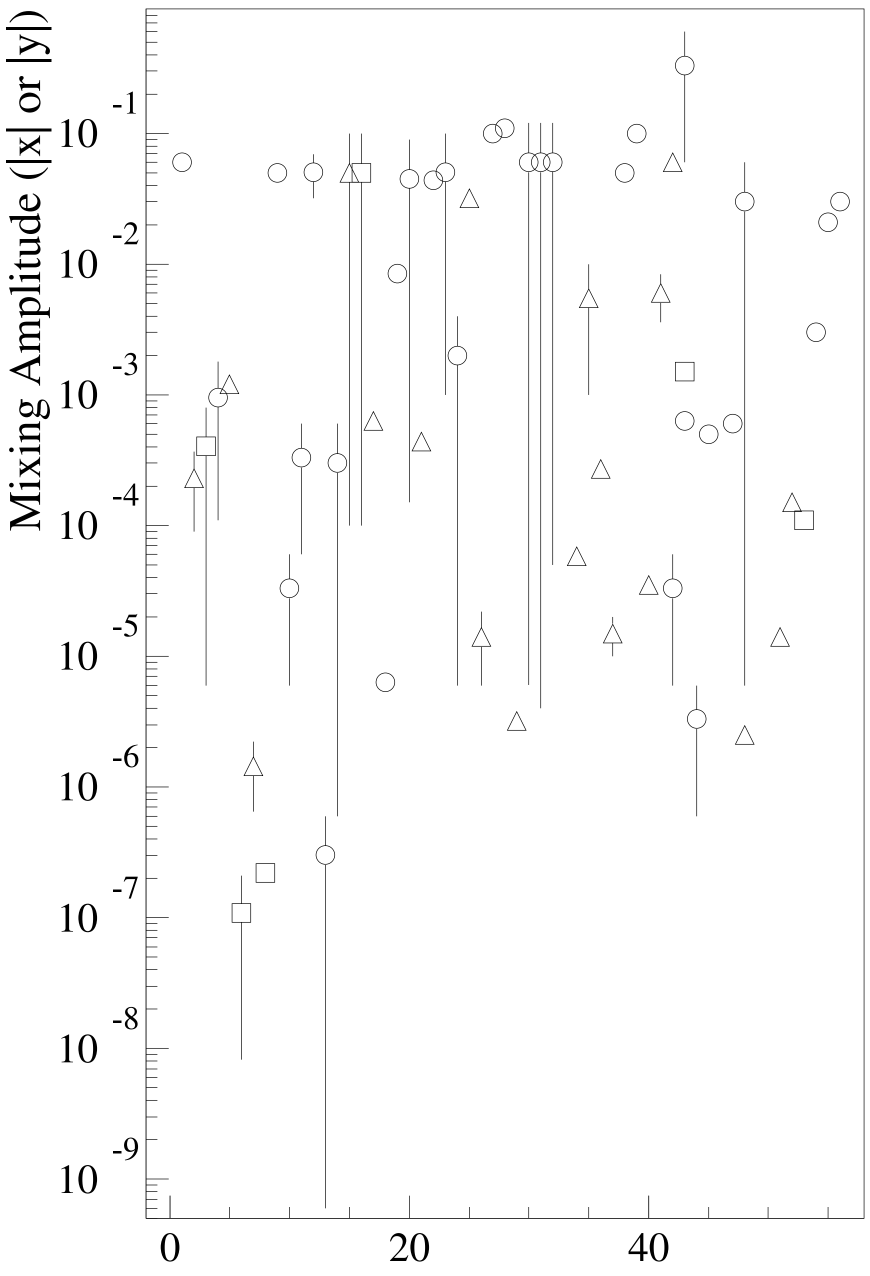

Figure 1.5: A collection of 56 theoretical predictions for $D^0 - \overline{D}^0$ mixing based on the compilation of Harry Nelson [21]. The triangles are SM based predictions of x, the squares are SM predictions of y and the circles are non-SM predictions of x.

1.4 Interference Between DCS and Mixing

In quantum mechanics when there are two or more paths from an initial state to a final state, there is the possibility for interference between the paths. As will be shown in the following derivation, the interference between DCS and mixing in D^0 decays provides a potentially observable effect which is significantly enhanced compared to $R_{\rm mix}$.

Assuming CP conservation in the charm meson system[3], the CP eigenstates of the neutral D system can be written as

$$|D_1\rangle = \frac{1}{\sqrt{2}}\left(|D^0\rangle + |\overline{D}^0\rangle\right) \tag{1.5a}$$

$$|D_2\rangle = \frac{1}{\sqrt{2}}\left(|D^0\rangle - |\overline{D}^0\rangle\right). \tag{1.5b}$$

If we define

$$CP|D^0\rangle = |\overline{D}^0\rangle$$

it then follows that $|D_1\rangle$ is a CP even state and $|D_2\rangle$ is CP odd. The time evolution of the $|D_1\rangle$ and $|D_2\rangle$ states is [23]

$$|D_i(t)\rangle = e^{-i(M_i - i\frac{\Gamma_i}{2})t}|D_i(0)\rangle, \tag{1.7}$$

where M_i and Γ_i are the mass and width for state i. Rearranging Equations (1.5a) and (1.5b) we find in terms of D_1 and D_2, that a pure D^0 state produced at time

[3]For a derivation of the interference relation without the assumption of CP conservation see Ref [22]

$t = 0$ is

$$|D^0\rangle = \frac{1}{\sqrt{2}}\left(|D_1\rangle + |D_2\rangle\right). \tag{1.8}$$

We obtain the time evolution of D^0 by plugging in the time evolution of the D_1 and D_2 states as given by Equation (1.7):

$$|D^0(t)\rangle = \frac{1}{\sqrt{2}}\left(e^{-i(M_1 - i\frac{\Gamma_1}{2})t}|D_1(0)\rangle + e^{-i(M_2 - i\frac{\Gamma_2}{2})t}|D_2(0)\rangle\right). \tag{1.9}$$

This can be expressed in terms of the $|D^0\rangle$ and $|\overline{D}^0\rangle$ by using the relations in Equations (1.5a) and (1.5b) and combining like terms:

$$|D^0(t)\rangle = \frac{1}{2}\left(A_+|D^0\rangle + A_-|\overline{D}^0\rangle\right), \tag{1.10}$$

with

$$A_\pm = e^{-i(M_1 - i\frac{\Gamma_1}{2})t} \pm e^{-i(M_2 - i\frac{\Gamma_2}{2})t}. \tag{1.11}$$

The terms $A_\pm$ can be arranged in more convenient forms by using the definitions:

$$\Delta M = M_1 - M_2, \tag{1.12}$$

$$\Delta\Gamma = \Gamma_1 - \Gamma_2, \tag{1.13}$$

$$M = \tfrac{M_1 + M_2}{2}, \tag{1.14}$$

$$\Gamma = \tfrac{\Gamma_1 + \Gamma_2}{2}, \tag{1.15}$$

and factoring $e^{-(iM+\Gamma/2)t}$ from each term, yielding

$$A_\pm = e^{-(iM+\frac{\Gamma}{2})t}\left(e^{-(i\Delta M + \frac{\Delta\Gamma}{2})t/2} \pm e^{(i\Delta M + \frac{\Delta\Gamma}{2})t/2}\right). \tag{1.16}$$

Using trigonometric identities and the definitions given in Equation (1.5) we obtain

$$A_+ = 2e^{-(iM+\frac{\Gamma}{2})t}\cosh\left[(y+ix)\frac{\Gamma t}{2}\right] \tag{1.16a}$$

and

$$A_- = -2e^{-(iM+\frac{\Gamma}{2})t}\sinh\left[(y+ix)\frac{\Gamma t}{2}\right]. \tag{1.16b}$$

Then

$$|D^0(t)\rangle = \\ e^{-(iM+\frac{\Gamma}{2})t}\left\{\cosh\left[(y+ix)\frac{\Gamma t}{2}\right]|D^0\rangle - \sinh\left[(y+ix)\frac{\Gamma t}{2}\right]|\overline{D}^0\rangle\right\}. \tag{1.18}$$

Now we are prepared to answer the question: What is the probability of an originally pure D^0 state to decay to $K^+\pi^-$? Define $\langle f|$ to be the vector representing the final state $K^+\pi^-$. The amplitude for this decay process is

$$\langle f|D^0(t)\rangle = \\ e^{-(iM+\frac{\Gamma}{2})t}\left\{\cosh\left[(y+ix)\frac{\Gamma t}{2}\right]\langle f|D^0\rangle - \sinh\left[(y+ix)\frac{\Gamma t}{2}\right]\langle f|\overline{D}^0\rangle\right\} \tag{1.19}$$

where $\langle f|D^0\rangle$ is the DCS decay amplitude and $\langle f|\overline{D}^0\rangle$ is the CF amplitude. The CF amplitude is factored out of Equation (1.19) and the DCS to CF amplitude ratio is written as

$$\frac{\langle f|D^0\rangle}{\langle f|\overline{D}^0\rangle} = -\sqrt{R_{\text{DCS}}}e^{-i\delta}, \tag{1.20}$$

where R_{DCS} is the the DCS to CF branching ratio and δ is a strong force phase between the DCS and CF amplitudes. Then

$$\begin{aligned} \langle f|D^0(t)\rangle = & \\ & -e^{-(iM+\frac{\Gamma}{2})t}\langle f|\overline{D}^0\rangle \times \\ & \left\{\cosh\left[(y+ix)\frac{\Gamma t}{2}\right]\sqrt{R_{\text{DCS}}}e^{-i\delta}+\sinh\left[(y+ix)\frac{\Gamma t}{2}\right]\right\}. \end{aligned} \tag{1.21}$$

Approximating the hyperbolic functions with the first term of their Taylor series expansions ($\sinh x = x$ and $\cosh x = 1$) we get

$$\langle f|D^0(t)\rangle = e^{-(iM+\frac{\Gamma}{2})t}\langle f|\overline{D}^0\rangle\left[-\sqrt{R_{\text{DCS}}}e^{-i\delta}-(y+ix)\frac{\Gamma t}{2}\right]. \tag{1.22}$$

Finally, the probability is the absolute value square of the amplitude:

$$\begin{aligned} |\langle f|D^0(t)\rangle|^2 = & \\ & e^{-\Gamma t}|\langle f|\overline{D}^0\rangle|^2\left|-\sqrt{R_{\text{DCS}}}(\cos\delta - i\sin\delta) - (y+ix)\frac{\Gamma t}{2}\right|^2 = \\ & e^{-\Gamma t}|\langle f|\overline{D}^0\rangle|^2\left[R_{\text{DCS}}+\sqrt{R_{\text{DCS}}}(y\cos\delta - x\sin\delta)\Gamma t+\left(\frac{x^2+y^2}{4}\right)\Gamma^2 t^2\right]. \end{aligned} \tag{1.23}$$

Define a quantity $R(t)$, which is the time dependent rate for the WS process relative to the CF branching fraction or

$$R(t) = \frac{|\langle f|D^0(t)\rangle|^2}{|\langle f|\overline{D}^0\rangle|^2}, \tag{1.24}$$

and define the parameters x' and y' which are related to the mixing parameters, x and y, by a strong phase rotation:

$$x' = x\cos\delta + y\sin\delta, \tag{1.24a}$$

$$y' = y\cos\delta - x\sin\delta. \tag{1.24b}$$

Redefine t in units of the D^0 lifetime (where $\Gamma t = t/\tau_{D^0}$) to obtain an expression for the lifetime evolution of the decay $D^0 \to K^+\pi^-$:

$$R(t) = \left[R_{\rm DCS} + \sqrt{R_{\rm DCS}}y't + \left(\frac{x'^2+y'^2}{4}\right)t^2\right]e^{-t}. \tag{1.26}$$

The constant times e^{-t} term is a pure DCS, the t^2e^{-t} term is a pure mixing and the te^{-t} term is the interference of DCS and mixing.

The of behavior the full lifetime evolution, $R(t)$, as well as the contributions from each individual term are plotted in Figure 1.6. Figure 1.6a shows the case of constructive interference ($y' > 0$). Note the enhancement of WS decays over pure exponential at long lifetimes. Alternatively, when the interference is destructive

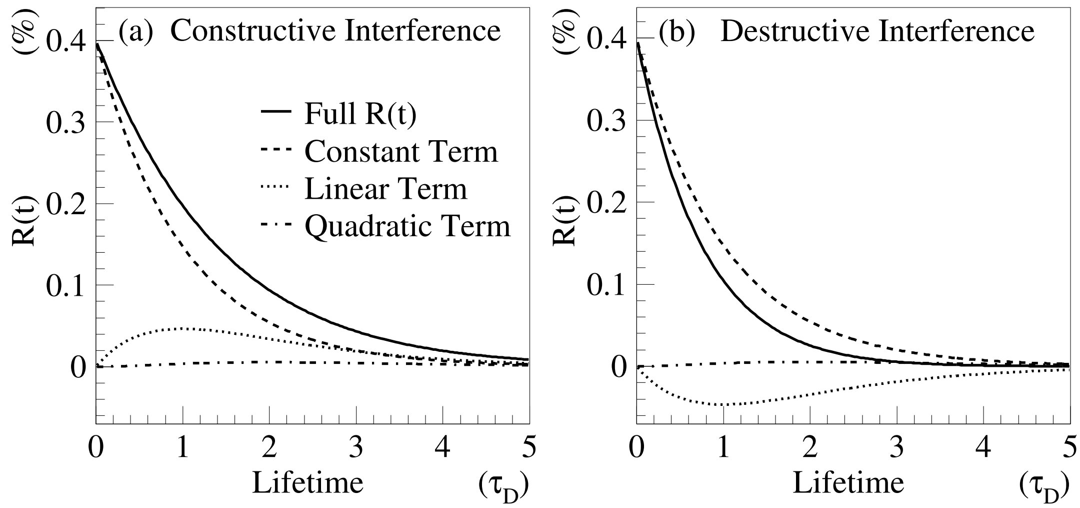

Figure 1.6: Time evolution of the decay $D^0 \to K^+\pi^-$ with **a)** constructive interference and **b)** destructive interference. A value of $y' = 2\%$ is used in this illustration.

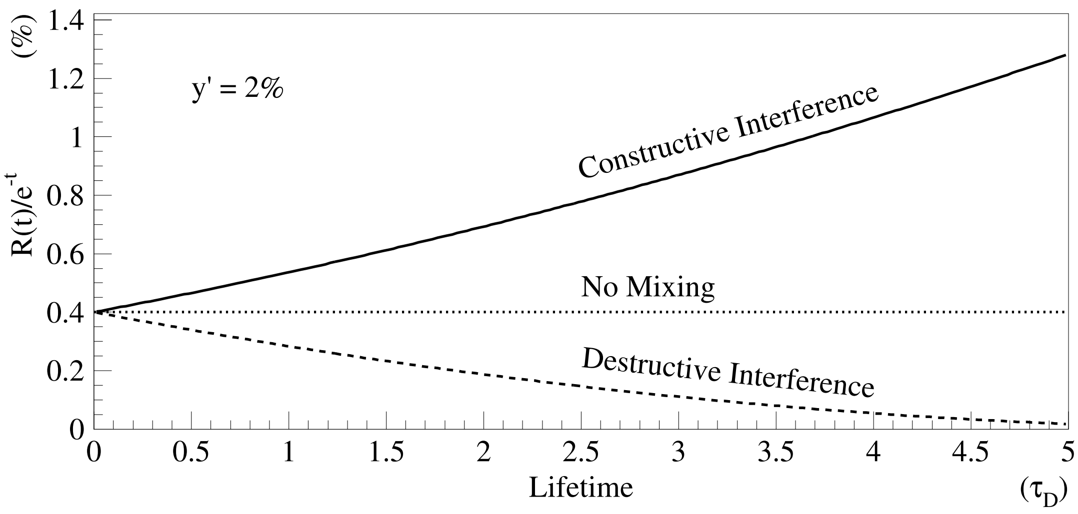

Figure 1.7: The lifetime dependence of $D^0 \to K^+\pi^-$ rate with $y' = 2\%$ for the cases of constructive interference, destructive interference and no mixing.

(Figure 1.6b) we expect fewer events at long lifetime. This deviation from pure exponential decay leads to an interesting consequence for the WS to RS branching ratio. Figure 1.7 shows the dependence of the branching ratio on the D^0 decay proper time. In the case of constructive (destructive) interference the branching ratio begins, at proper time equal to zero, at the DCS branching ratio and rises (falls) at longer lifetime. Therefore, if mixing is significant the measured value of this ratio will depend on the lifetime acceptance of the analysis.

1.4.1 Expectations for the Strong Phase δ

In the limit of unbroken SU(3) flavor symmetry, the strong phase δ between the decays $D^0 \to K^+\pi^-$ and $\overline{D}^0 \to K^+\pi^-$, is zero [24], but SU(3) flavor symmetry is known to be broken. For example, SU(3) symmetry predicts that the K and π should have the same mass, but the mass of the K is more than 3.5 times greater than the mass of the π. Nevertheless, as an approximate symmetry, flavor SU(3) has been a useful tool and as such predicts that δ should be small. An analysis considering the contributions of resonances near the D^0 finds that δ may be as large as 20° [25]. Fits to the experimentally measured branching fractions of D's with particular phenomenological models return values δ typically less than about 15° [26, 27, 28, 29].

1.5 $D^0-\overline{D}^0$ Mixing Searches

Limits on D^0–$\overline{D}^0$ mixing go back to just after the discovery of D meson [30]. Since that time the limits have steadily improved. There are several ways to search for $D^0-\overline{D}^0$ mixing (for an expanded discussion see Ref. [31]). I will focus on three methods that have been used to set the most restrictive limits.

Semileptonic Decays

Unlike the fully hadronic $D^0 \to K^+\pi^-$ process, the decay $D^0 \to K^+\ell^-\nu_\ell$ ($\ell = \mu$ or e) can only occur through mixing and there is no DCS channel to cause interference. Therefore, the time evolution for the semileptonic wrong sign process goes as the

t^2 term of Equation (1.26):

$$R(t) = \left(\frac{x'^2 + y'^2}{4}\right) t^2 e^{-t}. \tag{1.27}$$

By looking for a $K^+\ell^-\nu_\ell$ signal with cleanly identified D^0 events, a limit (or a measurement if a signal is observed) can be made on $R_{\rm mix}$. The current best limit with this method comes from E791 [32], which found $R_{\rm mix} < 0.50\%$ at the 90% confidence level.

Interference in Hadronic Decays

Several groups [5, 6, 7] have searched for D^0–$\overline{D}^0$ mixing with DCS decay modes such as $D^0 \to K^+\pi^-$ and $D^0 \to K^+\pi^-\pi^+\pi^-$, by looking for the interference term derived in Section 1.4. To disentangle the mixing and DCS, the lifetime distribution is fit to Equation (1.26). In contrast to the semileptonic method, this method has the potential to separate the x' and y' components of mixing. The best limits from this technique come from CLEO [7] which found $|x'| < 2.8\%$ and $-5.2\% < y' < 0.2\%$.

Direct Search for $\Delta\Gamma$

The third mixing search technique is to look for a difference in lifetime (or rate, Γ) for CP even and CP odd eigenstates[4]. The most suitable CP eigenstate is K^+K^-, which is CP even. It is compared to $K^-\pi^+$ which is assumed to be an

[4]The mass difference (Δm) is far too small to be observed directly with the current experimental sensitivity.

even mixture of CP even and CP odd. The most sensitive measurement with this method comes from FOCUS which finds $y = (3.42 \pm 1.39 \pm 0.74)\%$ [33].

A comparison of these three search limits in x' and y' space is shown in Figure 1.8. It is important to remember that the FOCUS $\Delta\Gamma$ limit is only directly comparable to the other two measurements in the limit that the strong phase δ goes to zero. For the FOCUS and CLEO results to be in agreement at the $1\,\sigma$ level requires $\delta \geq \pi/4$ [34].

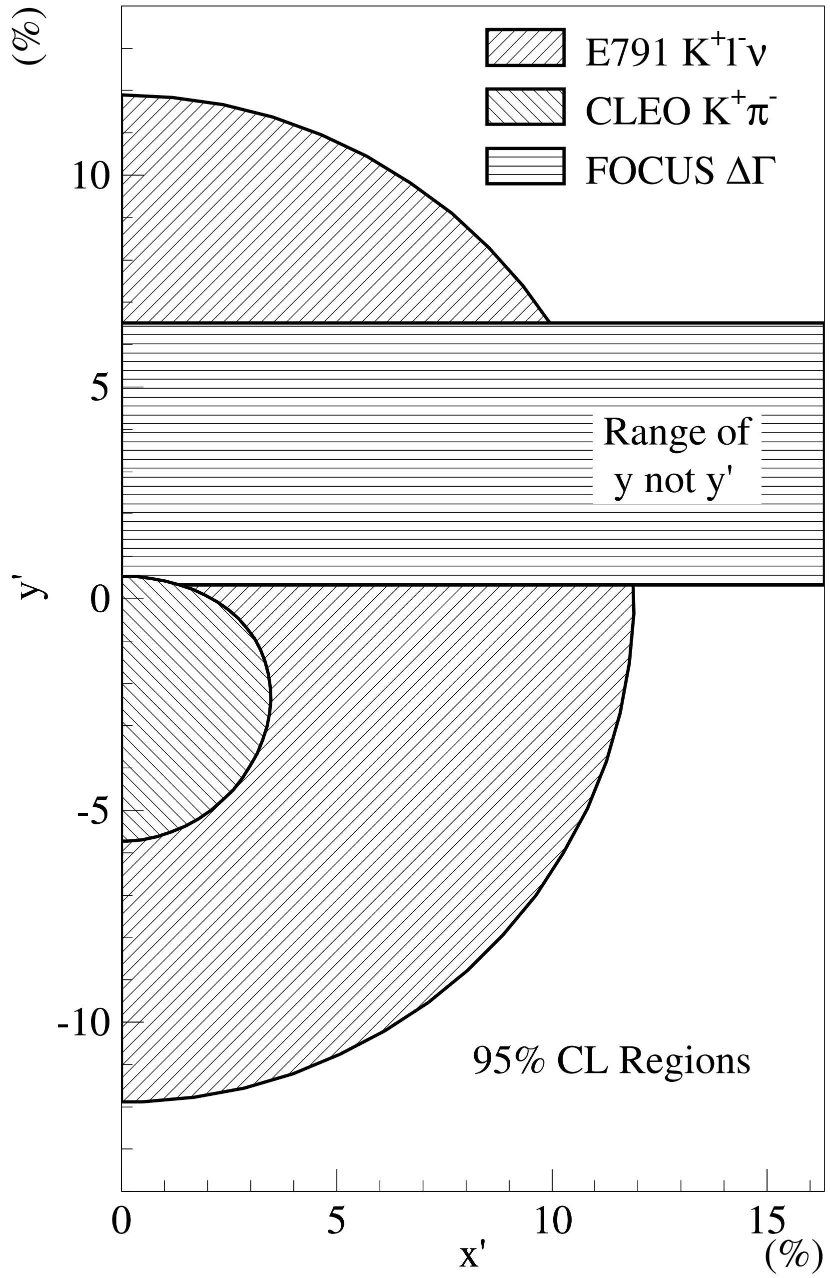

Figure 1.8: Comparison of the best experimental limits on x' and y' from the three methods discussed in Section 1.5. The FOCUS $\Delta\Gamma$ band is only directly comparable to the other experiments in the case of $\delta = 0$.

Chapter 2

The FOCUS Beam Line

Our study of charm particles in a relatively clean and forward environment relies on the production of a high energy photon beam. This photon beam is created through a multistep process that requires tools unique to the Fermilab accelerator complex. We begin with a description of how the 800 GeV proton beam is generated. Then we will discuss how that proton beam is used to produce the wide band photon beam used in the production of charm particles.

2.1 The Proton Beam

The first stage of acceleration is provided by a device known as the Cockroft-Walton. Inside this device electrons are added to hydrogen atoms so that the resulting negative ions can be accelerated across a single electrostatic gap to an

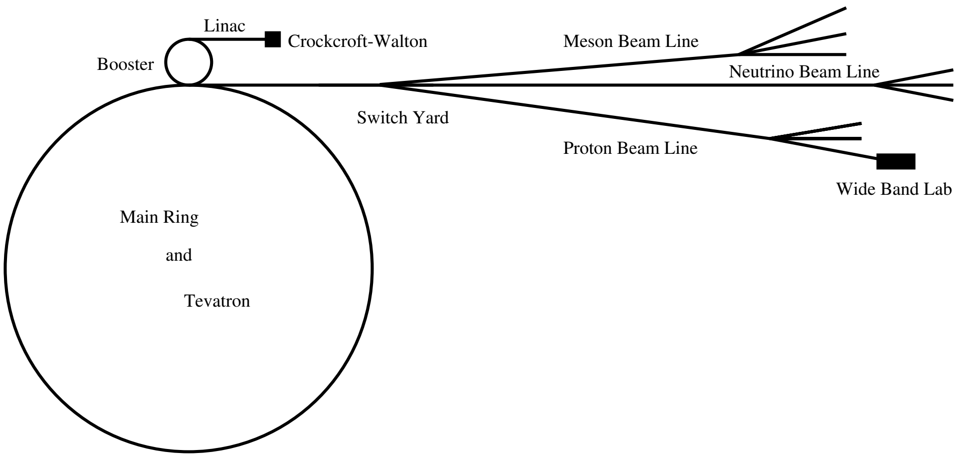

Figure 2.1: Schematic of the Fermilab accelerator complex and fixed target beam lines.

energy of 750 KeV.

After leaving the Cockroft-Walton, the hydrogen ions enter the Linac (from **Lin**ear **ac**celerator). Inside the Linac the hydrogen ions pass through a series of drift tubes. An oscillating electric field is applied to the tubes such that the ions always feel an accelerating force. The Linac accelerates the ions from 750 KeV to 400 MeV. Before continuing on to the next stage, the hydrogen ions are passed through a carbon foil which strips away the electrons, leaving only the protons.

The next stage of acceleration occurs in a 500 foot diameter synchrotron known as the Booster. The Booster uses magnets to bend proton beams around in a circular path. Along that path they repeatedly pass through an accelerating electric field. Each proton travels around the Booster approximately 20,000 times and emerges with an energy of 8 GeV.

After acceleration by the Booster is complete, the protons are transferred to the Main Ring. The Main Ring is a much larger (4 miles around) synchrotron. It raises the proton energy from 8 GeV to 150 GeV.

The 150 GeV Main Ring proton beam is then injected into the Tevatron. The Tevatron uses the same 4 mile circular tunnel as the Main Ring. Like the Main Ring it is also a synchrotron, but what distinguishes it from the Main Ring are the 1000 high field superconducting magnets that steer the beam. This allows the Tevatron to reach an energy, which is double the maximum Main Ring energy, in a ring of the same dimensions. The superconducting magnets are cooled with liquid helium to a temperature of 4.5 Kelvin.

The Tevatron accelerates the protons to an energy of 800 GeV. The radio frequency cavities used to accelerate the beam in the Tevatron group the protons into bunches known as beam buckets. During fixed target operation the Tevatron holds just over 1000 proton buckets separated in time by about 20 ns.

During the 1996-97 fixed target run the Fermilab accelerator complex operated on a 60 second cycle. In the first 40 s, the Tevatron is filled with beam which it accelerates to an enrgy of 800 GeV. In the remaining 20 s the beam is slowly extracted from the Tevatron and delivered to the experiments. In the Main Switch Yard the proton beam is split and beams are sent to each of three main beam line areas known as Meson, Neutrino, and Proton. The beam is further split in each of these beam lines and sent to various experimental areas. The Wideband

Photon Lab is located at the end of the eastern most beam line in the Proton Area. Figure 2.1 provides a schematic overview of the accelerator complex and beam lines as they appeared in the 1996-97 fixed target run.

2.2 The Photon Beam

About 365 meters upstream of the FOCUS experimental target is a 3.6 m long liquid deuterium target. The 800 GeV proton beam collides with this target generating a shower of charged and neutral particles. The charged particles are swept out of the beam by a system of dipole magnets and collimators. The remaining neutral particles (including photons, neutrons and K_L's) pass through a 60% radiation length lead converter in which most of the photons interact to produce e^+e^- pairs. These electrons and positrons are magnetically transported around a dump that absorbs the remaining neutral beam particles. The FOCUS beam line doubles the intensity of the E687 beam [35] by utilizing both the electrons and the positrons with a unique design that routes the oppositely charged e^+e^- tracks around opposite sides of the neutral dump [36]. The magnetic transport accepts a momentum range of $\pm 15\%$ about the central momentum value. Typically the magnets are optimized for electron and positron beams of 300 GeV.

On the other side of the neutral dump the two oppositely charged beams are recombined into a single beam which is focused on the experimental target. About

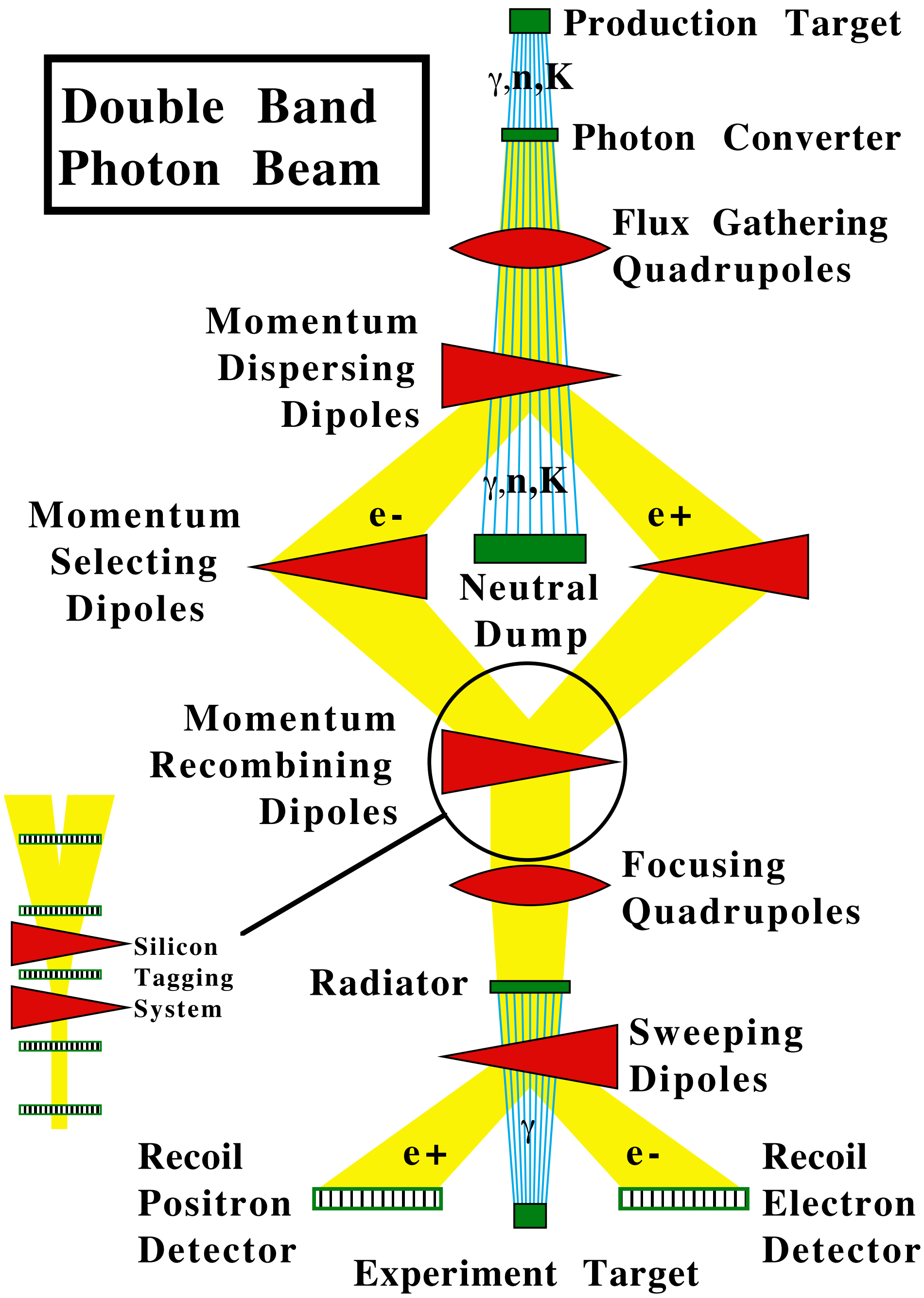

Figure 2.2: Schematic of Wideband photon beam line.

40 m upstream of the target is a 20% radiation length lead radiator. Electrons and positions passing through this radiator may bremsstrahlung producing photons. These bremsstrahlung photons follow the direction of the original charged particle towards the experimental target. Downstream of the radiator the $e^{\pm}$ particles are swept into an instrumented beam dump by dipole magnets while the photons pass through a narrow collimator and on to the experimental target.

2.3 Photon Energy Measurement

As the electron and positron beams are refocused on to the target, the individual beam particle momenta are measured by a series of five silicon strip planes. The recoil energy of the $e^{\pm}$ after passing through the lead radiator is measured by a pair of lead glass calorimeters (one for the electron side and one for the positron side) located at the front of the charged particle dump. The energy of the recoiling beam track is determined by measuring the deflection of the track as it passes through the sweeper magnets. The total photon energy is equal to the difference between the $e^{\pm}$ energy measured before and after the radiator. It is possible for more than one bremsstrahlung interaction to occur, so to determine the energy of the interacting photon we must subtract the energy of any non-interacting photons. This is achieved by subtracting the energy collected in the Beam Gamma Monitor (BGM). The BGM is a small calorimeter just downstream of the Inner

Electromagnetic calorimeter (See Figure 3.1). It covers the center of the spectrometer and collects the energy of any non-interacting photons as well as e^+e^- pairs generated in photon electromagnetic interactions.

Chapter 3

The FOCUS Spectrometer

The FOCUS detector is a double bend, magnetic spectrometer. The photon beam interacts with a beryllium oxide target producing short lived states which decay into both charged and neutral longer lived particles. Charged particles are tracked with silicon strip detectors before passing through the first dipole analysis magnet. Three stations of wire chambers are used to track the charged particles between the first and second magnets. Downstream of the second magnet there are two wire tracking stations. The change in vertical track slope as measured in the three tracking regions, combined with knowledge of the magnetic field strength leads to a determination of a charged track's momentum. Once a track's momentum is known, the presence or absence of hits in each of the three threshold Čerenkov counters allows the determination of the particle identification hypotheses. Neutral particles such as photons and neutrons are detected, and their energies are

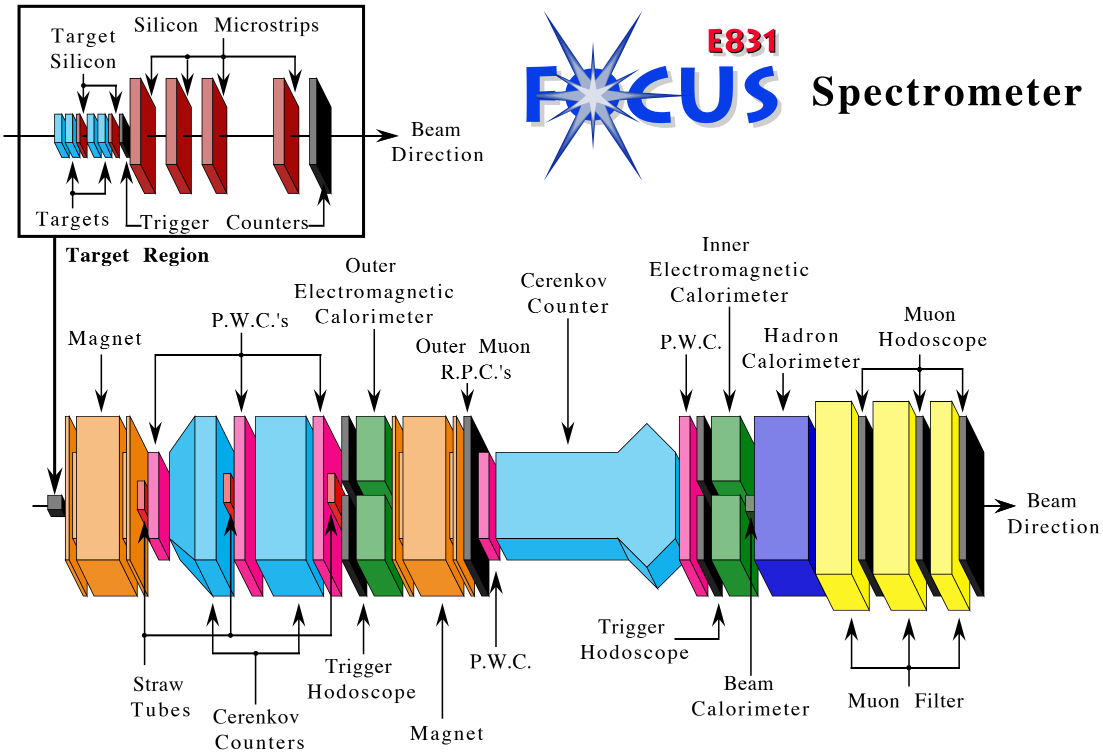

Figure 3.1: Schematic of the FOCUS Spectrometer.

measured, by one of three calorimeters. The calorimeters also aid in particle identification and play a crucial roll in event triggering. Finally, the muon system detects charged particles as they pass through massive iron walls, providing a mechanism for the separation of muons from pions and kaons. A schematic layout of the spectrometer is given in Figure 3.1)

3.1 Target

The choice of target material and configuration is the result of a simultaneous optimization of three competing physics criteria.

1. Maximize the rate of hadronic interactions to electromagnetic interactions:

$$\frac{\sigma_{had}}{\sigma_{em}} \propto \frac{Z^2}{A^{\frac{2}{3}}} \tag{3.1}$$

   where A is the atomic mass and Z is the atomic number.

2. Maximize the fraction of charm decays outside of the target material.

3. Maximize acceptance, with a compact target assembly.

Of the isotopes that satisfy the first condition (${}^{2}_{1}$H, ${}^{3}_{1}$H, ${}^{7}_{3}$Li and ${}^{9}_{4}$Be) only ${}^{9}_{4}$Be is suitable as a safe, low cost target material. In order to satisfy the second condition, the target is segmented into 4 pieces, which allows approximately 60% of all D^+ to decay in the air gaps. Finally, to satisfy the third condition, Be was replaced by BeO as the target material because of its greater density (see Table 3.1).

Table 3.1: Comparison of the properties of possible target materials.

Material	Int. Len. (gm/cm^2)	Rad. Len. (gm/cm^2)	Density (gm/cm^2)
Be	75.2	65.2	1.848
BeO	84.6	13.7	2.90

3.2 Silicon Strip Detectors

Silicon strip detectors (SSD) are long, thin diodes etched onto silicon wafers. These diodes are held at reverse bias creating an electric field across the diode volume. When a charged track passes through the silicon it separates electrons from atoms creating free electron-hole pairs which then migrate across the diode under the influence of the bias voltage. Collectively these electron-hole pairs create a signal pulse that is amplified and digitized by the SSD electronics.

The tracking of charged particles between the target segments and the first analysis magnet is done by 16 planes of SSD's. The FOCUS SSD system is actually two distinct systems: the target silicon (labeled TSSD in Figure 3.2) and the original E687 system (labeled SSD).

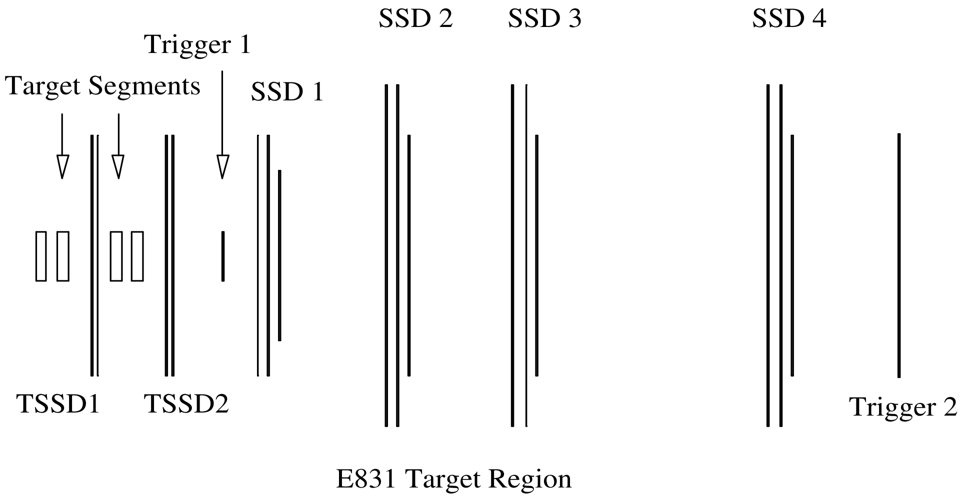

Figure 3.2: Layout of the FOCUS target region, showing the four target segments, the four target silicon planes (TSSD), the 12 E687 SSD planes and the trigger elements TR1 and TR2 (described in Section 3.11.1).

3.2.1 The Target Silicon

The target silicon system consists of two stations. The first station is located between the second and third target block and the second station is located between the fourth target segment and the E687 SSD's. Each target silicon station consists of two planes with strips oriented at $\pm 45^\circ$ from the vertical. Each plane has 1024 strips spaced at 25 μm and each strip is about 50 mm long, which makes the active region 25 $mm \times 50$ mm.

3.2.2 The E687 SSD's

The original E687 SSD system consists of 4 stations of detectors located downstream of the target silicon and upstream of the first analysis magnet. The first three stations are separated by a distance of 6 cm, and the fourth and most downstream station is separated from the third station by 12 cm. (See Figure 3.2 for the locations of components in the target region.)

Each station has three views. One plane, of each station, has strips oriented vertically and the other two planes are $\pm 45^\circ$ from vertical. Each plane consists of 688 strips separated into inner and outer regions. There are 384 strips in the inner region and 152 strips on each side of the outer region. The planes of the first station have strips spaced at 25 μm in the inner region and 50 μm in the outer region. All strips in the first station are 25 mm long. The remaining three stations have an inner spacing of 50 μm and an outer spacing of 100 μm, with a strip length of 50 mm.

3.3 Analysis Magnets

As the word spectrometer implies, the momentum spectrum of charged particles in the experiment is spread vertically as they pass through the dipole magnets. Reconstruction of a charged track on either side of the magnet then provides an accurate measure of its momentum by a simple application of the Lorentz force law. Two large aperture dipole magnets are used. The first magnet (M1) is located between the SSD system and the first station of wire tracking. Its operating current is 1020 amps and it provides a momentum kick of 0.5 GeV/c. The second magnet (M2) is located downstream of the third station of wire tracking (see Figure 3.1). Operating at a current of 2000 amps with its polarity opposite that of M1, M2 provides a kick of 0.85 GeV/c. The net result of both magnets is an approximate refocusing of charged particles in the vicinity of the Hadronic Calorimeter.

3.4 Proportional Wire Chambers

The operation of proportional wire chambers (PWC) is very similar to that of SSD's. In a PWC the potential difference comes from the voltage on the anode wire planes which creates a potential difference between the anode planes and the signal wire planes which are held at ground. The drift of free charge toward the signal and anode wires results in the formation of a pulse on the signal wire that is picked up by preamplifiers.

The PWC system in FOCUS consists of 20 signal planes grouped into 5 stations with 4 planes per station. The stations are labeled P0, P1, P2, P3 and P4, from upstream to downstream. Stations P0, P1 and P2 are located between the two analysis magnets with P0 just downstream of M1. Chamber P3 is located just downstream of M2 and P4 is just downstream of the last Čerenkov counter, C3.

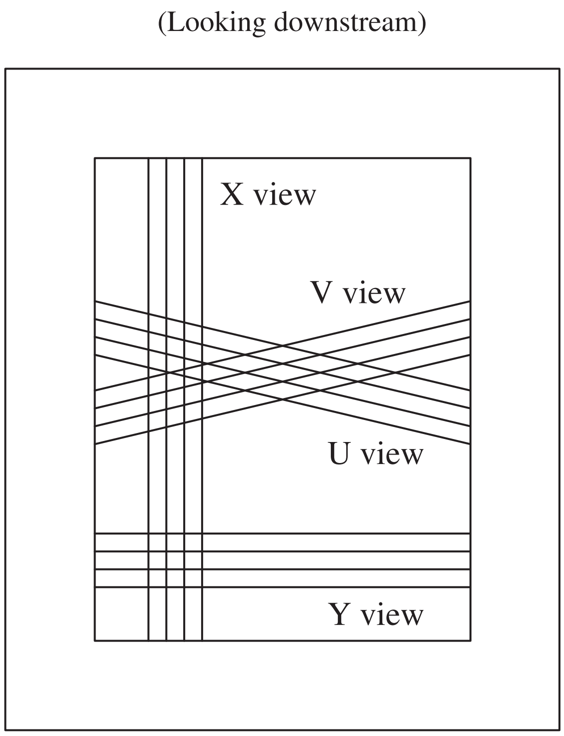

Figure 3.3: Signal wire layout of the proportional wire chambers.

All stations contain four views Y, V, U, and X, listed in order from upstream to downstream. Views X and Y measure track positions in x and y respectively. The U and V views are oriented $\pm 11.3°$ from the horizontal (Y) view and contribute position information along a coordinate perpendicular to their wires. (See figure 3.3)

There are two types of PWC stations, Type I (P0 and P3), and Type II (P1, P2 and P4). The Type I stations have an aperture of approximately 76 $cm \times 127$ cm (larger dimension is vertical) and a signal wire spacing of 2 mm. The Type II stations have an aperture of approximately 152 cm $\times$ 229 cm and a wire spacing of 3.3 mm.

The chambers are operated in a gas mixture of 65% argon and 35% ethane which was bubbled through ethyl alcohol.

3.5 Straw Tube Detectors

Three straw tube wire chambers are used to cover the high e^+e^- pair flux region (generated by photon conversions in the target which are subsequently spread into a vertical strip by the analysis magnets). Each chamber has three views, and within each view there are three nested straw layers.

All three chambers have a vertical (x measuring) view consisting of 30 straws (3 layers by 10 rows), and two angled views ($\pm 11.33^o$ from vertical). The

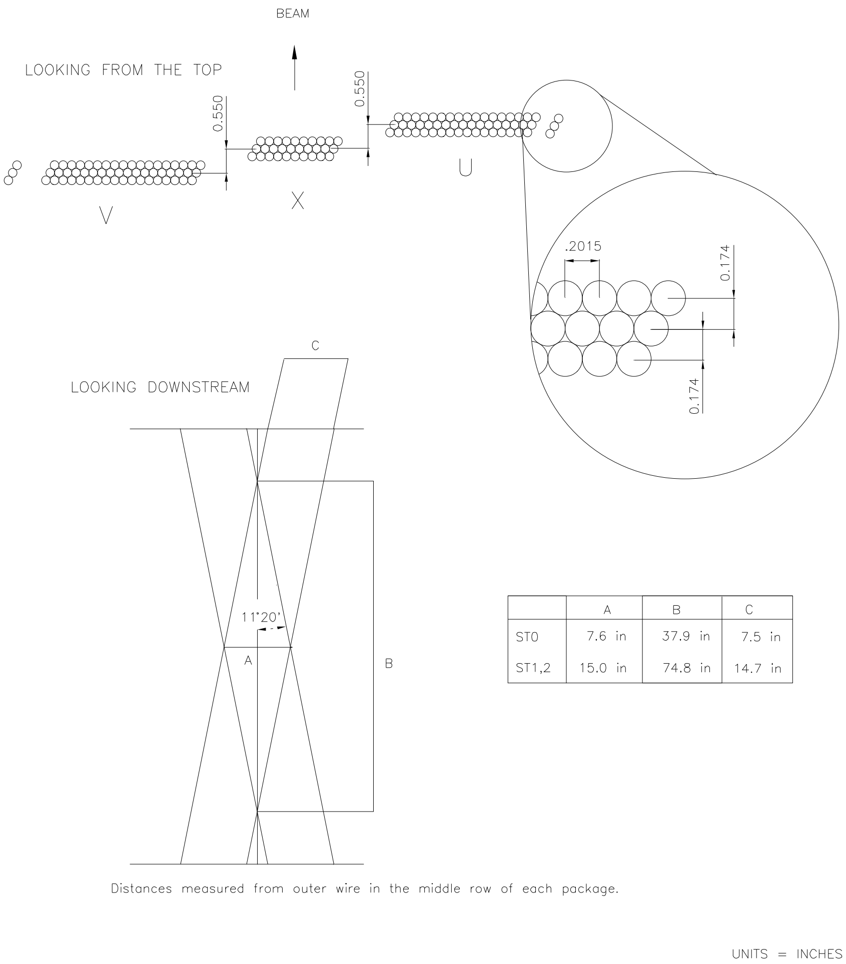

	A	B	C
ST0	7.6 in	37.9 in	7.5 in
ST1,2	15.0 in	74.8 in	14.7 in

Figure 3.4: Schematic of the straw tube detectors showing basic layout and dimensions.

most upstream chamber (ST0) is built with 138 cm long straws. Its angled views each consist of 114 straws (3 by 38). The other two chambers (ST1 and ST2) use 241 cm long straws and each angled view is comprised of 222 straws (3 by 74). (See figure 3.4.)

Each straw tube measures 5 mm in diameter. The straw material consists of two layers of $\sim$10 μm thick mylar with a thin vapor deposition coating of copper on the inner surface. The central anode wire is 20 μm thick gold plated tungsten.

The straws are operated with a slowly flowing gas mixture of 50% argon and 50% ethane, at a negligible positive pressure. The copper-coated straw wall is held at ground and the central wire is kept at a positive potential of about 1600 volts.

3.6 Čerenkov Counters

When a charged particle travels faster than the speed of light in a material it emits radiation known as Čerenkov light, at an angle θ defined by

$$\cos\theta = \frac{1}{n\beta} \tag{3.2}$$

where β is the velocity of the particle, and n is the index of refraction of the material. If $\frac{1}{n\beta} < 1$ then no Čerenkov light is emitted. Two charged particles with the same momentum, but different mass will have different velocities and thus different Čerenkov thresholds. The light collected in a circle of radius

$$r = l(n\beta - \frac{1}{n\beta}) \tag{3.3}$$

(where l is the length of the detector material) about the point where the track intercepts the back plane of the detector, is used to determine if the track is above threshold.

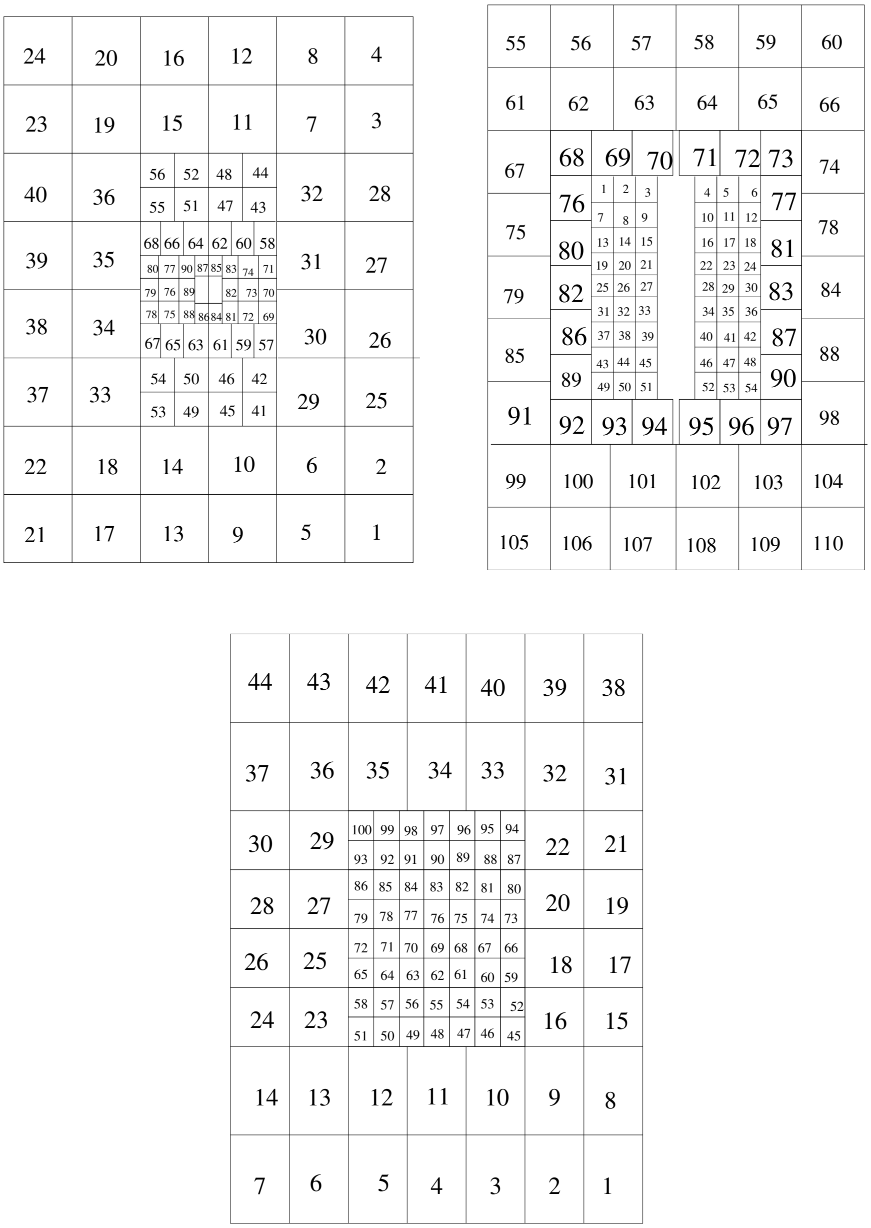

Figure 3.5: Mirror layout of the Čerenkov counters C1(top left), C2(top right) and C3(bottom).

Table 3.2: Čerenkov detector properties and thresholds.

Detector	Number of Cells	Length (cm)	Gas	Threshold (GeV/c)		
				π	K	p
C1	90	188	80% He, 20% N_2	8.4	29.8	56.5
C2	110	188	N_2O	4.5	16.0	30.9
C3	100	711	He	17.4	61.8	117.0

The gases used in a Čerenkov detector are chosen for their optical transparency and to optimize the system's ability to distinguish between the stable charged particles (e, μ, $\pi^{\pm}$, $K^{\pm}$ and p) at the typical momentum scale of the experiment. FOCUS uses three gas Čerenkov detectors referred to as C1, C2, and C3 in order from upstream to downstream. The detector properties and thresholds are shown in Table 3.6.

The back plane of each detector is divided into cells. The light arriving in each cell is reflected into photo tubes mounted on the side of the detector. The central cells are denser than the outer cells. Figure 3.5 shows the cell layouts for each of the three Čerenkov detectors.

3.7 Outer Electromagnetic Calorimeter

The Outer Electromagnetic Calorimeter (OE) [37] detects and measures the energy of electromagnetic particles ($e^{\pm}$ and γ) that are outside the acceptance of M2. It sits just in front of M2 and has a rectangular gap in the middle which matches the magnet's aperture. The OE's design is that of a lead-aluminum-scintilator sandwich, with 10 modules of various orientations.

3.8 Inner Electromagnetic Calorimeter

The Inner Electromagnetic calorimeter (IE) detects and measures the energy of electromagnetic particles that are within the acceptance of M2. The IE is an array of lead glass blocks arranged in a tower geometry. Čerenkov light generated in the lead glass by the charged particles of the electromagnetic shower is collected by phototubes mated to the lead glass blocks on the downstream end of the calorimeter. The detector is divided into two halves about the y axis with a central gap of 14 cm which allows non-interacting beam photons and e^+e^- pairs to pass through. A schematic drawing of the layout of the IE is shown in Figure 3.6. Each block has dimensions 5.8 $cm \times$ 5.8 $cm \times 60.2$ cm and is 18.75 radiation lengths and 2.2 interaction lengths. A fast energy sum is performed on groups of nine blocks for use in the trigger.

3.9 Hadronic Calorimeter

The Hadronic Calorimeter (HC) [38] is located downstream of the IE. It measures the energy of hadronic particles within the acceptance of M2. The HC also plays a crucial role in the first level of triggering by providing a fast sum of the hadronic

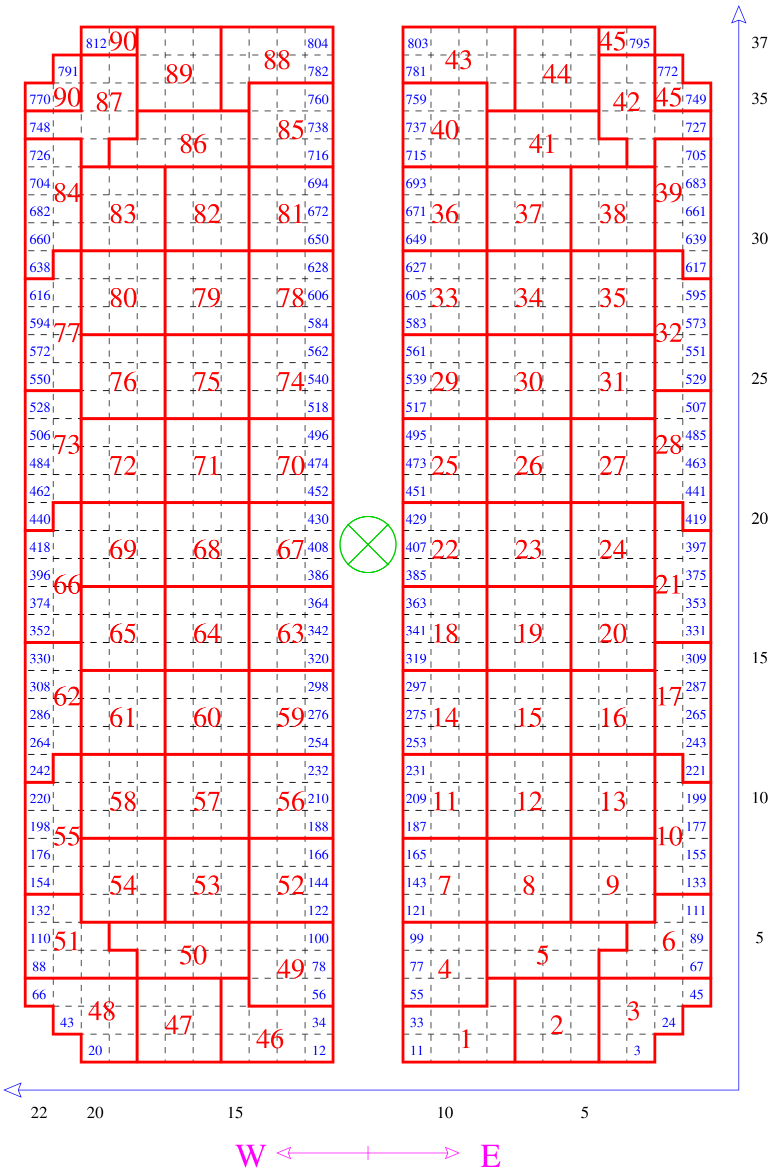

Figure 3.6: Schematic of the Inner Electromagnetic Calorimeter showing block layout (dashed lines) and trigger summer groupings (heavy lines).

energy in each event. The HC consists of 28 active scintilator planes separated by 28 planes of iron which absorb energy. The scintillating planes are divided into tiles as shown in Figure 3.7. Scintillation light created in the tiles is collected by

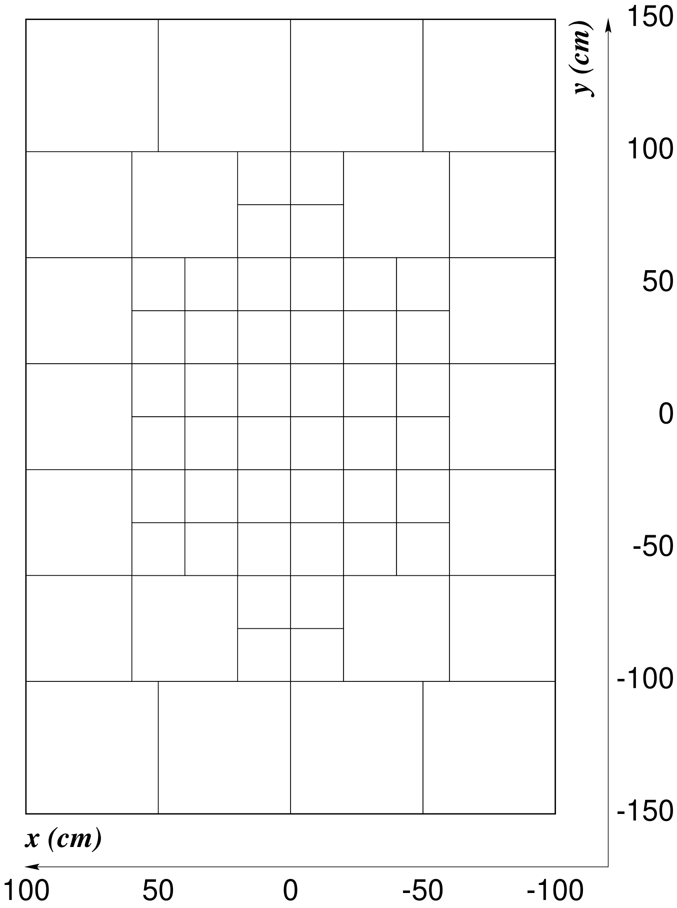

Figure 3.7: Schematic of the Hadron Calorimeter showing the configuration of the tiles.

wave shifting fibers which are mated to clear fibers at the tile's edge. The clear fibers are routed to phototubes at the edge of the detector. The HC is 219 *cm* long and 7.8 interaction lengths.

3.10 Muon Detectors

The fact that pions and muons have very similar masses makes identification by Čerenkov thresholds possible only in very limited momentum ranges. Instead, we exploit the fact that muons interact weakly in material to make the identification. Thick blocks of iron are used to range out showers from electrons, pions and other hadrons. Particles detected beyond the iron are likely to be muons.

3.10.1 Outer Muon System

The outer muon system uses the steel of the second dipole magnet (M2) as its filter. Muon hits are detected in resistive plate chambers. The detectors cover the region outside the M2 aperture.

3.10.2 Inner Muon System

The inner muon system consists of three stations of scintillating hodoscopes. Each station is proceeded by a steel block. The widths of the three steel blocks are 61 cm, 129 cm and 68 cm from upstream to downstream.

3.11 Trigger

In order to identify and select physically interesting events and to reduce the data rate to an acceptable level, a triggering system is used. FOCUS employs two levels of trigger referred to as the Master Gate and the Second Level Trigger. High speed detector elements placed at various strategic locations throughout the spectrometer provide the summary information on which the trigger decisions are based.

3.11.1 Trigger Elements

There are seven scintillating hodoscopes in the experiment which are used exclusively for triggering. In addition, summary information from the IE, HC, OM and PWC's are also used in the trigger.

The **AM** and **AMD** are scintillating walls upstream of the experimental target. They are used to detect beam halo particles — most likely muons produced in the liquid deuterium primary target. The coincidence of **AM** and **AMD** is used as a veto for single muon (semileptonic) and dimuon (J/ψ) triggers in the Second Level Trigger.

TR1 is a small counter located just downstream of the target assembly and upstream of the E687 SSD system. It is used to detect charged tracks produced in the target. The **TR2** counter consists of four individual counters connected as a logical OR. It is located just downstream of the SSD's and detects the existence of charged tracks emerging from the silicon and entering the magnet. All Master Gate triggers require the logical AND of **TR1** and **TR2**. In this way all triggered events are required to have some sort of track in the silicon microstrip system.

The **OH** array consists of 24 counters combined in a logical OR. This array is just downstream of ST2 and upstream of the OE. It has a pair gap down the middle to avoid recording hits from e^+e^- pairs produced indirectly in photon electromagnetic interaction in the target. The **OH** is intended to count charged tracks in the outer part of the detector and therefore has a gap matched to the M2 aperture.

The OM provides an OR of all channels in each RPC tower as input to the trigger logic. The logic returns two OM trigger words. One for events consistent with one or more tracks and the second consistent with two or more tracks. These trigger words are used for semileptonic and J/ψ triggers.

The **H×V** array, located just downstream of the last PWC and just upstream of the IE, is actually two scintilator arrays — one horizontal and one vertical. This trigger element is intended to record the passage of charged tracks in the inner region. Like the **OH** it also has a pair gap. Unlike the **OH** the signals from it's individual counters are sent to fast trigger logic which is able to crudely count tracks. The **H×V** logic produces two signals. The first signal, $(\mathrm{H}\times\mathrm{V})_1$, indicates that at least one track has passed through the system, and the second signal, $(\mathrm{H}\times\mathrm{V})_2$, indicates that at least two tracks are present.

As mentioned in Section 3.8, a fast sum of IE energy is made. This information is used in two ways. First the total energy is used to augment the HC's determination of total hadronic energy, and second the IE energy is divided into six sections and a two body trigger signal is made that requires energy in two non-adjacent sections. This two body IE trigger is used in the J/ψ dielectron trigger.

A fast sum of energy deposited in the HC is also provided. This energy sum provides a strong signature of a hadronic interaction.

The final trigger elements are the **IM1** and **IM2** scintilator arrays in the inner muon system. These arrays provide both one body and two body trigger words to the Master Gate for use in semileptonic and J/ψ triggers.

3.11.2 The Master Gate

The Master Gate is the first level of triggering in FOCUS. Information from the trigger elements listed in the previous section are collected in the programmable Master Gate module [39] which uses combinations of this trigger information to produce 8 Master Gate trigger outputs. Each of the 8 triggers selects different types of physics and diagnostic events. The decision to trigger an event at the Master Gate level is made about 330 ns after the interaction.

Most of the data used in this analysis came in through the hadronic trigger. The hadronic trigger consists of an AND of **TR1**, **TR2** and hadronic energy greater than 18 GeV ($\mathrm{E_{HI}}$), as well as the two body requirement:

$$2\mathrm{B} \equiv (\mathrm{H} \times \mathrm{V})_2 \text{ OR } [(\mathrm{H} \times \mathrm{V})_1 \text{ AND OH}]$$

which requires that there are at least two tracks in the inner detector or one in the inner and at least one in the outer.

3.11.3 Second Level Trigger

Once the Master Gate trigger decision is made, a signal is sent to begin reading out an event. Simultaneously the Second Level Trigger logic begins to work on its triggering decision. Approximately 2.5 μs later the Second Level decision is made and the event is either readout or the buffers are reset.

Again, the events used in this thesis come in primarily through the hadronic trigger. In the Second Level there are two additional requirements made for hadronic events. The first is a minimum IE energy sum and the second is a PWC hit multiplicity that is consistent with 4 tracks in the system.

3.12 Data Acquisition

Events passing the Second Level Trigger are readout and written to tape for future analysis. It takes about 1 ms to readout a event. During this time no other events can trigger the system. This period is known as the deadtime. If the event fails the Second Level Trigger there is about 1.5 μs of deadtime as the system resets. Figure 3.8 shows the layout of the Data Acquisition (DAQ) system which is described in detail elsewhere [40]. Digitized information on timing, charge and hits is collected through a direct VME interface, by a SGI Challenge L computer,

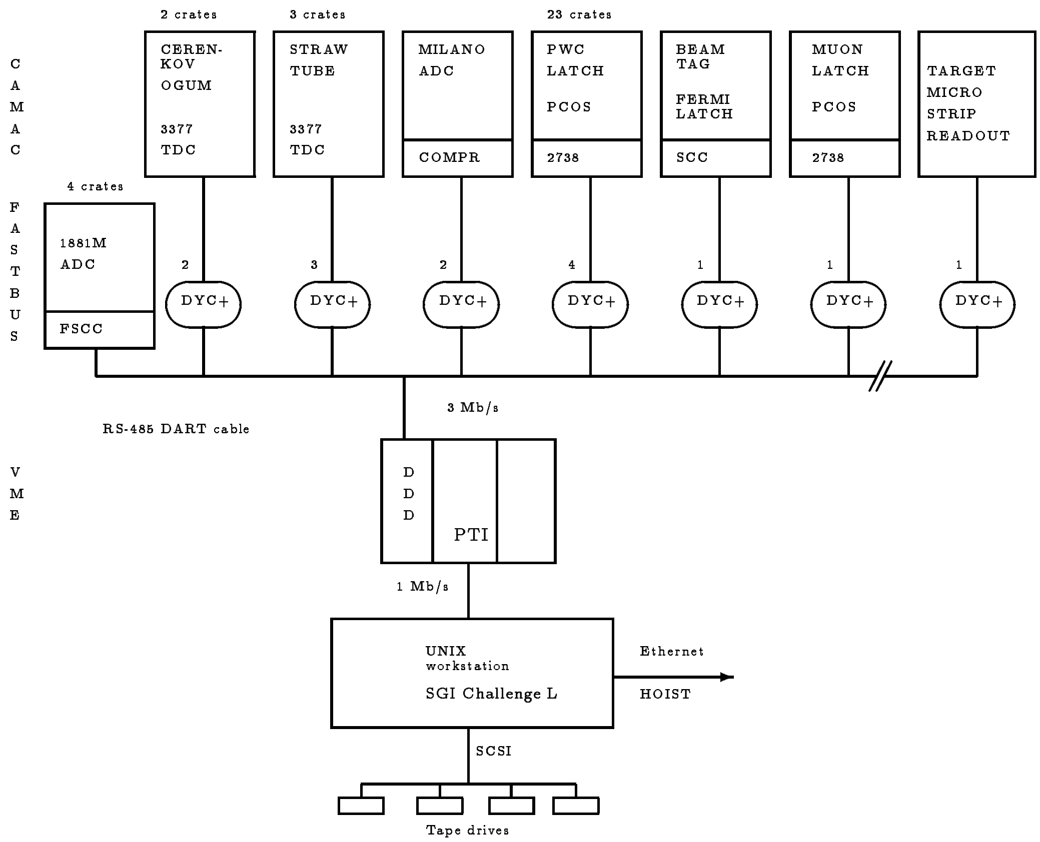

Figure 3.8: Overview of the DAQ layout.

which assembles the event and saves it to disk. Once a run is complete — typically about 30 minutes of data taking and 1 million triggered events — the data are written to an 8 *mm* tape.

Chapter 4

Data Reconstruction

4.1 Reconstruction Algorithms

4.1.1 SSD Tracking

The SSD track finding (or tracking) is a three step algorithm[1]. First, strips recording a hit are grouped into clusters. Then projections of hit clusters are found in each of the three measurement directions. Finally, these projections are combined into tracks.

Groups of no more than three hit strips are gathered into hit clusters. The total collected charge — determined by adding the analog-to-digital converter (ADC) counts of all channels in the cluster — is used to determine if the cluster is consistent with the passage of a single minimum ionizing particle (MIP) or if more

[1] The algorithm described here pertains to the original 12 planes of E687 SSD's only.

than one track contributed to the cluster. The actual cluster location is determined by weighting the hit strip positions by the strip ADC counts to determine the cluster centroid.

Projections are found by looking for combinations of clusters in different planes of the same orientation that fit a straight line hypothesis. Projections must fit a straight line with χ^2 per number of degrees of freedom (χ^2/ndf) of less than three and they must contain clusters from at least three of the four planes. Clusters are allowed to be shared among 3-plane projections, but sharing is only allowed in the first plane of 4-plane projections.

Tracks are formed by combining projections from each of the three views. They are required to have $\chi^2/\text{ndf} < 8$. Tracks with shared projections are arbitrated based on the lowest χ^2/ndf and tracks with nearly identical parameters are reduced to a single track.

In E687, the spatial resolution for tracks in the high resolution region of the SSD was found to be

$$\sigma_x = 11.0\mu\text{m}\sqrt{1 + \left(\frac{17.5\ \text{GeV}/c}{p}\right)^2} \tag{4.1}$$

$$\sigma_y = 7.7\mu\text{m}\sqrt{1 + \left(\frac{25.0\ \text{GeV}/c}{p}\right)^2} \tag{4.2}$$

and the resolution for a track in the SSD low resolution region is about twice as large. The constant term is the intrinsic resolution of the detector and the momentum dependent term comes from the multiple Coulomb scattering of the track in the silicon planes. In E687 the hit location was given by the center of the strip in the cluster with the most collected charge, instead of the cluster centroid. The FOCUS resolution using the centroid method is about 10% better than the resolutions shown in Equations (4.1) and (4.2).

4.1.2 Vertexing

For a given set of n SSD tracks a vertex location is found by minimizing

$$\chi^2 = \sum_{i=1}^{n} \left[\frac{x - (x_i + x'_i z)}{\sigma_{x,i}}\right]^2 + \left[\frac{y - (y_i + y'_i z)}{\sigma_{y,i}}\right]^2 \tag{4.3}$$

with respect to the vertex position coordinates x, y and z where x_i, y_i, x'_i and y'_i are the track intercepts and slopes and $\sigma_{x,i}$ and $\sigma_{y,i}$ are the SSD track errors.

In FOCUS, vertex track selecting, locating and booking are guided by a software package known as DVERT. With DVERT the user selects a group of tracks that are suspected to form a vertex (*e.g.* D decay vertex), and the routine returns the best vertex location and the confidence level (CL). If the vertex is found to be satisfactory (typically with CL $> 1\%$), the vertex can be booked and the vector associated with the combined tracks (or parent state) is available for use as a track in the formation of other vertices. Hit information from the target silicon detectors is used at this point to improve track parameters. The target silicon information is used after vertexing to avoid using hits from upstream of the track's point of

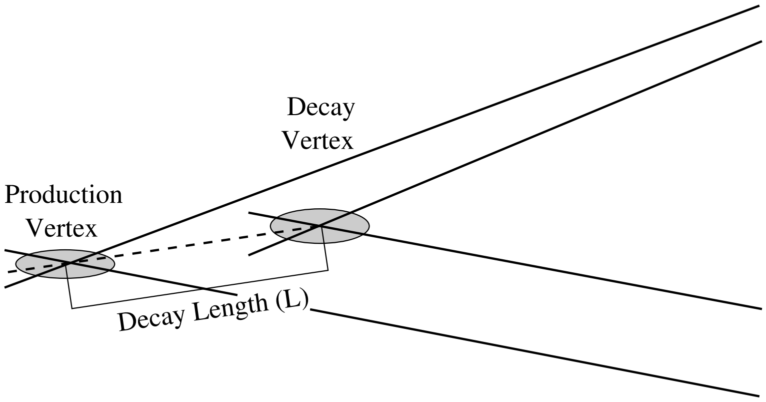

Figure 4.1: Schematic of the charm production and decay vertices. The ellipses represent the vertex resolution and the decay length is a measure of the production and decay vertex separation.

origin.

The hallmark of charm decay is the relatively long, weak scale lifetime ($\sim 10^{-13}$ s). This means that for charm particles with significant momentum one expects a measurable separation between the point of production and the decay. Figure 4.1 is an illustration of typical charm production and decay vertices showing the vertex separation. DVERT uses the decay vertex tracks to construct a charm particle track vector which is then used as a seed to nucleate the production vertex. This is achieved by repeatedly looping over all available tracks to find the vertex which includes the most tracks and has CL $> 1\%$.

Once the production and decay vertices are booked, DVERT provides routines to determine the significance of the vertex separation (ℓ/σ_ℓ), and vertex isolation. Vertex isolation looks at the CL for including other tracks in a vertex.

The isolation cut used in this analysis requires that the CL for including any of the decay vertex tracks in the production vertex is less than 1%.

4.1.3 PWC Tracking

The tracking algorithm in the PWC begins with single view projections as was done in the SSD system. The first step is to extrapolate SSD tracks from the non-bend view (x view) into the PWC system to look for hits forming x view projections. Projections, formed independently in the remaining three views, are combined with the x projections to form tracks. Unused x view hits are gathered into additional x projections and these are combined with the remaining u, v and y projections to form tracks.

Each track must have hits in at least three out of the five chambers and x projections from SSD extrapolated tracks must have a hit in P0. No more than four missing hits are allowed and no more than two missing hits in a single chamber. The track slopes and intercepts are determined by a linear least squares fit to the PWC hits associated with the track. For tracks passing through the M2 the bend in the y direction is also included as a fit parameter.

4.1.4 Linking PWC and SSD Tracks

The tracks reconstructed in the SSD and PWC systems are linked by extrapolating both sides to the z location of the M1 bend center. A global least squares fit to both the SSD and PWC hits is used to determine if the two track segments are consistent with being a single track. The links are arbitrated based on the χ^2/ndf. A maximum of two PWC tracks are allowed to be linked to a single SSD track. The second link is allowed to account for e^+e^- pairs from photon conversion that have a negligible opening angle in the SSD system, but are separated into two distinct tracks when they pass through the analysis magnet.

4.1.5 Momentum Determination

Track momenta are measured by determining the deflection angle in one of the two large aperture analysis magnets. The M1 deflection is used for tracks that are found only in the first three PWC stations. Typically these tracks are lower momentum tracks and therefore their deflection in M1 is of such an angle that they miss the M2 aperture, or they are swept out of the spectrometer by the higher field in M2. Magnet M2 is operated at a higher field so that high momentum tracks which are only slightly deflected by M1 will experience a larger bend in M2 leading to a better determination of momentum.

The deflection is measured by comparing the track's slope before and after passing through the magnet. For momenta measured in M1 the resolution is approximately given by (measured in E687 data)

$$\frac{\sigma_p}{p} = 0.034 \times \frac{p}{100\ \mathrm{GeV}/c}\sqrt{1+\left(\frac{17\ \mathrm{GeV}/c}{p}\right)^2}, \tag{4.4}$$

and corresponding resolution for momenta determined in M2 is

$$\frac{\sigma_p}{p} = 0.014 \times \frac{p}{100\ \mathrm{GeV}/c}\sqrt{1 + \left(\frac{23\ \mathrm{GeV}/c}{p}\right)^2}. \tag{4.5}$$

For low momentum tracks the resolution is limited by multiple Coulomb scattering, and at high momentum the resolution is limited by hit position resolution. The latter is primarily due to the wire spacing and to a lesser degree the alignment. Alignment problems tend to cause systematic shifts in momentum. Chapter 5 describes a technique that was used to address systematic shifts in momentum related to alignment problems.

4.1.6 Čerenkov Particle Identification

FOCUS uses a Čerenkov algorithm known as CITADL which is based on particle hypothesis likelihoods for the stable charged particles $e^\pm$, $\pi^\pm$, $K^\pm$ and $p^\pm$ (the muon is too similar in mass to the pion to be separately identified by its Čerenkov light production). For each track, likelihoods $\mathcal{L}$ for each particle hypothesis are determined by observing the status of cells in the track's $\beta = 1$ Čerenkov light cone. If the number of photoelectrons expected in cell i for a track of given momentum under a particular particle hypothesis is μ_i then the Poisson probability of that cell firing is $(1-e^{-\mu_i})$. In addition the cell has an accidental firing probability, a_i.

Then the full contribution to the likelihood for cell i is

$$\mathcal{L}_i = \begin{cases} (1 - e^{-\mu_i}) + a_i - a_i(1 - e^{-\mu_i}) & \text{if the cell is on} \\ 1 - [(1 - e^{-\mu_i}) + a_i - a_i(1 - e^{-\mu_i})] & \text{if the cell is off} \end{cases} \tag{4.6}$$

In general the accidental rate is different for each cell and it is dependent on the instantaneous rate in the spectrometer.

CITADL provides a set of χ^2-like variables $W(i) \equiv -2\log(\mathcal{L})$ where i ranges over the four particle hypotheses. The hypothesis with the lowest W is the most likely. These variables will be used in the following ways:

- Separate one hypothesis from another with

  $$\Delta W_{i,j} \equiv W(j) - W(i) > n$$

  such that hypothesis i is n units of W more likely then hypothesis j.

- Separation of a hypothesis from the minimum hypothesis with

  $$\Delta W_{i,\min} \equiv W(\min) - W(i) > n.$$

  This selection is used to ensure that the chosen hypothesis is not wildly less likely then some other hypothesis.

4.1.7 Electron Identification

The electron identification provided by the Čerenkov system is reliable only up to the momentum where the pions are also above the Čerenkov threshold. For tracks which are only observed upstream of M2 the pion threshold (for C1) is about 8.5 GeV/c, while for five chamber tracks the threshold (C3) is 17 GeV/c. For tracks above these thresholds electron identification requires the use of the electromagnetic calorimeters (IE and OE).

The details of shower clustering and energy calculation differ in the inner and outer calorimeters (and are beyond the scope of this discussion), but both systems identify a track as an electron by comparing the energy (E) collected in the calorimeter cluster associated with the track to the track's momentum (p). The energy of an electron is typically fully contained in the electromagnetic calorimeter, while hadrons generally leave only a fraction of their energy in the system, and muons leave almost no energy. Therefore a track and cluster combination with the ratio $E/p \approx 1$ has a high probability of being an electron.

4.1.8 Muon Identification

In the Inner Muon system, muons are identified by requiring hits in at least four of the six hodoscope planes. If the track momentum is below 10 GeV/c then only two hits are required. If the required number of hits are present then a χ^2 is calculated which gives a measure of the deviation of the hits from the extrapolated track. The hit positional errors used in the χ^2 calculation include both the scintillator paddle granularity and the expected multiple Coulomb scattering in the iron. This algorithm is described in detail in reference [41].

The methodology of muon identification in the Outer Muon system is similar to that used in in the inner system, except that it is complicated by the presence of a magnetic field in the M2 iron (see Ref. [42]).

Both systems provide muon identification confidence levels, which are set to zero when there are too few hits.

4.2 Data Processing

The FOCUS collaboration recorded 5926 tapes of good photon interaction data. Each data tape has a capacity of 4.5 Gigabytes which holds on average 1.1 million triggered events for a total of 27 Terabytes and 6.5 billion events. The data were processed in three collaboration wide stages, in order to make it manageable for individual analyses. The three stages were known as PassOne, Skim1, and Skim2. These collective processing stages took nearly two years to complete.

4.2.1 PassOne

PassOne was conducted on the Fermilab processing farms using CPS [43], a distributed computing package developed and maintained by Fermilab's Computing Division. CPS has been used by several experiments including E687. CPS groups together a server node and a cluster of about ten worker nodes into a computing farm. In this way a single data tape can be processed in parallel on ten computers.

At its peak, PassOne processing used 8 farms consisting of nearly 90 worker nodes.

During PassOne all the major reconstruction algorithms were run. This stage of processing was the most computationally intense. The reconstructed data were added to the raw data and written to tape. Each tape of input corresponded to a single tape of PassOne output. The addition of the reconstructed data to the output tape was offset by compressing raw data blocks, by rejecting events with certain kinds of reconstruction errors (*e.g.* too many hits) and from very loose selection cuts (*e.g.* requiring at least one track in the SSD's). About 10% of events were rejected at the PassOne level.

4.2.2 Skim1

At the next level of processing, known as Skim1, data from the PassOne output tapes was split into six separate streams (known as superstreams to distinguish them from the output of Skim2) based on physics selection criteria (see Table 4.1). This splitting process resulted in more manageable data sets ranging in size from 200 to 500 tapes. In addition to splitting the data, some reconstruction algorithms were rerun to fix problems discovered in the original PassOne algorithms.

The Skim1 processing was carried out at Vanderbilt University and the University of Colorado. Each used their own locally produced control software, but both institutions relied on large clusters of computers and tape stackers. Unlike PassOne, Skim1 was primarily limited by the speed of tape reading and writing.

4.2.3 Skim2

The final stage of collective data processing, referred to as Skim2, further split the data into specific physics topics. In many cases these "substreams" were tailored to the specification of a individual collaboration member. Each of the Skim1 superstreams was processed at a single institution. The specifics of each Skim2 setup varied from skim to skim, but most of the skims used skim control software known as the Generalized Skim Framework (GSF). The GSF maintained databases and provided data processing control, disk management and permanent skim record keeping.

All but a few of the Skim2 substreams fit on less than 100 tapes and many fit on fewer than 25 tapes. These small data sets allow individual collaborators to conveniently work with the data at their home institutions, and encourage studies that would otherwise be logistically difficult.

Table 4.1: Description of the six Skim1 superstreams with their Skim2 computing institutions.

Super-stream	Physics Topics	Skim2 Institution
1	Semi-leptonic decays	Puerto Rico
2	Topological vertexing and K_S	Illinois
3	Rare decays and Calibration	CBPF, Brazil
4	Baryons	Fermilab
5	Light quark states	UC Davis
6	Meson hadronic decays	UC Davis

Chapter 5

Correcting the Mass Scale

In the FOCUS spectrometer, momentum of charged particles is calculated by measuring the change in the trajectory of a track after it passes through one of two large aperture dipole magnets. This method relies on accurate, high resolution tracking information provided by the SSD and PWC systems, but the tracking system is only as good as its calibration and alignment.

Although there are no obvious logical flaws in the alignment procedure used for the tracking system during the reconstruction, two problems have appeared in reconstructed masses, which can be attributed to inaccuracies in the chamber alignment or magnet field constants. The first problem is that positively charged tracks have systematically low momenta while negatively charged tracks are systematically high. This was first noticed as a shift in the peak mass of $D^+ \to K^-\pi^+\pi^+$ versus $D^- \to K^+\pi^-\pi^-$. The shift is caused by an effective tilt between tracking regions and is discussed in Section 5.2. The second problem is that the overall momentum scale is shifted high. This effect can be seen in the reconstructed masses of several states which are high by 2 to 5 MeV/c^2. It is the result of an effective stretching of a tracking region or regions and is discussed in Section 5.3.

5.1 Calculating Momentum and Mass

By approximating that the track bend occurs at a single point in the center of the dipole magnet, the formula for calculating the track momentum p is based on the difference between the slopes of two track segments:

$$p = \frac{K}{\Delta s} \tag{5.1}$$

where K is the magnet kick and Δs is the change in slope.

The mass of a particle which decays into n daughters is given by:

$$m^2 = (E_1 + ... + E_n)^2 - (\mathbf{p}_1 + ... + \mathbf{p}_n)^2, \tag{5.2}$$

and since $m_i^2 \ll p_i^2$

$$m^2 \simeq \sum_{i=1}^{n} m_i^2 + \sum_{i=1}^{n} \sum_{j=1}^{n} p_i p_j (1 - \cos\theta_{ij}) \tag{5.3}$$

where θ_{ij}[1] is the opening angle between tracks i and j.

[1] When $i = j$, $(1 - \cos\theta_{ij}) = 0$.

If the momenta of the daughter tracks are mismeasured by amounts δp_1,... δp_n then

$$(m+\delta m)^2 = \sum_{i=1}^{n} m_i^2 + \sum_{i=1}^{n}\sum_{j=1}^{n}(p_i+\delta p_i)(p_j+\delta p_j)(1-\cos\theta_{ij}). \tag{5.4}$$

Neglecting terms of order $(\delta m)^2$ and $(\delta p)^2$ we get

$$m^2 + 2m\,\delta m \simeq \sum_{i=1}^{n} m_i^2 + \sum_{i=1}^{n}\sum_{j=1}^{n} p_i p_j (1-\cos\theta_{ij})\left(1+\frac{\delta p_i}{p_i}+\frac{\delta p_j}{p_j}\right)$$

$$2m\,\delta m \simeq \sum_{i=1}^{n}\sum_{j=1}^{n} p_i p_j (1-\cos\theta_{ij})\left(\frac{\delta p_i}{p_i}+\frac{\delta p_j}{p_j}\right). \tag{5.5}$$

In the case of a two body decay Equation (5.5) reduces to

$$\delta m \simeq \frac{1}{2m}\left(\frac{\delta p_1}{p_1}+\frac{\delta p_2}{p_2}\right)(m^2 - m_1^2 - m_2^2). \tag{5.6}$$

5.2 Tilted Tracking Region

If there exists a systematic uncorrected tilt ($\delta s = \sin\delta\alpha \simeq \delta\alpha$) between the two tracking regions on either side of a magnet, then the measured momentum is:

$$p' = \frac{K}{\Delta s + \delta\alpha}. \tag{5.7}$$

Here it is clear that the sign of Δs determines the sign of p'. Therefore, for a given tilt, one track charge will have a systematically higher momentum and the other will have a systematically lower momentum.

The tilt momentum shift δp in terms of the measured momentum is

$$\delta p = p - p' = \frac{p'^2 \delta\alpha}{K - p'\delta\alpha} \tag{5.8}$$

and the relative momentum error is

$$\frac{\delta p}{p} = \frac{p'\delta\alpha}{K} \tag{5.9}$$

where the charge of the track is the sign of p'.

Now it is possible to calculate the reconstructed mass error for a two track parent when there is an uncorrected tilt. Using the unsigned measured momenta p_+ and p_- for the positive and negative daughter tracks respectively, we plug Equation (5.9) into Equation (5.6) and get

$$\delta m \simeq \frac{\delta\alpha}{2mK}(p_+ - p_-)(m^2 - m_+^2 - m_-^2). \tag{5.10}$$

So, the mass scale effect creates a sizable mass shift when the difference between the negative and positive track momenta is large. When averaged over the full range of positive and negative momenta, the peak mass value is not affected, but the overall mass resolution is broadened.

The value of $\delta\alpha$ can be measured by plotting the fitted peak mass for a suitable two body decay (such as $K_s \to \pi^+\pi^-$) versus the momentum difference, $p_+ - p_-$. The points are expected to lie on a line with slope

$$\frac{\delta\alpha}{2mK}(m^2 - m_+^2 - m_-^2).$$

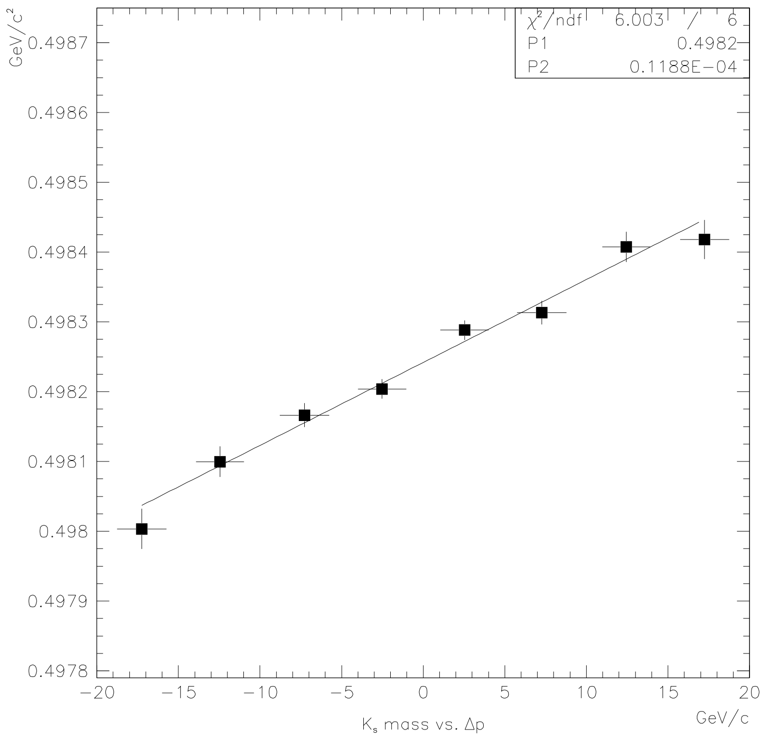

Figure 5.1: The asymmetry generated about magnet M2, for runs in the range of 10 200 to 11 800. The slope corresponds to $\delta\alpha = -47$ microradians.

Figure 5.1 shows the slope due to tilted tracking regions about magnet M2.

In subsequent sections, this tilt effect will be referred to as the asymmetrical effect because of its unequal treatment of positive and negative tracks.

5.3 Stretched Tracking Region

Effective stretching (or squashing) of a tracking region can result from at least three different geometry or calibration problems.

1. The magnet kick value is wrong by δK. Then:

$$\frac{\delta p}{p} = \frac{\delta K}{K} \tag{5.11}$$

   where K is the magnet transverse momentum kick.

2. The chamber positions z scale is off by δz. Then:

$$\frac{\delta p}{p} = \frac{\delta z}{z} \tag{5.12}$$

   where z is the length of the tracking region.

3. The chamber wire spacing is wrong by δy. Then:

$$\frac{\delta p}{p} = \frac{\delta y}{y} \tag{5.13}$$

   where y is chamber pitch in the y direction

For a fixed calibration, Equations (5.11)–(5.13) all have the form

$$\frac{\delta p}{p} = \text{constant} \equiv \mathcal{R}. \tag{5.14}$$

When plugged into Equation (5.6) we get

$$\delta m \simeq \frac{\mathcal{R}}{m}\left(m^2 - \sum_{i=1}^{n} m_i^2\right). \tag{5.15}$$

The stretching (squashing) effect, systematically raises (lowers) the momenta of both positive and negative tracks. The effect on the parent mass is independent of the individual track momenta. The value of $\mathcal{R}$ can be measured by the mass shift on any of a large number of fully charged decays where the parent mass has been accurately measured elsewhere.

The stretching effect will be referred to as the symmetrical effect in contrast to the asymmetrical effect of Section 5.2.

5.4 Correcting the Mass Scale

Perhaps the best way to fix the mass scale problems discussed in the previous sections would be to determine which alignment constants are wrong, fix them, and rerun the reconstruction. The obvious drawback to this approach is that it requires a data processing effort on the scale of PassOne or Skim1. Also, determining the correct calibration constants would be a difficult job for a number of reasons. First, chambers drift over time, and therefore accurate alignment could require a large number of separate run periods each with its own constants. Also, different calibration problems can cause effects that are indistinguishable, such as the three problems noted in Section 5.3. With the run over, the ability to design and run beam based calibration methods which could resolve these ambiguities is lost.

A more practical fix is to apply a post-reconstruction correction to the charged track momenta based on the measured values of $\delta\alpha$ and $\mathcal{R}$. In fact there are four constants, because each analysis magnet will have its own $\delta\alpha$ and $\mathcal{R}$. Also, these correction factors are run-dependent.

Corrected track momentum are calculated with

$$p = p' \pm \delta p_A + \delta p_S \tag{5.16}$$

where p' is the measured momentum, δp_A is the asymmetrical momentum error described in Section 5.2, δp_S is the symmetrical momentum error of Section 5.3 and $\pm$ matches the charge of the track. Equation (5.16) can be written as:

$$p = p' \pm p\frac{\delta p_A}{p} + p\frac{\delta p_S}{p}. \tag{5.17}$$

Then plugging in the relations from (5.9) and (5.14) and rearranging gives:

$$p = \frac{p'}{1 \mp p'\frac{\delta\alpha}{K} - \mathcal{R}}. \tag{5.18}$$

Equation (5.18) relates the real momentum, p, to the measured momentum p', the magnet kick K and the two correction factors $\delta\alpha$ and $\mathcal{R}$. With properly measured correction factors this relationship should fix both the asymmetrical and the symmetrical mass problems.

Figure 5.2 shows the run dependence of the mass scale and asymmetry slope for K_s in M1 and M2. Several run ranges with significant differences were identified and are noted with vertical lines in Figure 5.2. Corrections are determined in each of these regions by a fit which minimizes the squared deviation from the mass of K_s, in several bins of asymmetry, as the two correction constants are varied. The corrected run dependent plots are shown in Figure 5.3.

As an independent check of this method the uncorrected and corrected J/ψ mass distributions are shown in Figure 5.4. The J/ψ represents the high end of the

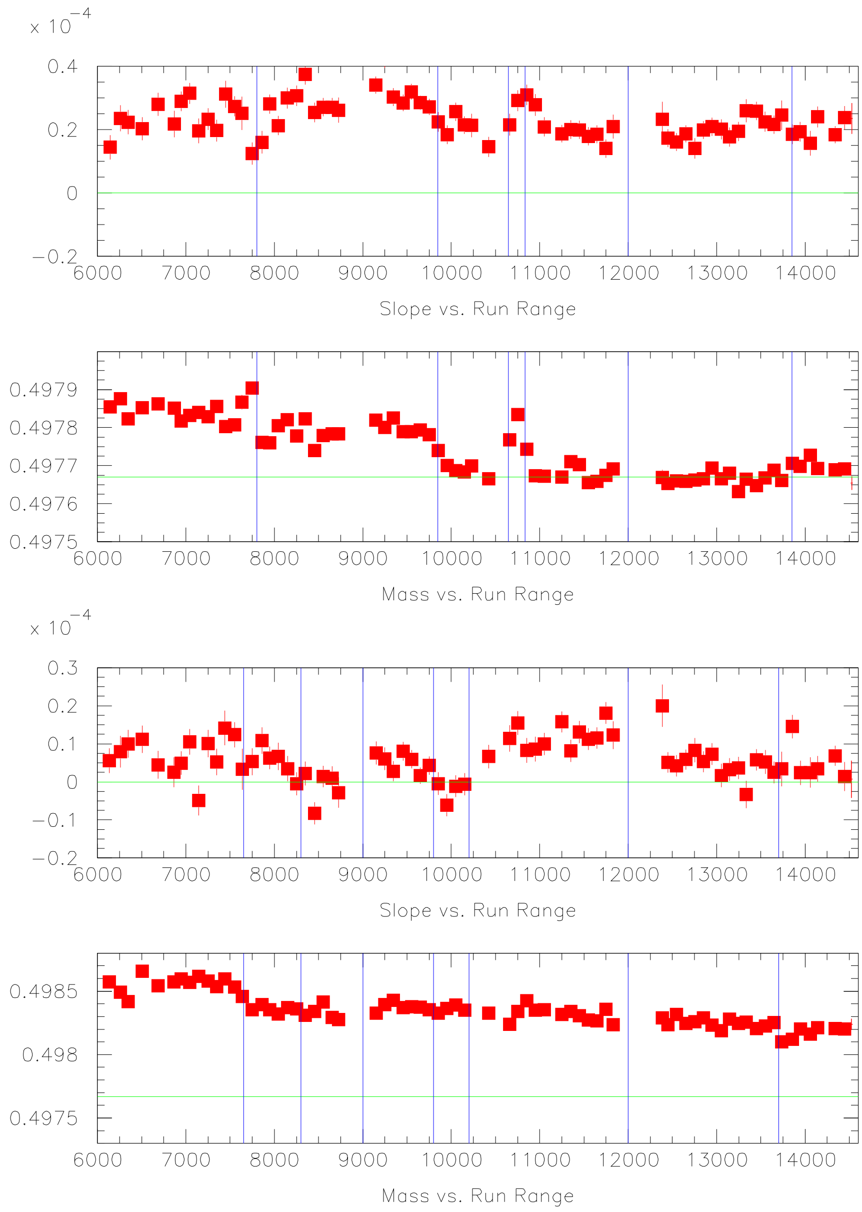

Figure 5.2: Run dependent mass scale and momentum asymmetry slope for M1 (top) and M2 (bottom). The vertical lines delineate the run periods where different correction constants were applied and the horizontal lines are the expected mass or slope.

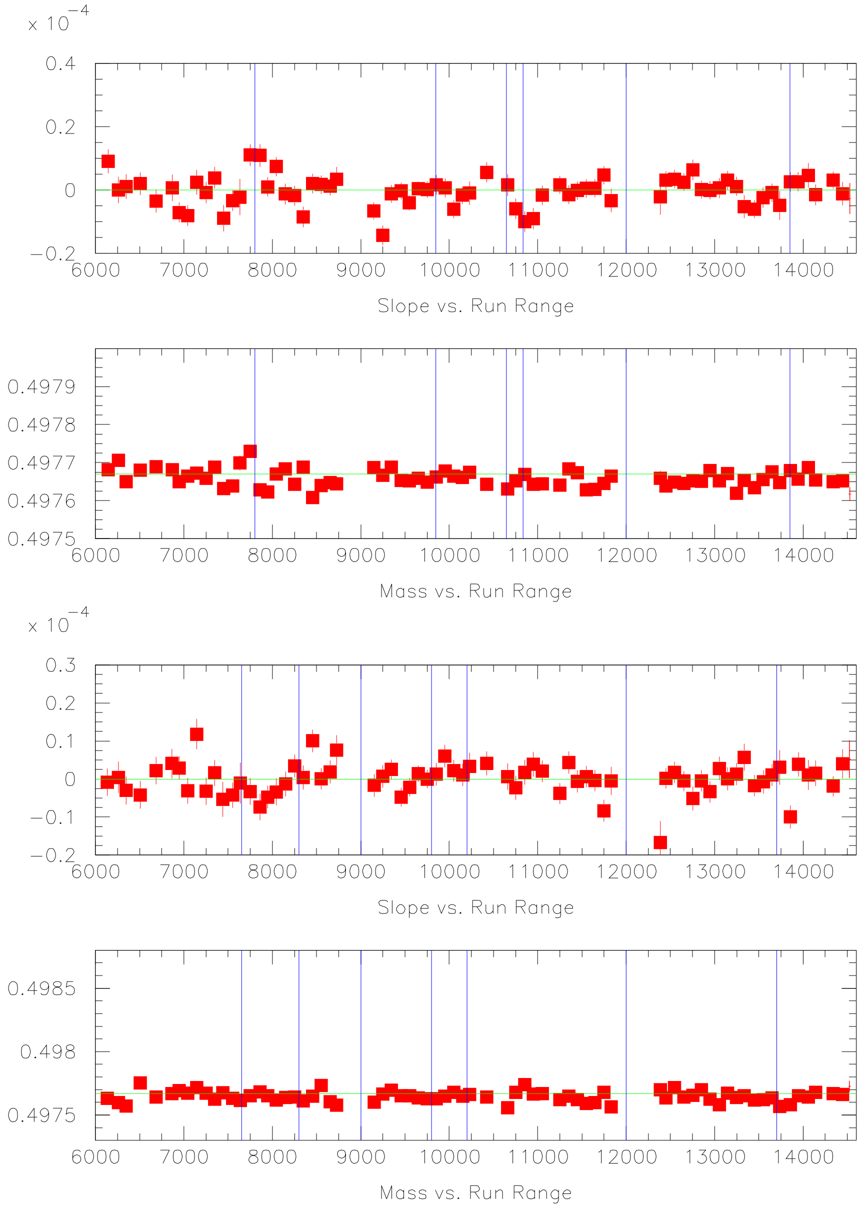

Figure 5.3: Corrected mass scale and asymmetry plots (compare to Figure 5.2).

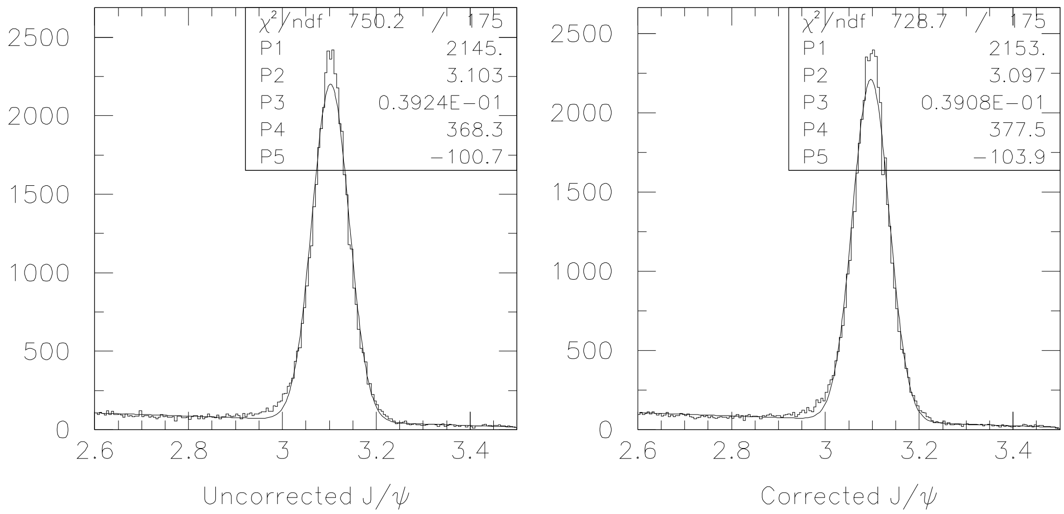

Figure 5.4: J/ψ mass (parameter P2) before and after the correction.

FOCUS mass scale. The J/ψ mass is shifted down 6 MeV/c^2 and is now completely consistent with the PDG value [8] of 3.09688 GeV/c^2. It is encouraging that the correction determined at the low mass of the K_s works well at the J/ψ mass.

Chapter 6

$D^0 \to K^+\pi^-$ Branching Ratio Measurement

6.1 Event Selection

The events used in this analysis are from Skim1 superstream 6. In this superstream events are chosen by a candidate driven selection routine known as SuperEZDEE. At Skim2 the golden mode skim was used. In the golden mode skim, events where the $K\pi$, $K\pi\pi$, $KK\pi$, or $K\pi\pi\pi$ SuperEZDEE skim bits were set are selected. At the last stage of skimming only events with the $K\pi$ skim bit are selected.

To minimize systematic effects, the same selection algorithm is applied to both the WS and RS modes. In fact, for most of the selection criteria the two modes are indistinguishable. The separation of WS and RS decays is achieved by using the decay chains

$$\begin{array}{l} D^{+*} \rightarrow D^0 \tilde{\pi}^+ \\ \qquad\quad \searrow K^- \pi^+ \text{ (RS)} \end{array}$$

and

$$\begin{array}{l} D^{+*} \rightarrow D^0 \tilde{\pi}^+ \\ \qquad\quad \searrow K^+ \pi^- \text{ (WS).} \end{array}$$

The production flavor of the neutral D is tagged (*i.e.* we know if it is a D^0 or a $\overline{D}^0$) by the sign of the soft tagging π ($\tilde{\pi}$). For RS decays the charge of the $\tilde{\pi}$ is the same as the charge of the D^0 daughter π, and in the case of WS decays the $\tilde{\pi}$ charge is opposite the daughter π charge. The D^* decay chain is identified by taking the difference of the $D^0\tilde{\pi}$ invariant mass and the D^0 reconstructed mass. Events with a D^* form a narrow peak at 145 MeV/c^2 (see Figure 6.1). This difference is known as the $D^* - D$ mass difference.

Requiring a $\tilde{\pi}$ candidate, with a $D^* - D$ mass difference of less than 200 MeV/c^2, is an excellent clean-up cut, and harsh additional clean-up cuts are not necessary. Therefore, the decision to use a selection cut is made only under the following conditions:

1. To match the cuts made at various levels of skimming.

2. To remove specific problem backgrounds.

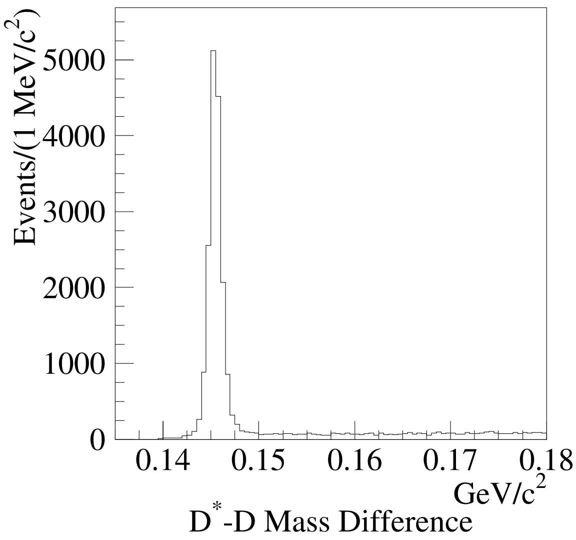

Figure 6.1: The $D^* - D$ mass difference for RS tagged $D^0 \to K^-\pi^+$ events.

3. To improve the signal to noise ratio only when there is minimal signal loss.

To avoid tuning cuts on data fluctuations most of the analysis cuts are set to reasonable (typically loose) values, and are varied at a later time to study possible systematic effects.

6.1.1 $K\pi$ Selection

A D^0 candidate consists of a pair of oppositely charged tracks that form a decay (or secondary) vertex and has a $K\pi$ invariant mass between 1.7 and 2.1 GeV/c^2. The D^0 candidate is used as a seed to locate a production (or primary) vertex consisting of at least two charged tracks in addition to the D^0. The primary vertex is required to be no more than 1 σ from the nearest target material and it must be separated from the secondary vertex by at least five times the separation error ($\ell/\sigma_\ell > 5$). Both the primary and secondary vertices must have confidence levels greater than 1%. The secondary vertex tracks must be inconsistent with originating in the primary vertex. This is achieved by requiring that the confidence level for each secondary track included in the primary be less than 1%.

$K\pi$ pairs with highly asymmetrical momenta are more likely to be background than signal. A cut is made on the momentum asymmetry, $\mathcal{A} = |p_K - p_\pi|/|p_K + p_\pi|$, to reject these candidates. As shown in Figure 6.2, the level of background varies with the D^0 momentum. The best background rejection is achieved by varying the cut point such that events satisfying

$$p_{D^0} > -160. + 280. \times \mathcal{A} \tag{6.1}$$

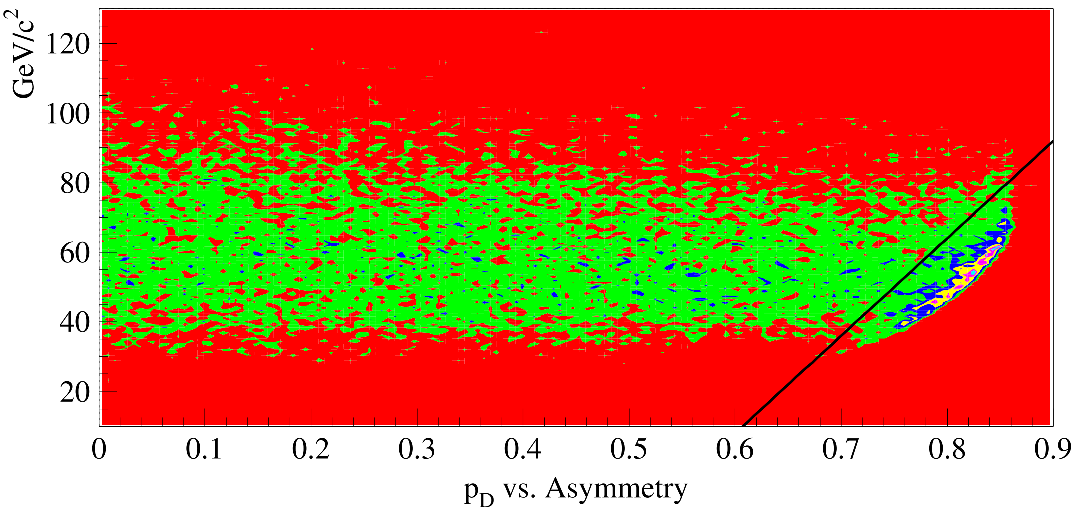

Figure 6.2: The D^0 momentum vs. $K\pi$ asymmetry. Events below and to the right of the solid line are rejected by the asymmetry cut.

are retained. Figure 6.2 shows the cut upper boundary.

The baseline Čerenkov particle identification cuts are intended to reject only unambiguously misidentified candidates. The following loose cuts are applied:

Kaon Candidate Requirements:

- $\Delta W_{K,\mathrm{min}} > -4$
- $\Delta W_{K,\pi} > 1/2$ (To match particle ID in SuperEZDEE skim)

Pion Candidate Requirements:

- $\Delta W_{\pi,\mathrm{min}} > -4$
- $\Delta W_{\pi,K} > -2$

A single track pair can pass these Čerenkov cuts as either $K^+\pi^-$ or $K^-\pi^+$. If both cases satisfy the cuts then two D^0 candidates are generated. If neither combination satisfies the cut, then the track pair is rejected.

Events with the decay $D^0 \to K^-\pi^+$ where the K has been misidentified as a π and the π has been misidentified as a K, produce false WS candidates. These doubly misidentified events form a broad peak in the $K^+\pi^-$ mass distribution centered on the D^0 mass (see Figure 6.3). When a real $\tilde{\pi}$ tag is present, a peak indistinguishable from the real WS signal appears in the $D^* - D$ mass difference. We treat this double misidentification background by imposing a hard Čerenkov cut on the sum $\Delta W_{K,\pi} + \Delta W_{\pi,K} > 8$, when the invariant mass of the $K\pi$ pair, with

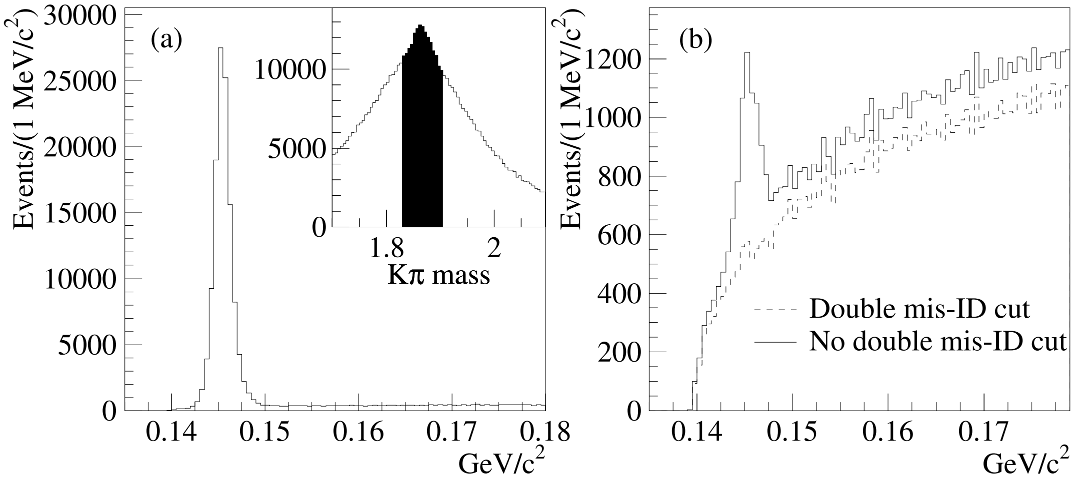

Figure 6.3: **a)** The $K\pi$ mass distribution (inset) and mass difference distribution for events in the D^0 signal region (shaded area of inset) for Monte Carlo events generated and selected as $D^0 \to K^-\pi^+$, but reconstructed as $K^+\pi^-$. **b)** The WS distribution from the same Monte Carlo events (reconstructed as selected) with and without the double mis-ID cut. No WS decays were generated.

the K and π particle hypotheses swapped, is within $4\,\sigma$ of the D^0 mass. Monte Carlo studies of this cut predict a double misidentification feed-through in the WS signal consistent with zero events (see Figure 6.3b), and at the 90% confidence level an upper limit of 5% of the observed WS yield.

A selection is made on the muon confidence level requiring that it be less than 1% for both D^0 candidate tracks. This cut targets background from the semimuonic decay $D^0 \to K^-\mu^+\nu_\mu$. This cut affects less than 0.5% of all events.

6.1.2 Soft Tagging π Selection

All tracks assigned to the production vertex are considered as potential $\tilde{\pi}$ candidates. The $\tilde{\pi}$ candidate must satisfy the Čerenkov condition, $\Delta W_{\pi,\min} > -4$, and be inconsistent with being a muon with μ confidence level less than 1%.

Additional cuts are made to remove background from $D^{0*} \to D^0\gamma$ (or $D^{0*} \to D^0\pi^0 \to D^0\gamma\gamma$) where a γ converts to e^+e^-. First, the charge deposited in the SSD by the track is required to be consistent with a single minimum ionizing particle, since one expects the e^+ and e^- from a pair conversion to both go in the direction of the original γ. Second, a combination of Čerenkov and electromagnetic calorimeter cuts are used. All $\tilde{\pi}$ candidates are required to have $\Delta W_{\pi,e} > 0$. For tracks depositing energy in the IE, the energy to momentum ratio (E/p) is required to be less than 0.8 or greater than 1.2. In the case of tracks leaving energy in the OE, with E/p in the range of 0.7 to 1.3 a selection is made requiring $\Delta W_{\pi,e} > 2$.

There is no arbitration to select the best $\tilde{\pi}$ candidate. Multiple $\tilde{\pi}$ are allowed and each $\tilde{\pi}$ is counted in the analysis with equal weight independent of the number of $\tilde{\pi}$ candidates found to be consistent with that D^0 candidate. If there is a $\tilde{\pi}$ tag with $D^* - D$ mass difference in the range 0.1425 to 0.1495 GeV/c^2, then all tags of the other sign are rejected. While applied symmetrically to both the RS and WS samples, this cut is a more effective clean up of the WS background, because there are 80 times more events in the RS signal region than in the WS signal region.

This cut eliminates a disparity in the WS and RS backgrounds due to a charge correlation with $\tilde{\pi}$'s from the other (associatively produced) charm particle in the event.

6.1.3 Correlated Backgrounds

The single mis-ID backgrounds from K^+K^- and $\pi^+\pi^-$, generate peaks in both the $K\pi$ mass plot and the $D^*{-}D$ mass difference. The insets in Figures 6.4a and 6.4b show the events passing the $K\pi$ selection cuts for K^+K^- and $\pi^+\pi^-$ Monte Carlo sets respectively. In the K^+K^- Monte Carlo events we see a broad peak centered about 100 MeV/c^2 below the D^0 mass. The $\pi^+\pi^-$ Monte Carlo events show a broad peak about 100 MeV/c^2 above the D^0 mass. For both reflections, the mass difference distributions for events in the D^0 signal region have well defined peaks in the D^* signal region. If not dealt with, these correlated tag backgrounds — which are as likely in the WS as in the RS — will tend to increase the branching ratio.

Finally a large D^0 Monte Carlo set is generated with all known decay modes except for $K\pi$, K^+K^-, and $\pi^+\pi^-$. The idea is to look for unexpected modes that may cause structured backgrounds due to correlated $\tilde{\pi}$'s. For example, doubly misidentified and partially reconstructed decays such as $K^-\pi^+\pi^0$ and $K^-\ell^+\nu$ can cause reflection tags for events under the D^0 mass signal. Figure 6.5 shows the $K\pi$ mass (inset) and mass difference in the D^0 signal window for events passing

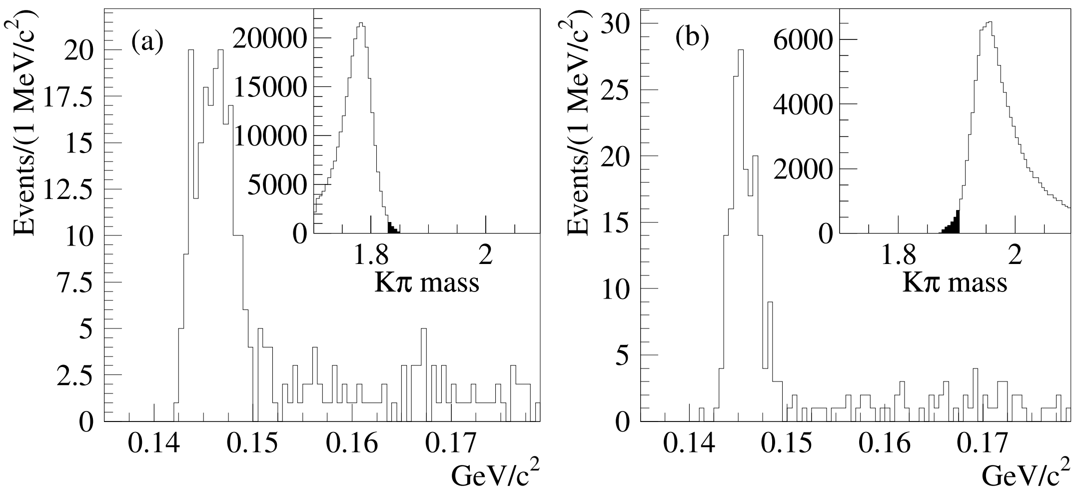

Figure 6.4: D^0 Monte Carlo events generated as decays to **a)** KK and **b)** $\pi\pi$, reconstructed and selected as $K\pi$. The inset plots show $K\pi$ mass distributions and the large plots show the mass difference distribution for events in the D^0 mass window (shaded area of inset plot).

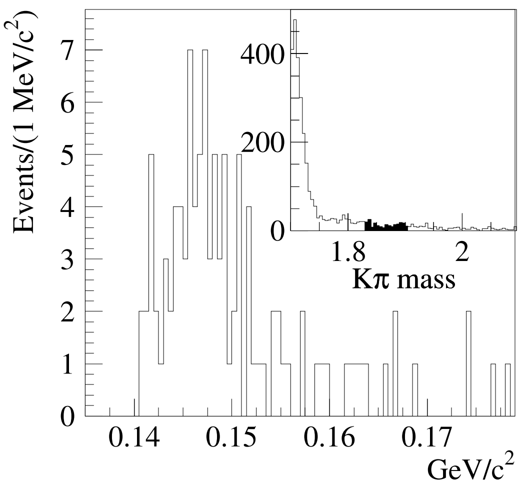

Figure 6.5: D^0 Monte Carlo events generated for all decay mode except $K\pi$, KK and $\pi\pi$, reconstructed and selected as $K\pi$. The inset shows the $K\pi$ mass distribution. The only structure is the reflection from partially reconstructed $K\pi\pi^0$ below 1.75 GeV/c^2. The large plot shows the mass difference distribution for events in the D^0 mass window.

Table 6.1: Summary of the correlated D^* backgrounds and their effects on the $K\pi$ mass and $D^* - D$ mass difference.

Source	Effect on $K\pi$ Mass	Effect on Mass Difference
$K^-\pi^+$ double mis-ID Figure 6.3	Very broad bump peaked at the D^0 mass.	Narrow peak which is indistinguishable from the D^* signal.
K^+K^- single mis-ID Figure 6.4a	Broad bump peaked below the D^0 mass.	Slightly wider peak in the D^* signal region.
$\pi^+\pi^-$ single mis-ID Figure 6.4b	Broad bump peaked above the D^0 mass.	Slightly wider peak in the D^* signal region.
Partially reconstructed and/or mis-ID modes (*e.g.* $K^-\pi^+\pi^0$, $K^-\ell^+\nu$, $\pi^+\pi^-\pi^0$ etc.) Figure 6.5	Linear background under the D^0 mass.	Broad bump centered on the D^* signal.

the analysis selection. A broad bump is observed in the mass difference while the $K\pi$ mass is structureless in the vicinity of the D^0.

The most dangerous mis-ID background is the double mis-ID of $K\pi$. The Monte Carlo events show that when the particle identities of $K\pi$ are swapped and the mass is calculated, as in the case of double mis-ID, there is a broad structure peaked at the mass of the D^0 in the mass distribution (see Figure 6.3a inset). The mass difference distribution for the events in the D^0 signal region, shows a narrow peak which is indistinguishable from the RS signal (see Figure 6.3a). The double mis-ID cut from section 6.1.1 addresses this background.

6.1.4 A Method to Deal with Structured Backgrounds

To deal with the $\tilde{\pi}$ backgrounds discussed in the last section, the data is split into 1 MeV/c^2 wide mass difference bins, as illustrated in Figure 6.6. The $K\pi$ mass

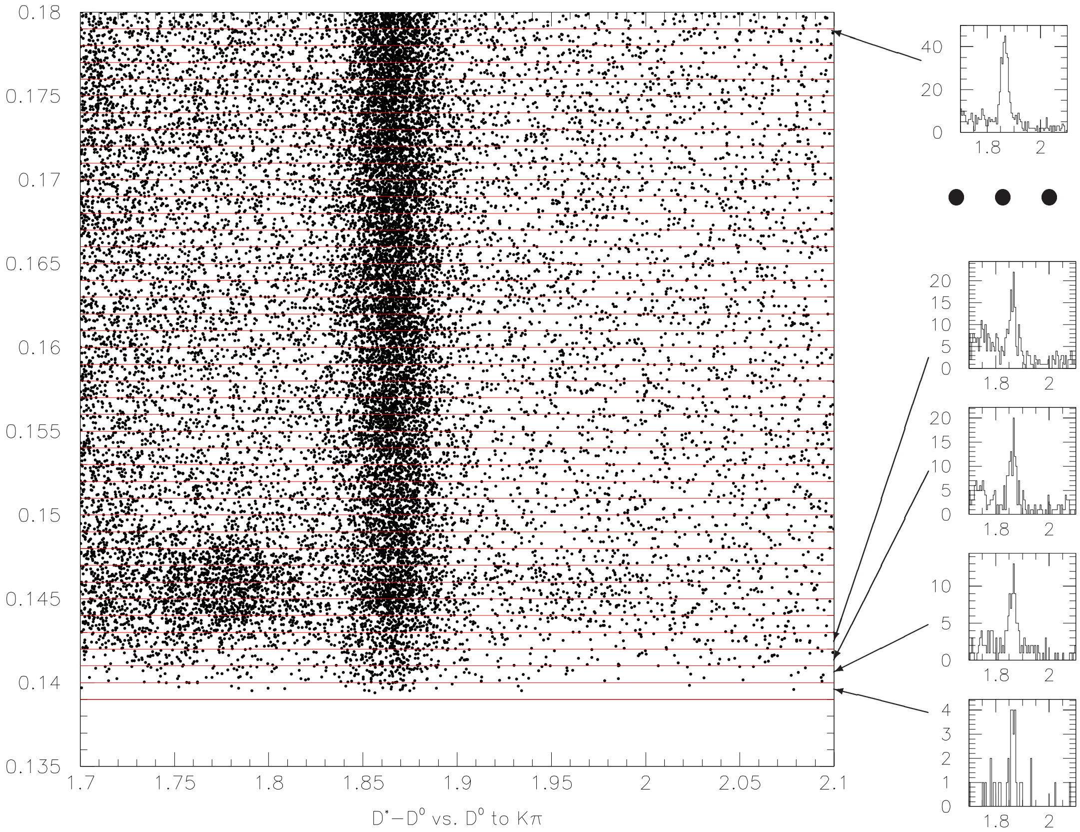

Figure 6.6: On the left is the WS $D^* - D$ mass difference plotted against the $K\pi$ mass. In the new method, this plot is sliced into 1 MeV/c^2 bins in mass difference. The $K\pi$ mass is plotted and fit in each bin. The resulting fitted D^0 yields are plotted at the appropriate mass difference (see Figure 6.9).

distribution for the data in each mass difference bin is fit for D^0 yield. The D^0 fit yield from each of the 80 $K\pi$ fits (40 each RS and WS) are plotted versus mass difference. The mass difference plots obtained through this procedure are made up of only the $D^0 \to K\pi$ contribution. This method transfers the task of isolating the reflections from the mass difference fit, where all the correlated backgrounds are peaked in the signal region, to the $K\pi$ mass fit, where the backgrounds peak outside the signal region.

The D^0 peak is fit to a single Gaussian and the K^+K^- and $\pi^+\pi^-$ reflections are fit to Monte Carlo line shapes. The remaining background is fit with a degree two polynomial. The Gaussian parameters are completely unconstrained, nevertheless, they are quite well behaved. Figures 6.7a and b show the distributions of the mass and width fit parameters normalized to errors.

The K^+K^- and $\pi^+\pi^-$ reflection Monte Carlo events where generated for all run periods. Nearly 6 million triggered events were generated for K^+K^- and about 8 million for $\pi^+\pi^-$. The Monte Carlo events are subjected to the same $K\pi$ selections as the data (described in Section 6.1). A $\pm 4\,\sigma$ cut is made about the D^0 in K^+K^- (or $\pi^+\pi^-$) mass to minimize the feed-through of $D^0 \to K^-\pi^+$ decays

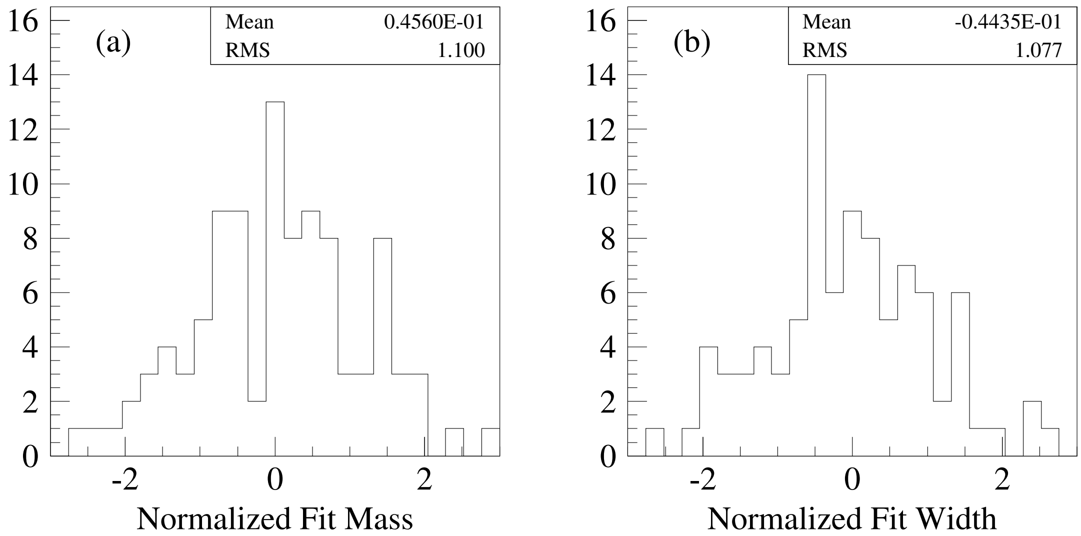

Figure 6.7: Distributions of the D^0 **a)** mass and **b)** width fit parameters normalized to errors. These plots show that the Gaussian fit to the D^0 signal is well behaved across the 80 fits.

from the other charm produced in association. The RS and WS tagged reflection distributions are combined to double the statistics. Combining the samples does not introduce any new error because the produced states, K^+K^- and $\pi^+\pi^-$, are charge conjugate eigenstates without separate RS and WS modes. The reflection shapes vary across the mass difference signal region. So, the reflections are also split into 1 MeV/c^2 mass difference bins. Away from the signal region, where the $\tilde{\pi}$ is not correlated with the decay, the reflection shapes are independent of mass difference and the reflection line shape used in these fits comes from a combined plot of all events in this region.

The K^+K^- and $\pi^+\pi^-$ reflection shapes each have one parameter in the fit, which scales the corresponding reflection histogram bin-by-bin to match the reflection contribution in the $K\pi$ mass histogram. The Monte Carlo samples are sufficiently large that neither scale factors is ever greater than 1/80. The scale factors are constrained to be positive.

The degree two polynomial background function gives a good description of both the random background and the unstructured D^0 backgrounds shown in Figure 6.5. It is not a good fit to the correctly identified $K\pi\pi^0$ reflection that is present at the low mass end of the plot. To avoid this reflection, the fit does not go below 1.75 GeV/c^2.

A typical fit of the $K\pi$ mass distribution from the mass difference signal region is shown in Figure 6.8. The fits to all 80 $K\pi$ mass plots are shown in

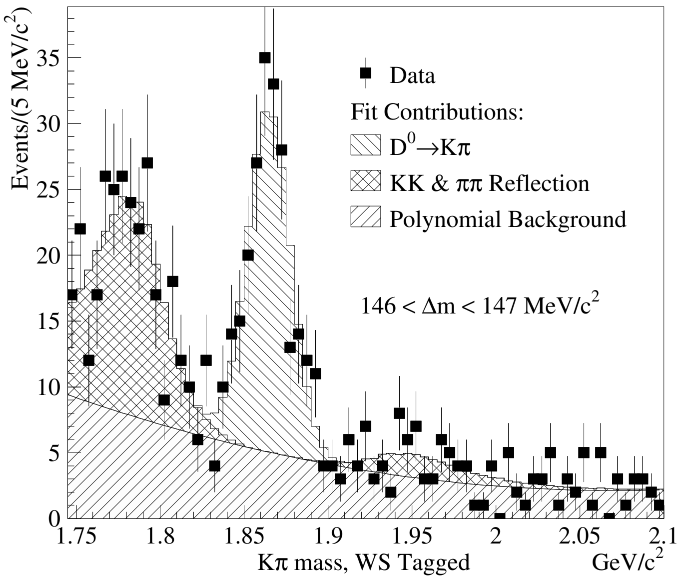

Figure 6.8: A typical fit of the $K\pi$ mass from the WS mass difference signal region, where the reflections are most prominent.

Appendix A.

6.2 The Mass Difference Fit

The mass difference fit is a MINUIT [45] based χ^2 minimization. The RS and WS mass difference plots are fit simultaneously with the RS signal shape used as a model for the WS signal. By inspection the RS signal region is chosen to run from 142 to 152 MeV/c^2.

The background is fit to a two parameter threshold function of the form

$$f(m) = \mathbf{A}[(m - m_\pi)^{1/2} + \mathbf{B}(m - m_\pi)^{3/2}]. \tag{6.2}$$

Separate fit parameters $\mathbf{A}$ and $\mathbf{B}$ are used in the fit to the RS and WS backgrounds.

At each iteration of the fit, the background contribution in each bin is calculated by integrating the background function across the bin. The RS background fit excludes the signal region. In the RS signal region, the interpolated background fit function is subtracted from the signal bin-by-bin. The remaining bin contents are scaled by a factor R_{WS} and added to the WS background function in the corresponding bins. For bin i, inside the signal region, the full χ^2 contribution is

$$\chi_i^2 = \frac{\left\{ Y_i^{\mathrm{WS}} - \left[\int_i f_{\mathrm{WS}}\, dm + R_{\mathrm{WS}} \left(Y_i^{\mathrm{RS}} - \int_i f_{\mathrm{RS}}\, dm \right) \right] \right\}^2}{\sigma^2_{Y_i^{WS}}} \tag{6.3}$$

where Y_i is the previously fit D^0 yield in bin i and σ_{Y_i} is its fitted error (there is no fit to the RS plot inside the signal region). Outside the signal region the full χ^2 contribution for bin i is

$$\chi_i^2 = \frac{\left(Y_i^{\mathrm{RS}} - \int_i f_{\mathrm{RS}}\, dm \right)^2}{\sigma^2_{Y_i^{\mathrm{RS}}}} + \frac{\left(Y_i^{\mathrm{WS}} - \int_i f_{\mathrm{WS}}\, dm \right)^2}{\sigma^2_{Y_i^{\mathrm{WS}}}}. \tag{6.4}$$

The scale factor R_{WS} is just the WS to RS branching ratio, meaning the branching ratio with errors comes directly out of the fit. The measured value of R_{WS} with statistical error is $(0.404 \pm 0.085)\%$ and the confidence level of this fit

Table 6.2: The mass difference fit parameters

Parameter	Fit Value
$\mathbf{A}_{\mathrm{RS}}$	1840 ± 79
$\mathbf{B}_{\mathrm{RS}}$	-7.4 ± 1.5
$\mathbf{A}_{\mathrm{WS}}$	1940 ± 63
$\mathbf{B}_{\mathrm{WS}}$	-7.4 ± 1.2
R_{WS}	$(4.04 \pm 0.85) \times 10^{-3}$

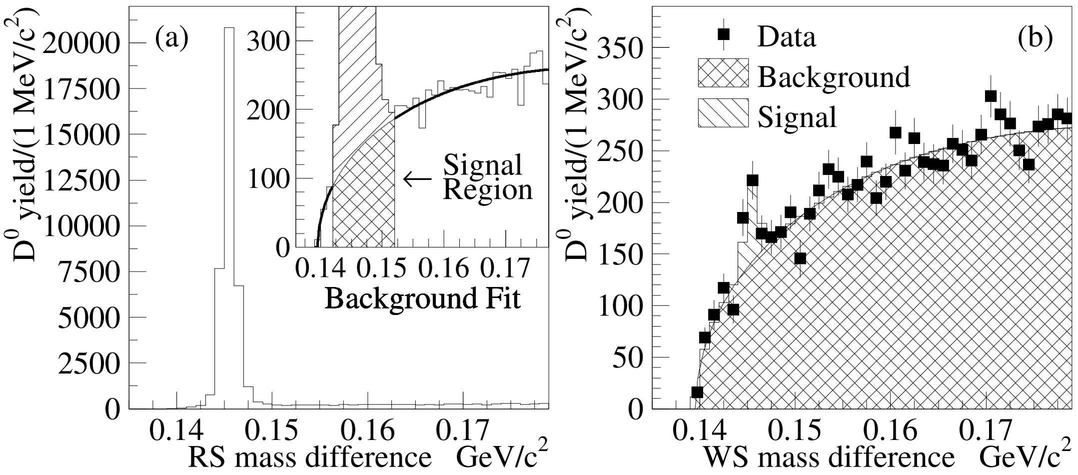

Figure 6.9: The **a)** right sign and **b)** wrong sign mass difference plots generated by fitting D^0 peak in 1 MeV/c^2 bins of $D^* - D$ mass difference. The inset to **(a)** is a close up of the RS background. The RS background fit is shown as a solid curve.

is 49.4%. Above the background we find 36 760±195 RS events which correspond to an effective WS yield of 149 ± 31. The fit is shown in Figure 6.9 and the fit parameters are given in Table 6.2

Using the RS mass difference signal as a WS signal model eliminates a potential source of systematic error due to an inadequate parameterization of the signal shape. A full discussion of systematic errors and cross checks is presented in the next section.

6.3 Systematic Error Studies

Recall from Section 1.4 that the measured branching ratio depends on the lifetime acceptance of the analysis if mixing is significant. Therefore, in evaluating the systematic error care must be taken to avoid studies that are correlated with lifetime, such as ℓ/σ_ℓ, which would indicate a systematic dependence on the cut value if large mixing is present. All other systematic studies are fair game.

6.3.1 Assumption of CP Conservation

In this analysis we have assumed that CP violation in the charm sector, and specifically in this decay mode, is small enough to be ignored. This assumption is tested by splitting the data into separate samples of D^0 and $\overline{D}^0$, and repeating the analysis on each sample. If a significant CP asymmetry is observed we should make a contribution to the systematic error due to the assumption of CP conservation. In Figure 6.10 is a comparison of the measured values of $R_{\rm WS}$ for each subsample to the measurement on the full data set and its statistical errors. The difference in $R_{\rm WS}$ observed between the D^0 and $\overline{D}^0$ data is small compared to the statistical error

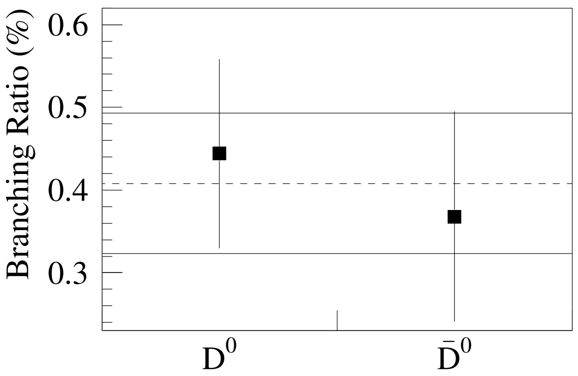

Figure 6.10: A comparison of $R_{\rm WS}$ for D^0 and $\overline{D}^0$ shows no indication of a CP violating asymmetry. The horizontal lines are the value and errors on $R_{\rm WS}$ for the combined sample.

on the full sample (especially since these are statistically independent samples) and is therefore insignificant.

6.3.2 Fit Method Systematics

Various methods of fitting the mass difference background are investigated:

- Instead of using the background parameterization of Equation (6.2), the function

$$f(m) = \mathbf{A}(m - m_\pi)^\alpha \times (1 + \mathbf{B}m) \tag{6.5}$$

  with new fit parameter α, is used.

- The RS and WS background fits are constrained to have the same shape, but not normalization, by constraining $\mathbf{B}_{\mathrm{RS}} = \mathbf{B}_{\mathrm{WS}}$.

- The mass difference bins centers are shifted by 0.25, 0.5 and 0.75 MeV/c^2.

- The mass difference bin width is adjusted from 1.0 MeV/c^2 to 0.8 MeV/c^2.

The results of these systematic tests are summarized in Table 6.3.2. The value of R_{WS} from all variants is consistent with the baseline measurement.

6.3.3 Monte Carlo Systematics

Since the WS and RS modes are kinematically identical any systematic effects due to spectrometer acceptance and analysis cuts should cancel. As a result there is

Table 6.3: Summary of the branching ratios from the fit systematic studies.

Variant	$R_{\rm WS}$ (%)	Fit C.L. (%)
Baseline conditions	0.404 ± 0.085	49.4
Alternate BG function	0.383 ± 0.086	53.8
$\mathbf{B}_{\rm RS} = \mathbf{B}_{\rm WS}$	0.407 ± 0.084	48.7
Bins shifted by 0.25 MeV/c^2	0.381 ± 0.087	23.1
Bins shifted by 0.50 MeV/c^2	0.374 ± 0.088	12.1
Bins shifted by 0.75 MeV/c^2	0.407 ± 0.086	37.7
Bin width 0.8 MeV/c^2	0.385 ± 0.085	14.5

no need for Monte Carlo efficiencies in computing $R_{\rm WS}$. Instead, the only direct use of the Monte Carlo in this analysis is in the $K\pi$ mass reflection fits. To check for systematic dependence of $R_{\rm WS}$ on the shape of the reflections the Monte Carlo reflection distributions are shifted by 2 MeV/c^2 (first high and then low), and the analysis is repeated. The values of $R_{\rm WS}$ obtained with the shifted reflections are $(0.397 \pm 0.082)\%$ for a positive shift and $(0.409 \pm 0.085)\%$ for a negative shift. These values are very consistent with the baseline measurement and demonstrate that subtle problems with the way Monte Carlo models the data will not significantly affect the measurement.

6.3.4 Cut Variants

Ignoring cuts like ℓ/σ_ℓ and primary isolation, that are strongly correlated with lifetime, only the asymmetry cut and Čerenkov cuts have a sufficient impact on the data to warrant systematic error study.

Momentum Dependant Asymmetry Cut

The primary concern with the asymmetry cut is that it is constructed to be momentum dependent. This is tested by repeating the analysis with the momentum dependent cut replaced by a cut of $\mathcal{A} < 70\%$. With this cut we measure $R_{\mathrm{WS}} = (0.458 \pm 0.086)\%$. This value is larger than expected but as we will see in Section 6.3.5 the contribution to the systematic error from the asymmetry cut is still relatively small.

Čerenkov Cuts

The general Čerenkov cuts are set about as low as the skim selection allows. Although the analysis discussed in Section 6.1.4 is intended to deal with misidentified background (among other things) it is conceivable that the low Čerenkov cut setting may allow problematic backgrounds that would cause a systematic shift in the measurement. To investigate this the analysis is repeated using the cut levels $\Delta W_{K,\pi} > 2$ and $\Delta W_{\pi,K} > 2$. A value of $R_{\mathrm{WS}} = (0.404 \pm 0.105)\%$ is obtained, which indicates no significant problem. It is interesting to note the 24% increase in the error, which indicates the scale of precision lost if hard particle identification cuts are used.

Double Mis-ID Cut

In Section 6.1.1 we discussed the double mis-ID cut which is designed to remove the correlated background from $D^0 \to K^-\pi^+$ decays where the K is misidentified as a π and the π is misidentified as a K. This double mis-ID cut was shown to be effective at removing this background in the Monte Carlo. To avoid relying on the Monte Carlo the effectiveness of the cut is also tested by measuring $R_{\rm WS}$ as the double mis-ID cut variable, $\Delta W_{K,\pi} + \Delta W_{\pi,K}$ is varied in integer steps from zero to ten. In Figure 6.11 these measurements of $R_{\rm WS}$ are plotted versus the cut point in the sum $\Delta W_{K,\pi} + \Delta W_{\pi,K}$. The value of $R_{\rm WS}$ is stable above a cut of four, which is well below the value of eight used in the analysis. If the double mis-ID cut was not removing the target background effectively we would expect to see the value of $R_{\rm WS}$ continue to decrease as the cut is tightened.

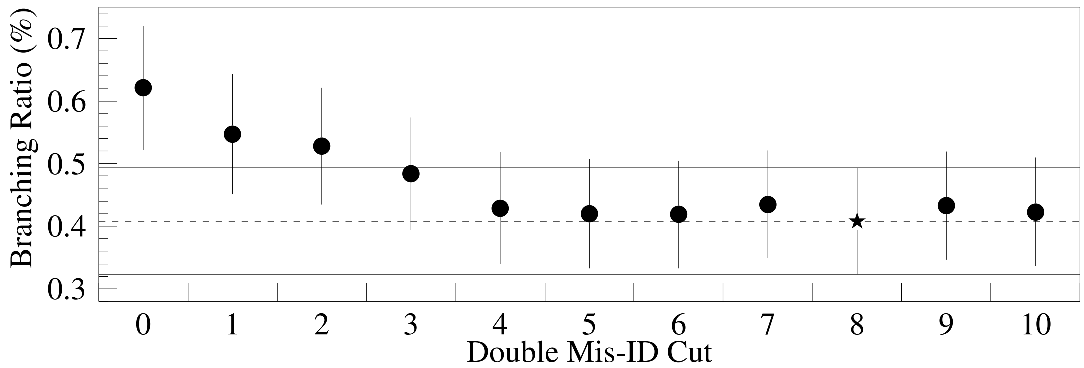

Figure 6.11: $R_{\rm WS}$ versus the strength of the double mis-ID cut. Note that the branching ratio is constant above a cut of four, well below the value of eight (indicated by a star) used in the analysis.

The double mis-ID cut is also tested for systematic effects associated with the particle hypothesis switched mass window range. Two additional mass windows are studied: one at $\pm 8\,\sigma$ and the second covering the whole plot range.

$$\pm 8\,\sigma \text{ window:} \quad R_{\mathrm{WS}} = (0.408 \pm 0.086)\%$$

$$\text{Whole range:} \quad R_{\mathrm{WS}} = (0.433 \pm 0.087)\%$$

These studies do not indicate any significant systematic problems.

6.3.5 Estimating the Systematic Error

To estimate the systematic error, measurements of R_{WS} are made with 140 different combinations of fit conditions and cut variations. Each of the seven different fit conditions listed in Table 6.3.2 are used. Measurements are made with all possible combinations of the baseline conditions, the alternate background function, and the $\mathbf{B}_{\mathrm{RS}} = \mathbf{B}_{\mathrm{WS}}$ condition for each of the 5 different binning conditions. Then each of these 20 combinations are used with each of the two Monte Carlo mass shifts, the two alternate Čerenkov cut sets, and the alternate asymmetry cut for a total of 140 measurements. Four of the 140 variant combinations failed to converge properly and are not considered. Figure 6.12 shows the different variant combinations and their spread. To estimate the systematic error, each measurement is assumed to be equally likely. Then the statistical variance of the measurements is taken to be the systematic error on R_{WS}. A systematic error of 0.025% is obtained.

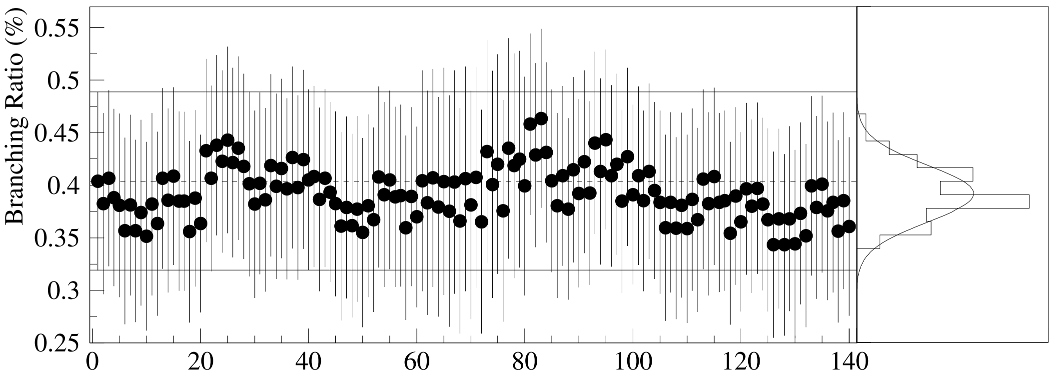

Figure 6.12: The spread of R_{WS} measurements. The systematic error is taken to be the statistical variance of the points in the distribution ($\sigma_{\mathrm{sys}} = 0.025\%$). The horizontal lines are the value of R_{WS} and its error for the baseline measurement.

Table 6.3.5 gives a breakdown of the variant statistical spread and average R_{WS} of the 20 fit variants for each cut variant.

Then the value of the branching ratio, R_{WS} with full errors is

$$R_{\mathrm{WS}} = (0.404 \pm 0.085 \pm 0.025)\%.$$

In the limit of no mixing the observed branching ratio R_{WS} is equal to the DCS branching ratio R_{DCS}.

Table 6.4: A breakdown of the fit variant spreads and average R_{WS} by study.

Cut Variant	Average R_{WS} (%)	$\sigma_{R_{\mathrm{WS}}}$ (%)
Baseline	0.380 ± 0.086	0.017
MC Shift +2 MeV/c^2	0.373 ± 0.086	0.019
MC Shift -2 MeV/c^2	0.383 ± 0.086	0.018
Asymmetry<70%	0.415 ± 0.087	0.025
Tight Čerenkov	0.399 ± 0.106	0.021
Wide Double Mis-ID	0.383 ± 0.087	0.017
Untargeted Double Mis-ID	0.413 ± 0.087	0.017
All 140 Variants	0.392 ± 0.086	0.025

Chapter 7

Effects of Mixing

As discussed in Section 1.4, if there is significant $D^0-\overline{D}^0$ mixing the value of the measured branching ratio R_{WS} will depend on the lifetime acceptance of the analysis. In this chapter we derive a relationship between R_{WS} and R_{DCS} for arbitrary values of x' and y'. Then we use this relationship to estimate the value of y'.

7.1 R_{DCS} in the Presence of Mixing

The time dependent rate for WS decays relative to the CF branching fraction is given by Equation (1.26)

$$R(t) = \left(R_{\mathrm{DCS}} + \sqrt{R_{\mathrm{DCS}}}\; y' t + \frac{x'^2+y'^2}{4} t^2\right) e^{-t}. \tag{1.26}$$

Using a large Monte Carlo sample (10 times the data) of $D^0 \to K^-\pi^+$ decays, generated with a pure exponential lifetime of 413 fs [8], we can calculate the expected number of WS events by reweighting each accepted Monte Carlo event with a weight given by

$$W(t_i, x', y', R_{\rm DCS}) = \frac{N_{\rm RS}}{N_{\rm MC}} \left(R_{\rm DCS} + \sqrt{R_{\rm DCS}}\ y' t_i + \frac{x'^2 + y'^2}{4} t_i^2 \right), \tag{7.1}$$

where t_i is the generated proper time for event i, and $N_{\rm RS}$ and $N_{\rm MC}$ are the number of accepted RS events in the data and Monte Carlo. The expected number of WS events ($N_{\rm WS}$) is determined by summing the weights of Equation (7.1) over all accepted Monte Carlo events:

$$\begin{aligned} N_{\rm WS} &= \sum_i^{\rm accepted} W(t_i, x', y', R_{\rm DCS}) \\ &= \frac{N_{\rm RS}}{N_{\rm MC}} \left(\sum_i^{\rm accepted} R_{\rm DCS} + \sqrt{R_{\rm DCS}}\ y' \sum_i^{\rm accepted} t_i + \frac{x'^2 + y'^2}{4} \sum_i^{\rm accepted} t_i^2 \right) \\ &= N_{\rm RS} \left(R_{\rm DCS} + \sqrt{R_{\rm DCS}}\ y' \langle t \rangle + \frac{x'^2 + y'^2}{4} \langle t^2 \rangle \right) \end{aligned} \tag{7.2}$$

where the averages $\langle t \rangle$ and $\langle t^2 \rangle$ are measured from the generated lifetime of all Monte Carlo events accepted in the analysis. The generated lifetime is used to compensate for a known bias on the reconstructed proper time from daughter tracks of the associated charm particle which tend to pull the production vertex downstream, thus producing a systematically shorter lifetime.

Dividing by $N_{\rm RS}$ we get

$$R_{\rm WS} = \frac{N_{\rm WS}}{N_{\rm RS}} = R_{\rm DCS} + \sqrt{R_{\rm DCS}}\ y' \langle t \rangle + \frac{x'^2 + y'^2}{4} \langle t^2 \rangle. \tag{7.3}$$

To obtain an expression for $R_{\rm DCS}$ in terms of x', y' and $R_{\rm WS}$, we solve Equation (7.3) for $\sqrt{R_{\rm DCS}}$ and square both sides:

$$\begin{aligned} R_{\rm DCS} = \; & \frac{y'^2\langle t\rangle^2}{2} - \frac{x'^2+y'^2}{4}\langle t^2\rangle + R_{\rm WS} \pm \\ & \frac{y'\langle t\rangle}{2}\sqrt{y'^2\langle t\rangle^2 - (x'^2+y'^2)\langle t^2\rangle + 4R_{\rm WS}}. \end{aligned} \tag{7.4}$$

The solution with the positive square root term is rejected because in the region of interest (y' near zero) it corresponds to a complex solution when Equation (7.3) is solved for $R_{\rm DCS}$.

From the Monte Carlo set we measure

$$\langle t\rangle = (1.578\pm 0.002)\tau_{D^0}$$

and

$$\langle t^2\rangle = (3.61\pm 0.01)\tau_{D^0}^2.$$

To determine their systematic error we compare the Monte Carlo reconstructed averages to the averages in the RS data. There is nothing special about the Monte Carlo events in deriving Equation (7.3). In the absence of the vertex pull, which necessitates the use of the unbiased generated lifetime, the averages could be derived from the RS data. All that is required is a large sample of $D^0 \to K^-\pi^+$ events with an underlying exponential lifetime distribution, which is subjected to the spectrometer's acceptance and analysis cuts. Table 7.1 shows the averages obtained with Monte Carlo events from the generated and reconstructed lifetimes as

Table 7.1: The average lifetime and average lifetime squared measured with different lifetime sources. The lifetime is in units of $\tau_{D^0} = 413\ fs$.

Source	$\langle t \rangle$	$\langle t^2 \rangle$
MC Generated	1.578±0.002	3.61±0.01
MC Reconstructed	1.562±0.002	3.56±0.01
Data	1.569±0.006	3.58±0.03
MC Reconstructed (generated $\tau_{D^0} = 409\ fs$)	1.570±0.007	3.55±0.04

well as from data. The systematic shift in reconstructed lifetime is apparent in the difference between the Monte Carlo generated and reconstructed averages. With the numbers in Table 7.1 we estimate the systematic errors to be $\sigma_{\langle t \rangle} = 0.007$ and $\sigma_{\langle t^2 \rangle} = 0.03$. These systematic errors are consistent with the error expected if the PDG [8] D^0 lifetime was high by one standard deviation. To illustrate this, the fourth entry in Table 7.1 gives the Monte Carlo reconstructed averages for events generated with $\tau_{D^0} = 409\ fs$ (about $1\,\sigma$ below the PDG average). These averages are more consistent with the data averages.

Figure 7.1 shows the dependence of R_{DCS} on the mixing parameters. In Figure 7.1a, R_{DCS} is plotted as a function of y' with x' fixed at zero, and in Figure 7.1b, R_{DCS} is plotted as a function of x' with y' at zero. The cross hashed bands contain all points within $1\,\sigma$ combined statistical and systematic error. The band is determined by inserting $R_{\text{WS}} + \sigma_{\text{WS}}$ and $R_{\text{WS}} - \sigma_{\text{WS}}$ in Equation (7.4). The lifetime average errors are added linearly with the appropriate functional dependence on y', but the additional error added by this step widens the error band

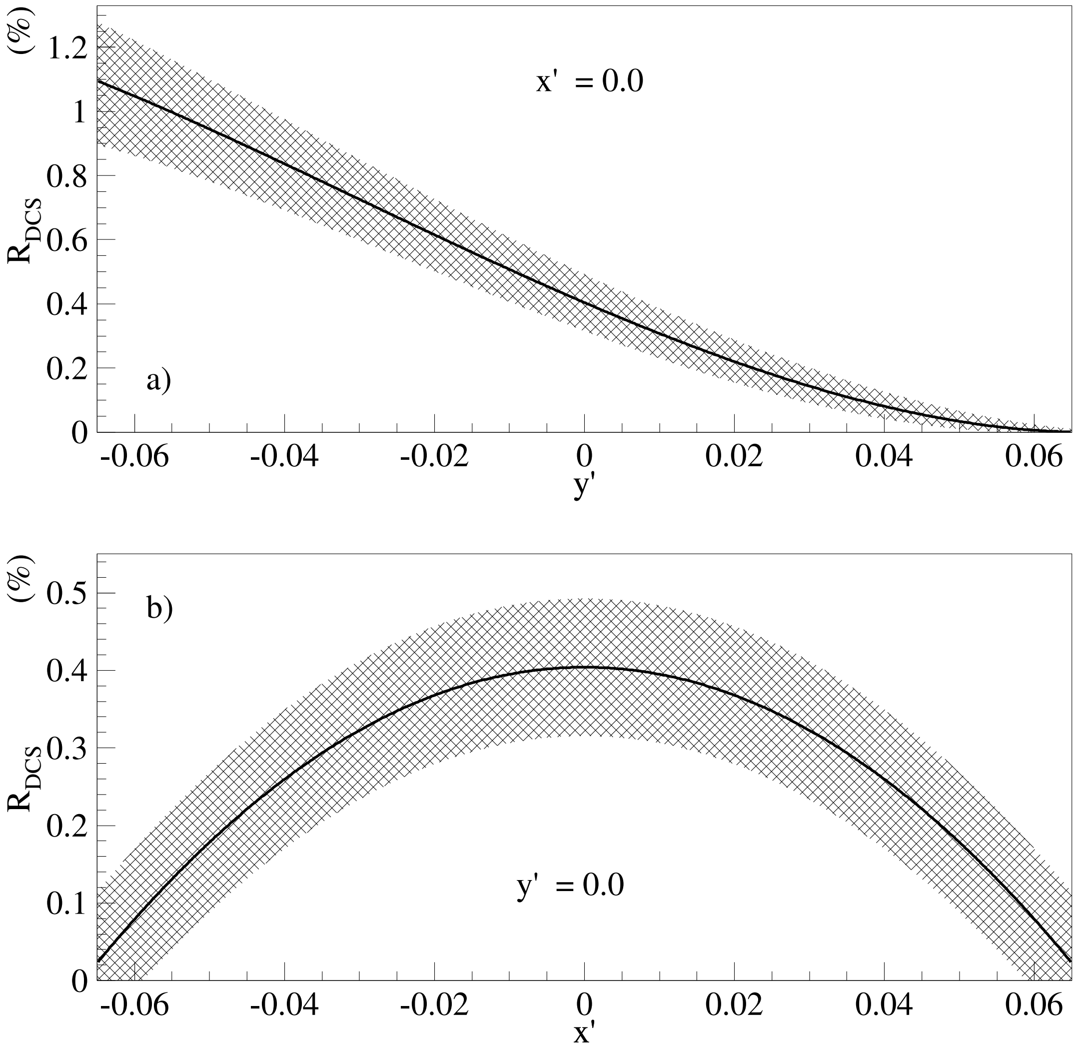

Figure 7.1: R_{DCS} plotted as a function of **a)** y' with $x' = 0$ and **b)** x' with $y' = 0$.

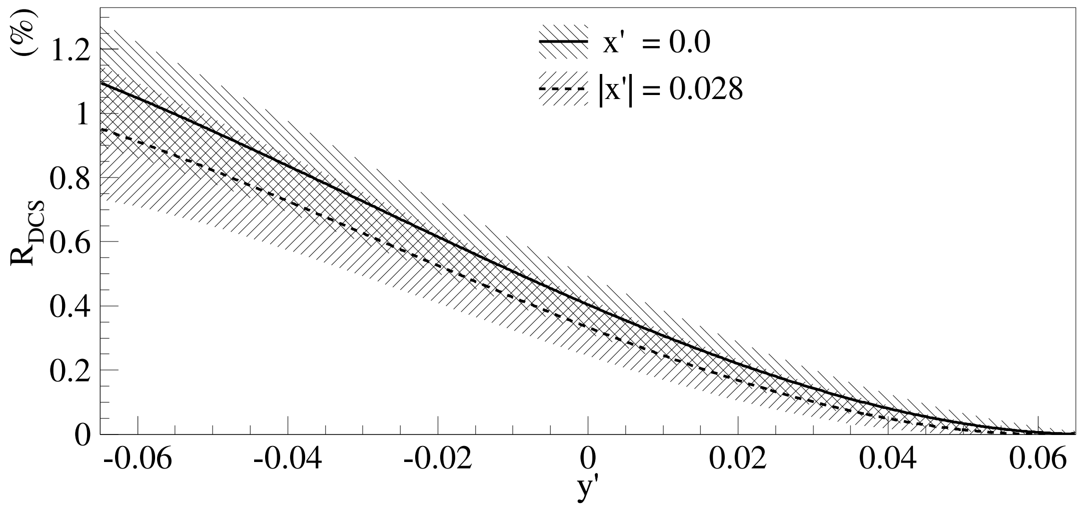

Figure 7.2: $R_{\rm DCS}$ plotted as a function of y'. The bands are given for $x' = 0.0$ and $|x'| = 0.028$, which cover the 95% CL from CLEO II.V.

imperceptibly. Observe that $R_{\rm DCS}$ is a symmetric function of x' which is expected since the function only has x'^2 dependence. Also, $R_{\rm DCS}$ is only marginally sensitive to the value of x' within the 95% CL range of CLEO II.V's ($-0.028 < x' < 0.028$). In Figure 7.2, $R_{\rm DCS}$ is plotted against y' for $x' = 0$ and $|x'| = 0.028$. Clearly, this measurement has very little sensitivity to x'.

7.2 Measuring y'

Figure 7.1a suggests a method to measure y'. If the data is split into two or more lifetime bins and $R_{\rm WS}$, $\langle t \rangle$ and $\langle t^2 \rangle$ are determined in each bin, then the resulting bands can be overlayed. The point at which they intersect is the preferred value

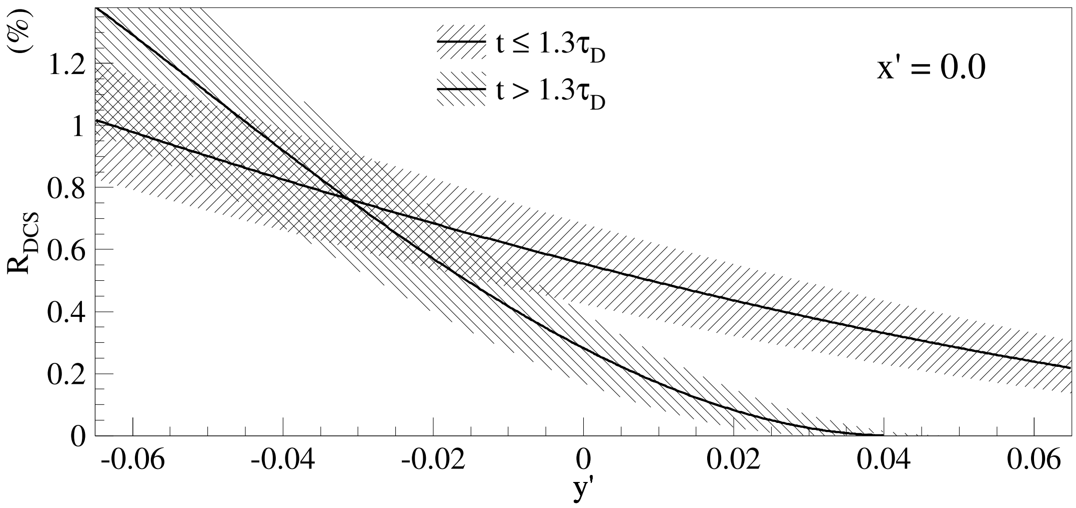

Figure 7.3: The intersection of R_{DCS} curves for high and low lifetime bins split at $1.3\tau_{D^0}$.

of y' and R_{DCS}. Unfortunately, the complexity of the fit procedure used to determine R_{WS} makes dividing the data into more than two bins virtually impossible. Figure 7.3 shows the intersection of the curves for events with t greater than and less than $1.3\,\tau_{D^0}$. The value of $1.3\,\tau_{D^0}$ is chosen because it optimizes the errors on R_{WS} in both splits, and it very nearly gives an equal split of the WS signal events.

To determine the confidence level limits on y' and R_{DCS}, a grid search is used in y' and R_{DCS} space to find points corresponding to the desired confidence level boundary. The confidence level of an individual point is calculated by first computing the χ^2 with respect to the the high and low t curves:

$$\chi^2(y', R_{\text{DCS}}) = \left(\frac{R_{\text{WS}\,h} - f_h(y', R_{\text{DCS}})}{\sigma_{R_{\text{WS}\,h}}}\right)^2 + \left(\frac{R_{\text{WS}\,l} - f_l(y', R_{\text{DCS}})}{\sigma_{R_{\text{WS}\,l}}}\right)^2 \tag{7.5}$$

where $R_{\text{WS}\,h(l)}$ is the branching ratio measured in the high (low) t data;

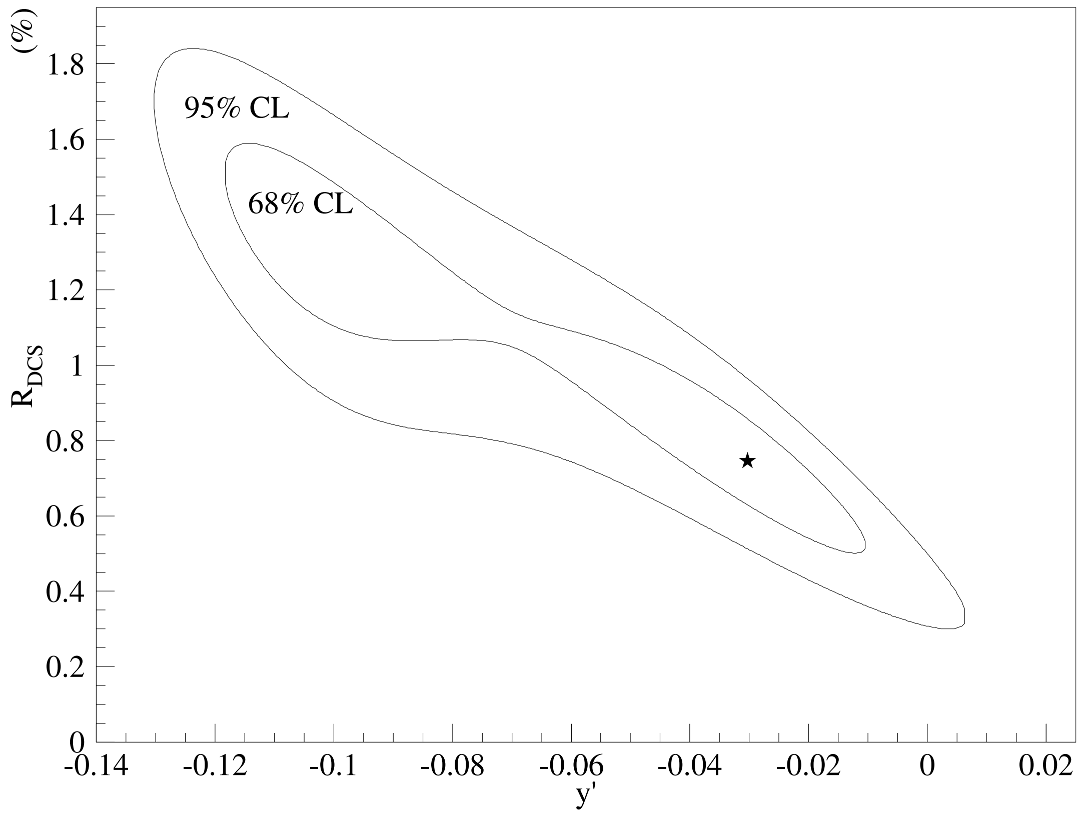

Figure 7.4: The 95% and 68% (or $1\,\sigma$) confidence level regions for y' and R_{DCS} from a lifetime split at $1.3\,\tau_{D^0}$.

$f_{h(l)}(y', R_{\text{DCS}})$ is the value of the function in Equation (7.3) evaluated at the point (y', R_{DCS}) using the high (low) t averages; and $\sigma_{R_{\text{WS}\,h(l)}}$ is the error on $R_{\text{WS}\,h(l)}$. The confidence level is the integral from the value of $\chi^2(y', R_{\text{WS}})$ to infinity of the probability density function for a χ^2 distribution with one degree of freedom [46]. Figure 7.4 shows the boundary of the 68% (or 1σ) and 95% confidence level regions. By integrating over the other variable we measure the 95% CL ranges

$$-0.124 < y' < -0.006$$

and

$$0.43\% < R_{\text{DCS}} < 1.73\%.$$

Although a full analysis of the systematic errors has not yet been done, several cross checks have been made. First, the lifetime split point is varied from 1.1 to $1.4\tau_{D^0}$. Outside this range diminishing statistics make the fit unreliable. The 95% CL boundaries and crossing points for the splits from this study are shown in Figure 7.5. The crossing points show variations consistent with the statistical

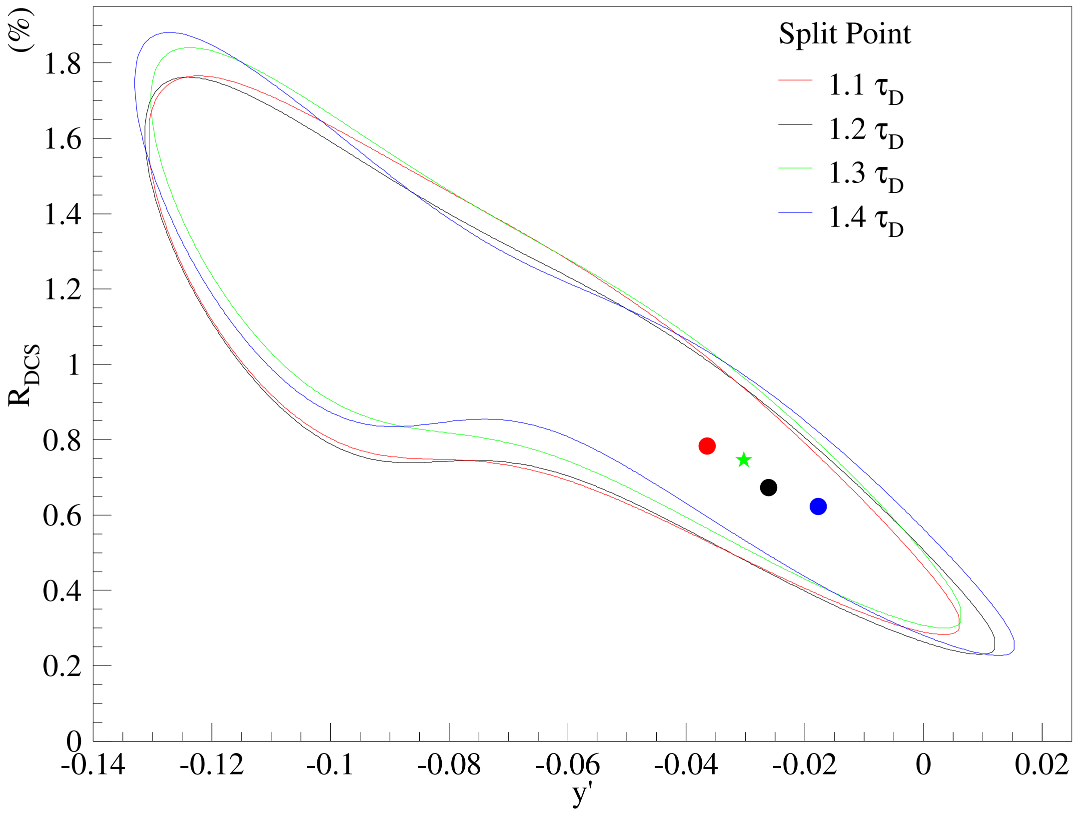

Figure 7.5: The confidence level regions and crossing points for y' and R_{DCS} from several splits in the range of 1.1 to 1.4 τ_{D^0}.

fluctuations in the R_{WS} measured values and no lifetime split dependent trend is seen. This result generally supports the restrictive upper limit on y', indicating that it is robust over several split values and is not due to a random fluctuation.

We also tested the sensitivity of the boundary to x', by setting $x' = 0.028$ (the CLEO II.V 95% CL limit) in Equation (7.3). The resulting 95% CL region is plotted in Figure (7.6). In this case the y' limit is even more restrictive than with $x' = 0$. It is clear from this result that the preferred negative value of y' is not the

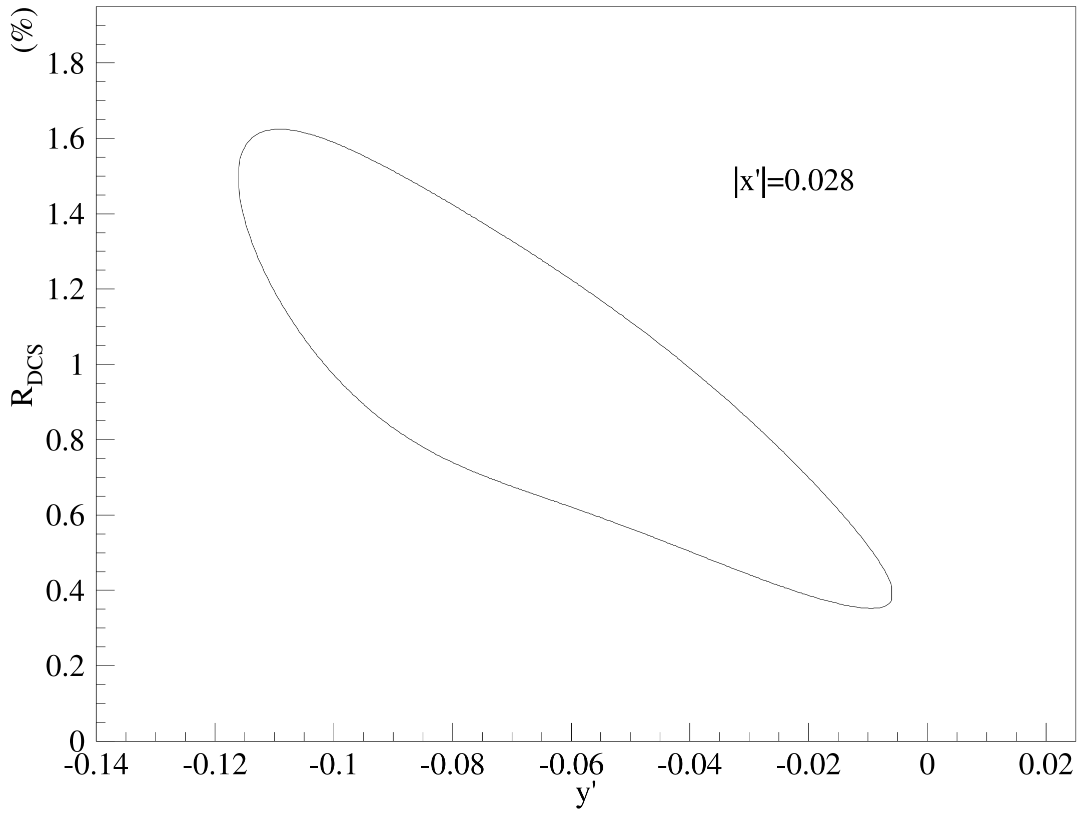

Figure 7.6: The confidence level region for y' and R_{DCS} with $|x'| = 0.028$ and the lifetime split at $1.3\,\tau_{D^0}$.

result of an interaction with a non-zero x'.

Chapter 8

Conclusions

We observe a signal in the decay channel $D^0 \to K^+\pi^-$ and measure its branching ratio relative to $D^0 \to K^-\pi^+$ to be $(0.404 \pm 0.085 \pm 0.025)\%$. If charm sector mixing is significant, the doubly Cabibbo suppressed component of the branching ratio can be determined for an arbitrary set of the mixing parameters x' and y' using the measured ratio R_{WS} and Equation 7.4.

8.1 Comparison to Existing Measurements

In Figure 8.1, the mixing measurements of CLEO II.V [7] and FOCUS [33] are plotted with the $y'R_{\mathrm{DCS}}$ band from Section 7.1. Recall from Section 1.5 that the CLEO result is from a direct measurement of R_{DCS}, x' and y', and the FOCUS band comes from a direct measurement of $\Delta\Gamma$. The FOCUS result is for y and can

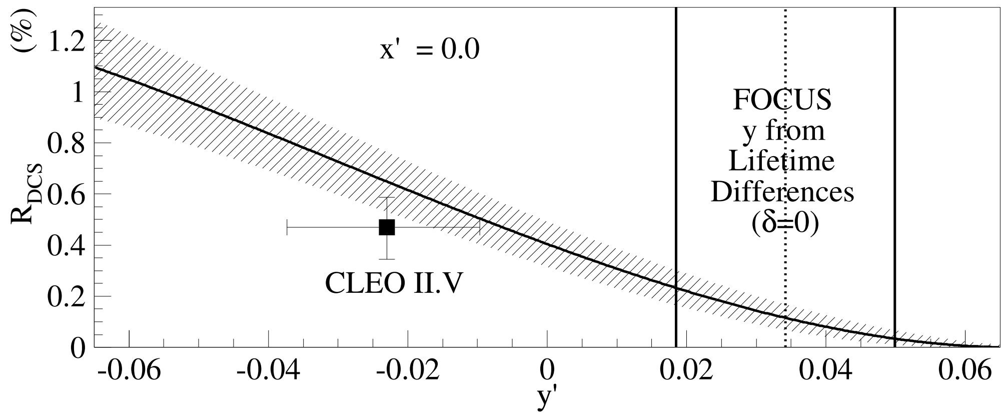

Figure 8.1: $R_{\rm DCS}$ contour compared to the CLEO II.V and FOCUS mixing results. A direct comparison to the FOCUS result requires $\delta = 0$.

only be directly compared to the other results in the limit as the strong phase δ goes to zero. From this comparison it is only possible to say that both results are consistent with the mixing DCS band determined in this thesis.

The existing direct limits on y' (including the semileptonic limit of E791 [32]) are compared to our 95% CL region for y' and $R_{\rm DCS}$ in Figure 8.2. The CLEO value of y' is in good agreement with the value found in this analysis. Both measurements suggest a negative y' with a value on order of a few percent. Together these measurements strongly disfavor a positive y' at the percent level. Combined with the FOCUS lifetime difference measurement (which favors positive y), these three results suggest two possible mixing scenarios: 1) y is positive and has a value of a few percent and there is a large strong phase δ, or 2) y is less than a percent and the recent results on y and y' which differ from zero by $\sim 2\,\sigma$ are statistical fluctuations. If the first scenario is correct then we have a

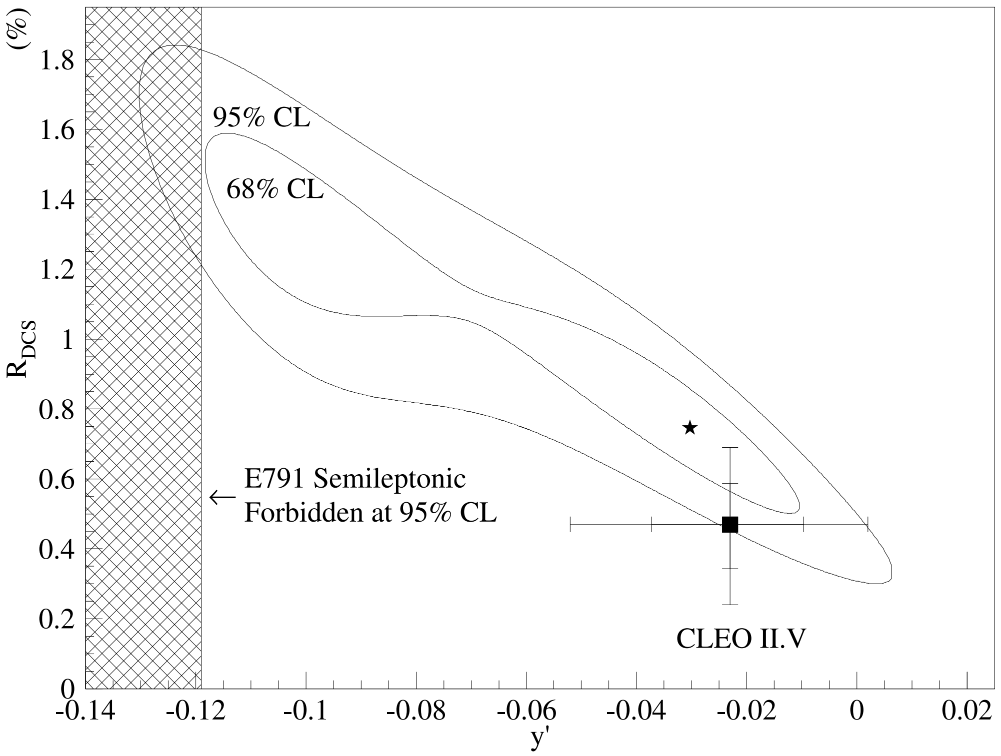

Figure 8.2: A comparison of the R_{DCS} and y' CL regions to the CLEO II.V and E791 results.

very interesting situation since neither large y-like mixing nor large strong phase has been anticipated by theory. The second scenario is much more mundane, as it exactly the situation that is expected in the SM. More studies of $D^0 - \overline{D}^0$ mixing are required to determine which scenario is correct.

8.2 Outlook for Mixing in FOCUS

There are several studies that can be undertaken with the FOCUS data set to further study $D^0 - \overline{D}^0$ mixing.

An analysis of semileptonic wrong sign decays is currently in progress. The expected 90% CL sensitivity in R_{mix}, using both the electron and the muon samples, is about 1.3×10^{-3}. This corresponds to a y or y' sensitivity of about 5%.

Direct measurements of $\Delta\Gamma$ can be made with other CP eigenstate modes. In particular, measurements of the lifetime difference for CP odd modes would be extremely interesting. See Reference [47] for an expanded discussion of CP eigenstate modes for lifetime difference studies.

Finally, more can be done with mixing measurements using wrong sign hadronic modes and exploiting the interference term. It is possible to make a fit to the WS lifetime distribution as was done by CLEO. Unfortunately, the method developed here to deal with correlated backgrounds will not isolate the $K\pi$ contribution from the reflection contributions in the lifetime distribution. As a result, hard particle identification cuts would be required leading to a loss of at least 35% of the WS signal. Also the signal to noise ratio of the WS $D^* - D$ mass signal is only 0.2, with the majority of the background coming from untagged CF decays. This background will cause a significant dilution of the WS decays in the lifetime distribution. If new ways can be found to clean up the WS distribution without sacrificing too much signal then a lifetime study with the FOCUS data could markedly improve on the CLEO II.V limits.

Appendix A

Fits to $K\pi$ Subsets

The following plots are the 80 $K\pi$ mass fits described in Section 6.1.4. The data are the solid circles with error bars, the K^+K^- and $\pi^+\pi^-$ reflection fit contributions are shown in the darkest shade (blue), the D^0 signal fit contribution is shown in the medium shade (green) and the polynomial background fit contribution is shown in the lightest shade (yellow).

A.1 Wrong Sign Tagged Fits

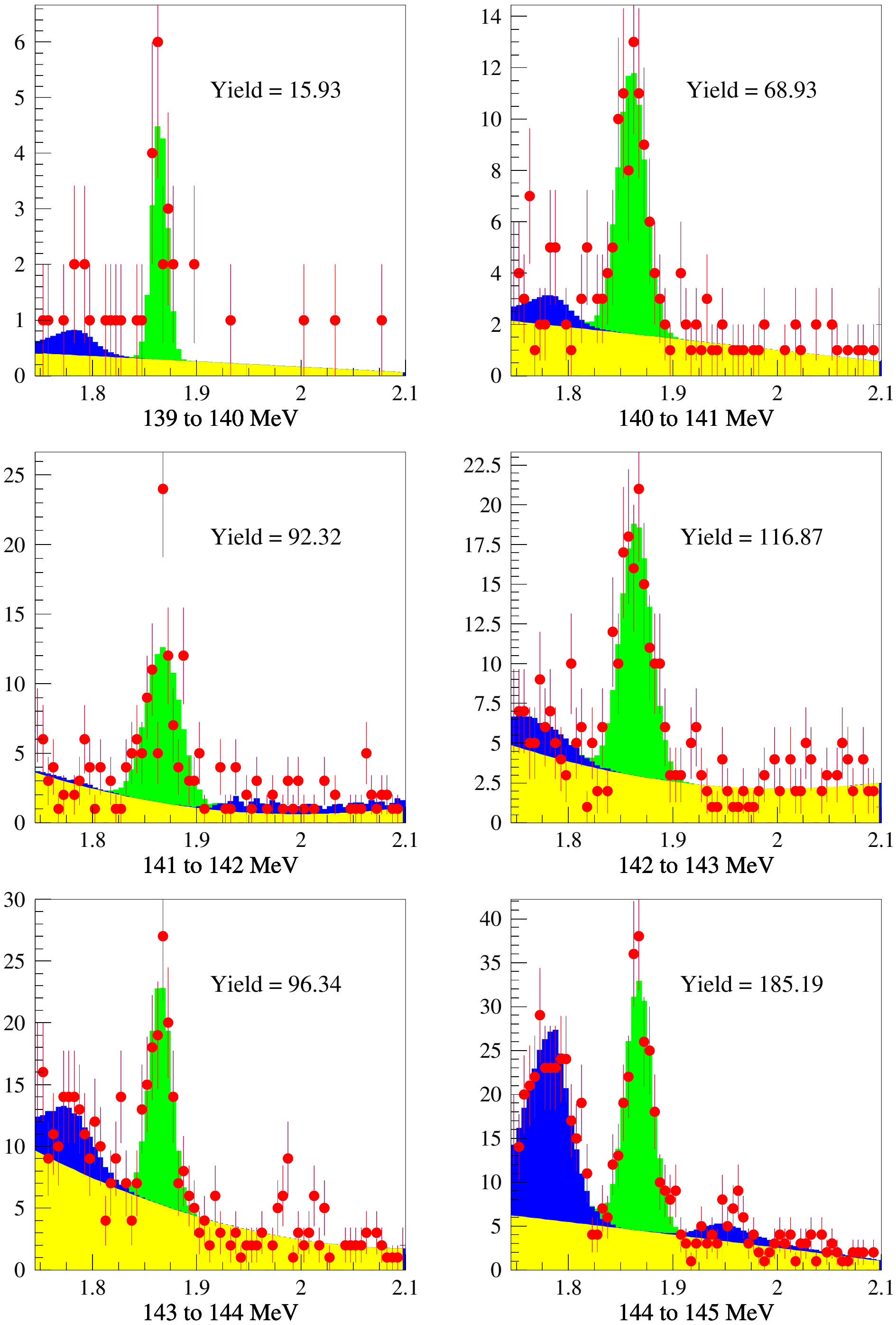

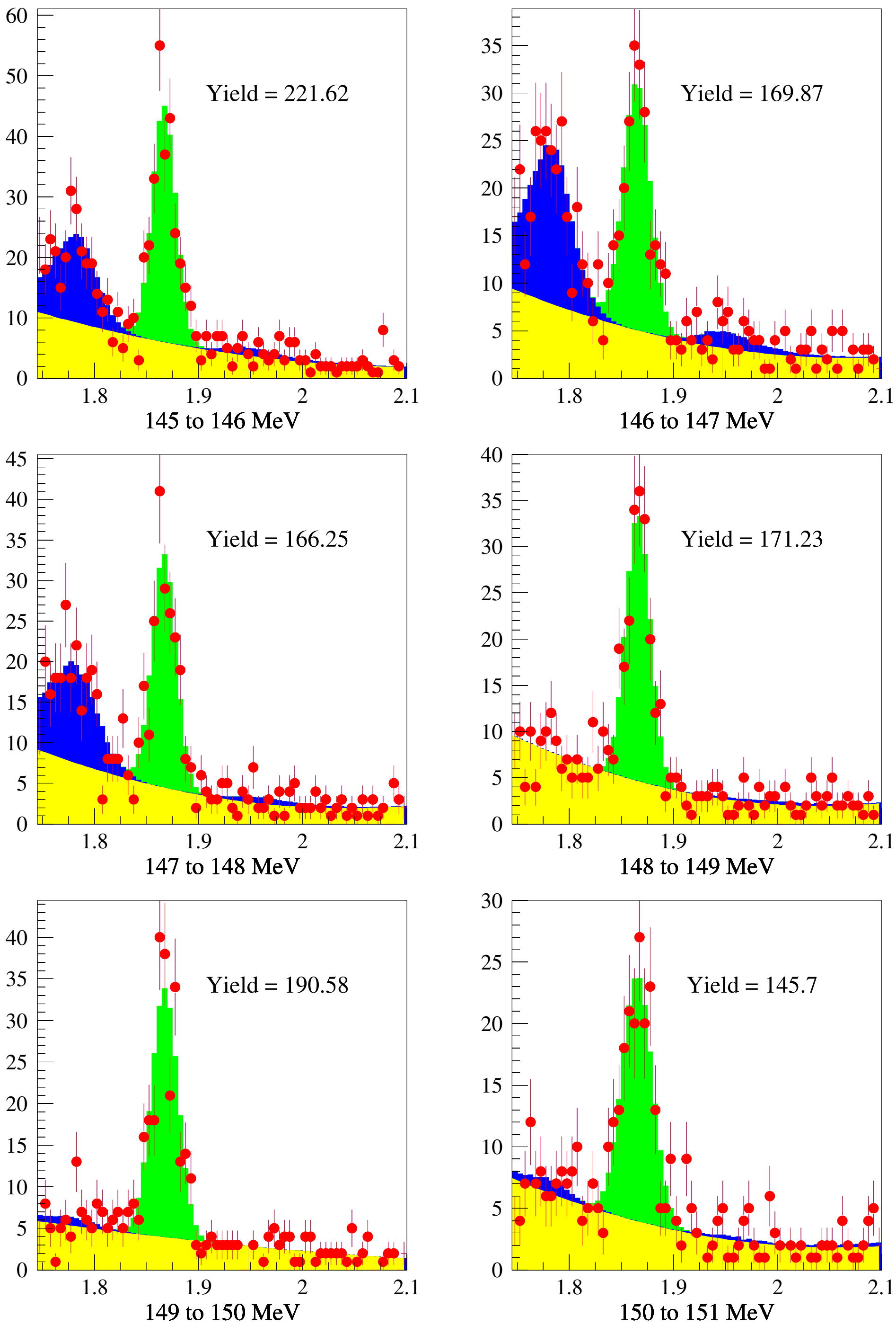
Yield = 221.62
145 to 146 MeV
Yield = 169.87
146 to 147 MeV
Yield = 166.25
147 to 148 MeV
Yield = 171.23
148 to 149 MeV
Yield = 190.58
149 to 150 MeV
Yield = 145.7
150 to 151 MeV

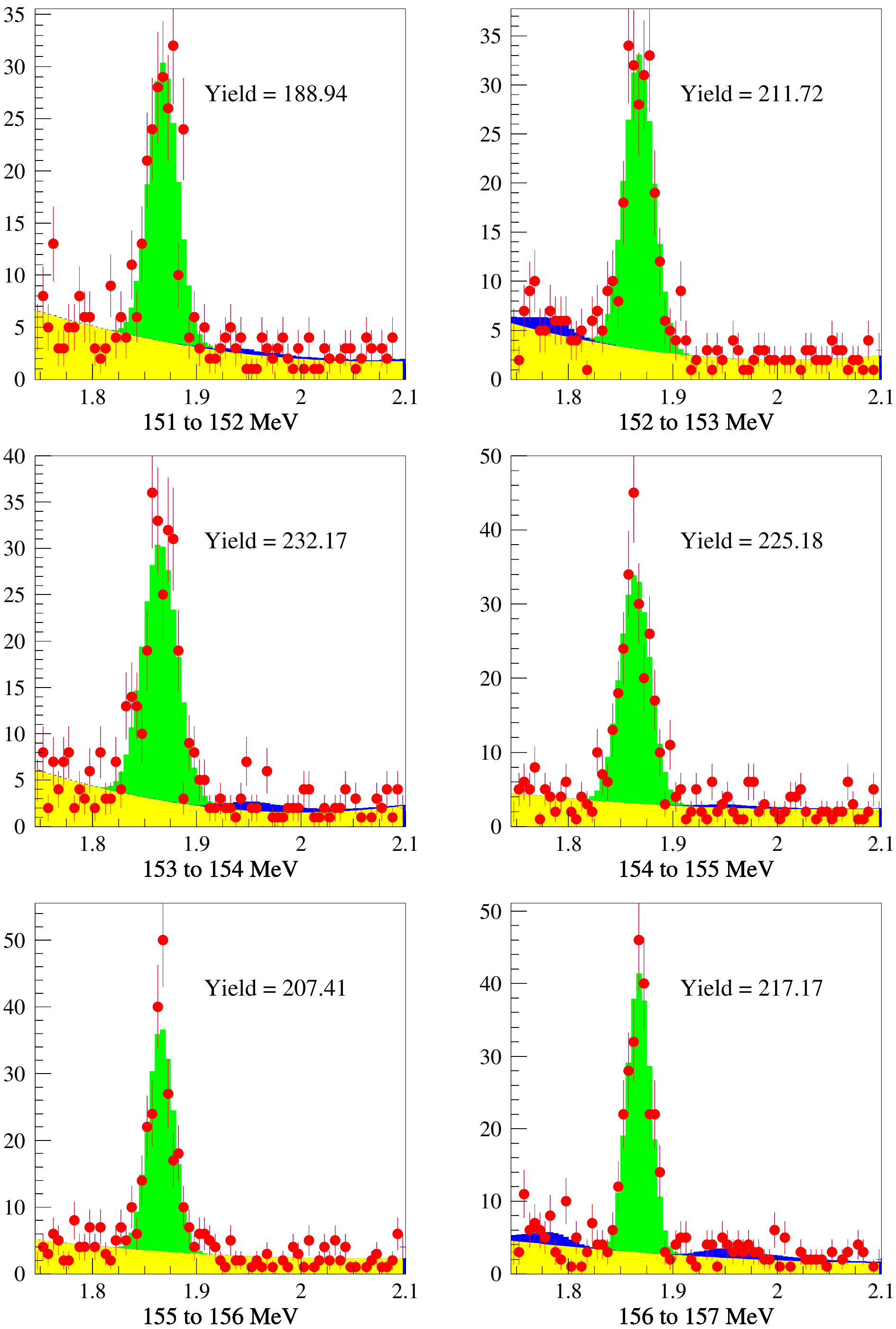
Yield = 188.94
151 to 152 MeV
Yield = 211.72
152 to 153 MeV
Yield = 232.17
153 to 154 MeV
Yield = 225.18
154 to 155 MeV
Yield = 207.41
155 to 156 MeV
Yield = 217.17
156 to 157 MeV

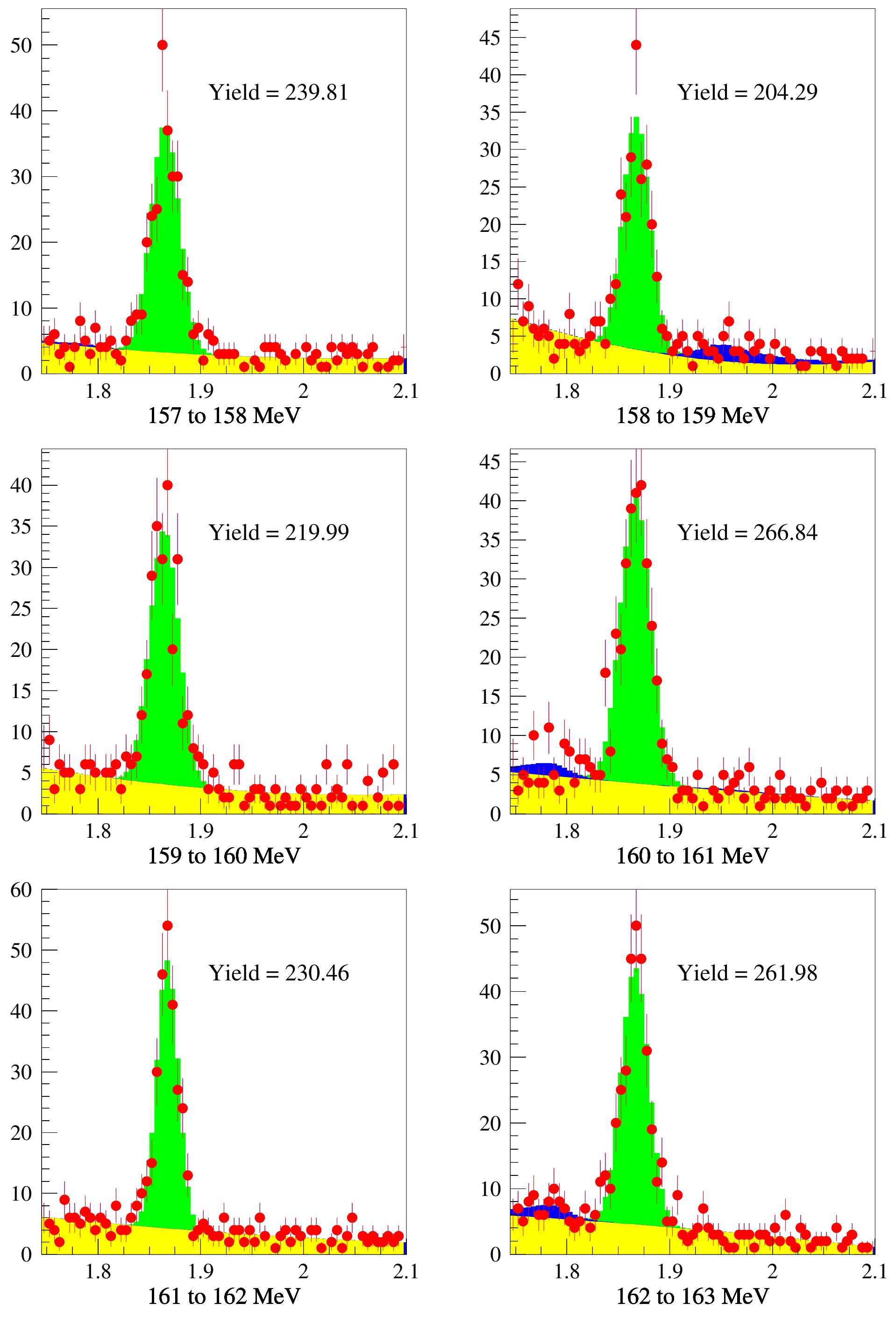
Yield = 239.81
157 to 158 MeV
Yield = 204.29
158 to 159 MeV
Yield = 219.99
159 to 160 MeV
Yield = 266.84
160 to 161 MeV
Yield = 230.46
161 to 162 MeV
Yield = 261.98
162 to 163 MeV

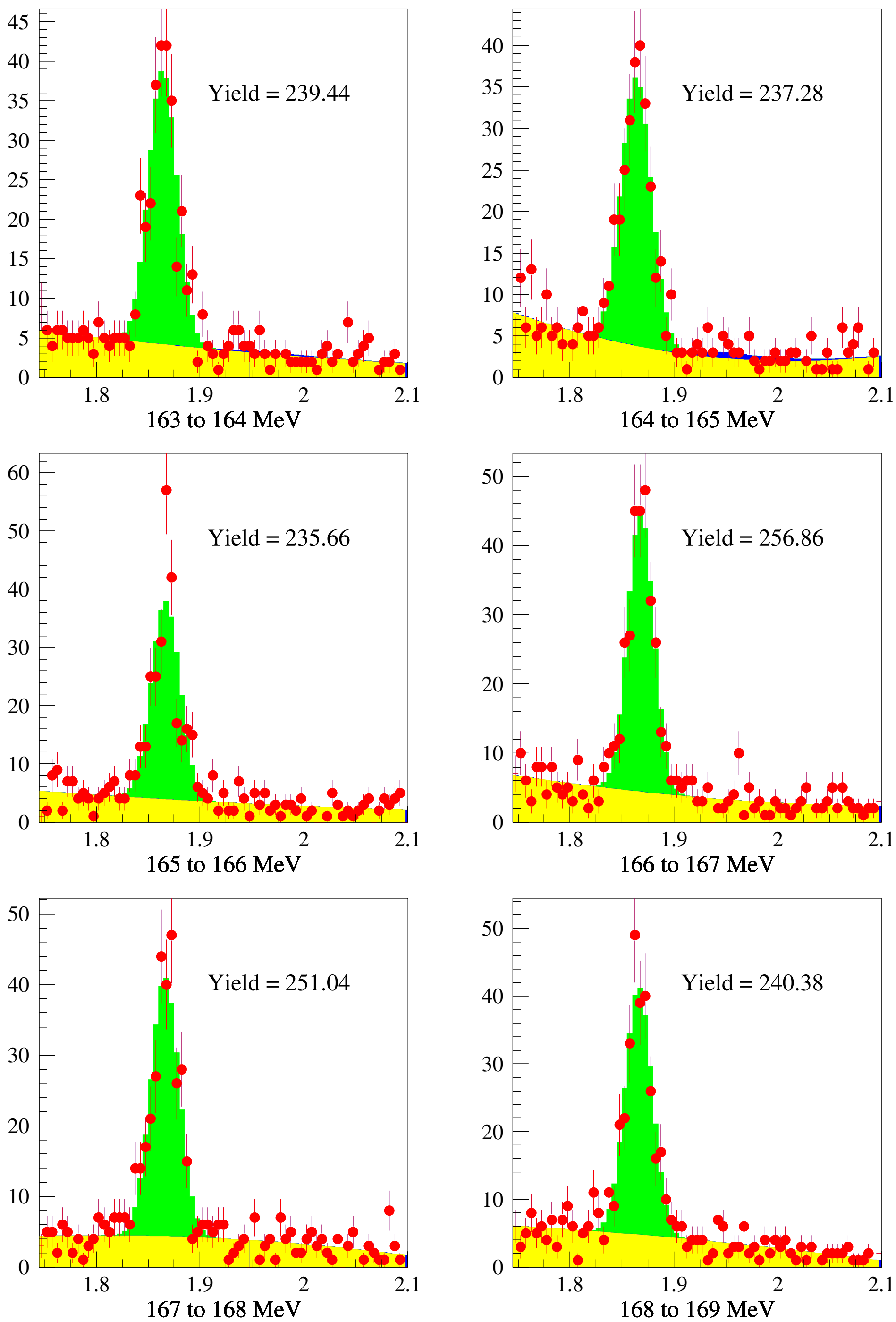

Yield = 239.44
163 to 164 MeV
Yield = 237.28
164 to 165 MeV
Yield = 235.66
165 to 166 MeV
Yield = 256.86
166 to 167 MeV
Yield = 251.04
167 to 168 MeV
Yield = 240.38
168 to 169 MeV

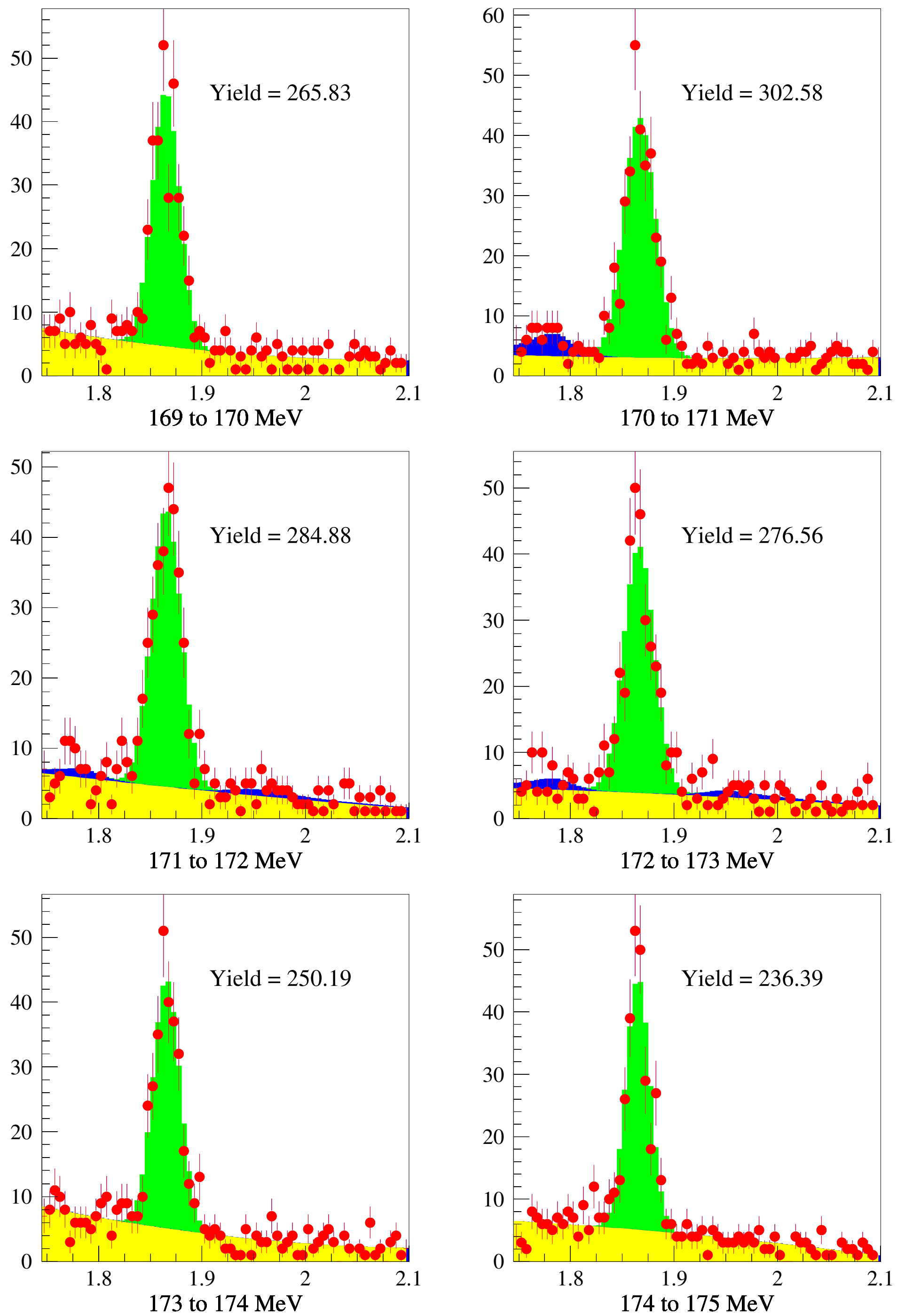
Yield = 265.83
169 to 170 MeV
Yield = 302.58
170 to 171 MeV
Yield = 284.88
171 to 172 MeV
Yield = 276.56
172 to 173 MeV
Yield = 250.19
173 to 174 MeV
Yield = 236.39
174 to 175 MeV

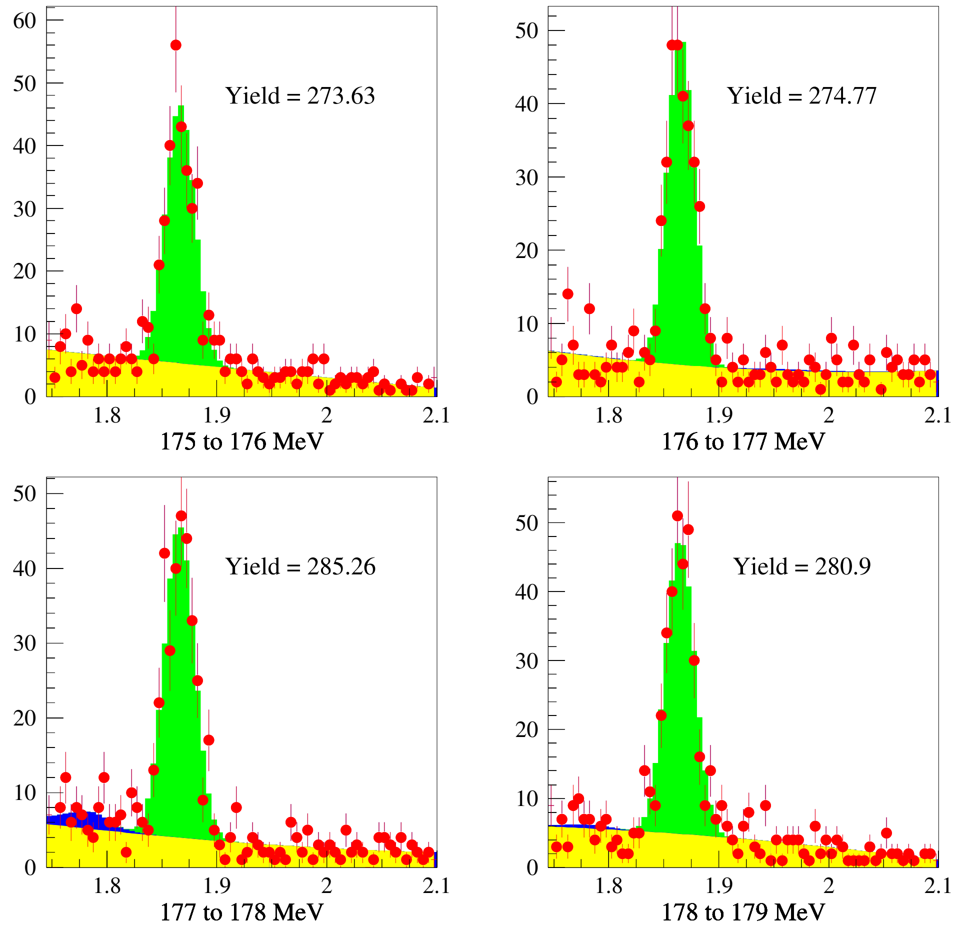

A.2 Right Sign Tagged Fits

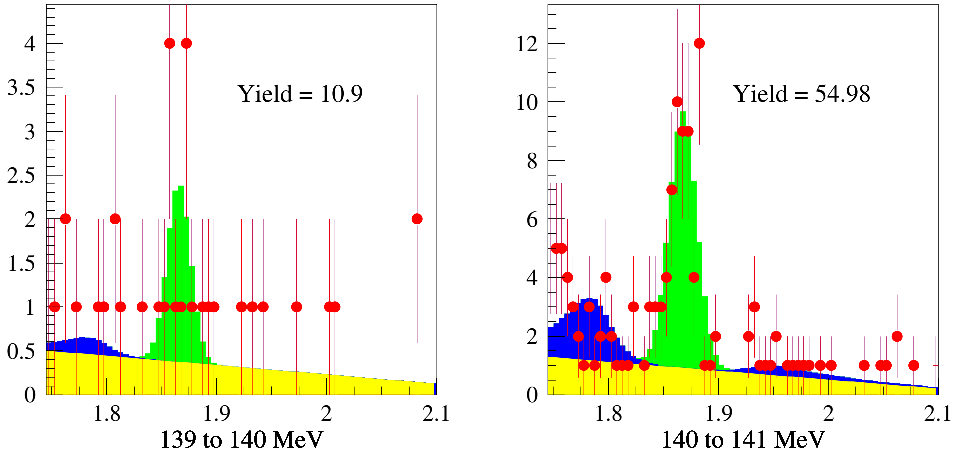

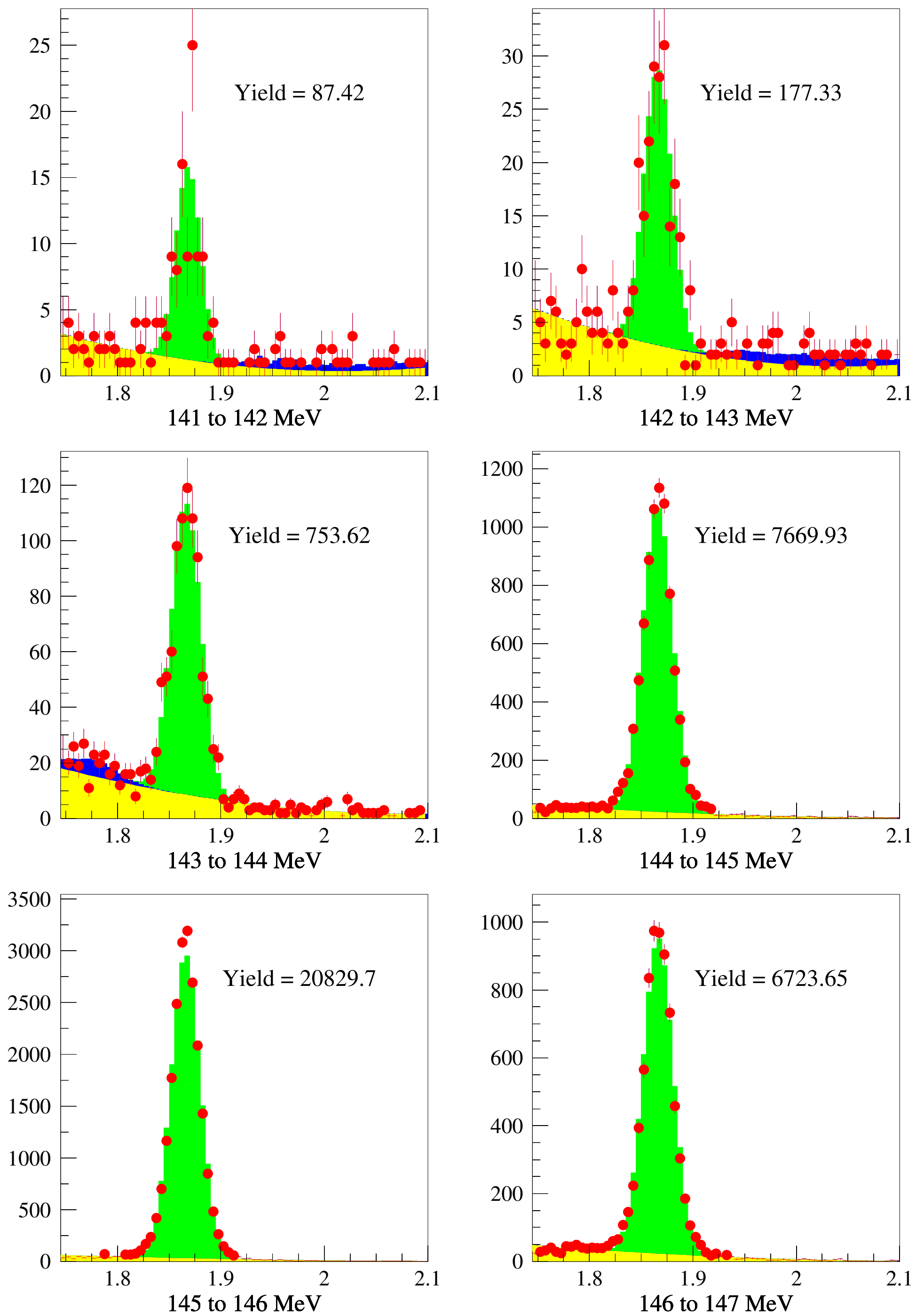
Yield = 87.42
141 to 142 MeV
Yield = 177.33
142 to 143 MeV
Yield = 753.62
143 to 144 MeV
Yield = 7669.93
144 to 145 MeV
Yield = 20829.7
145 to 146 MeV
Yield = 6723.65
146 to 147 MeV

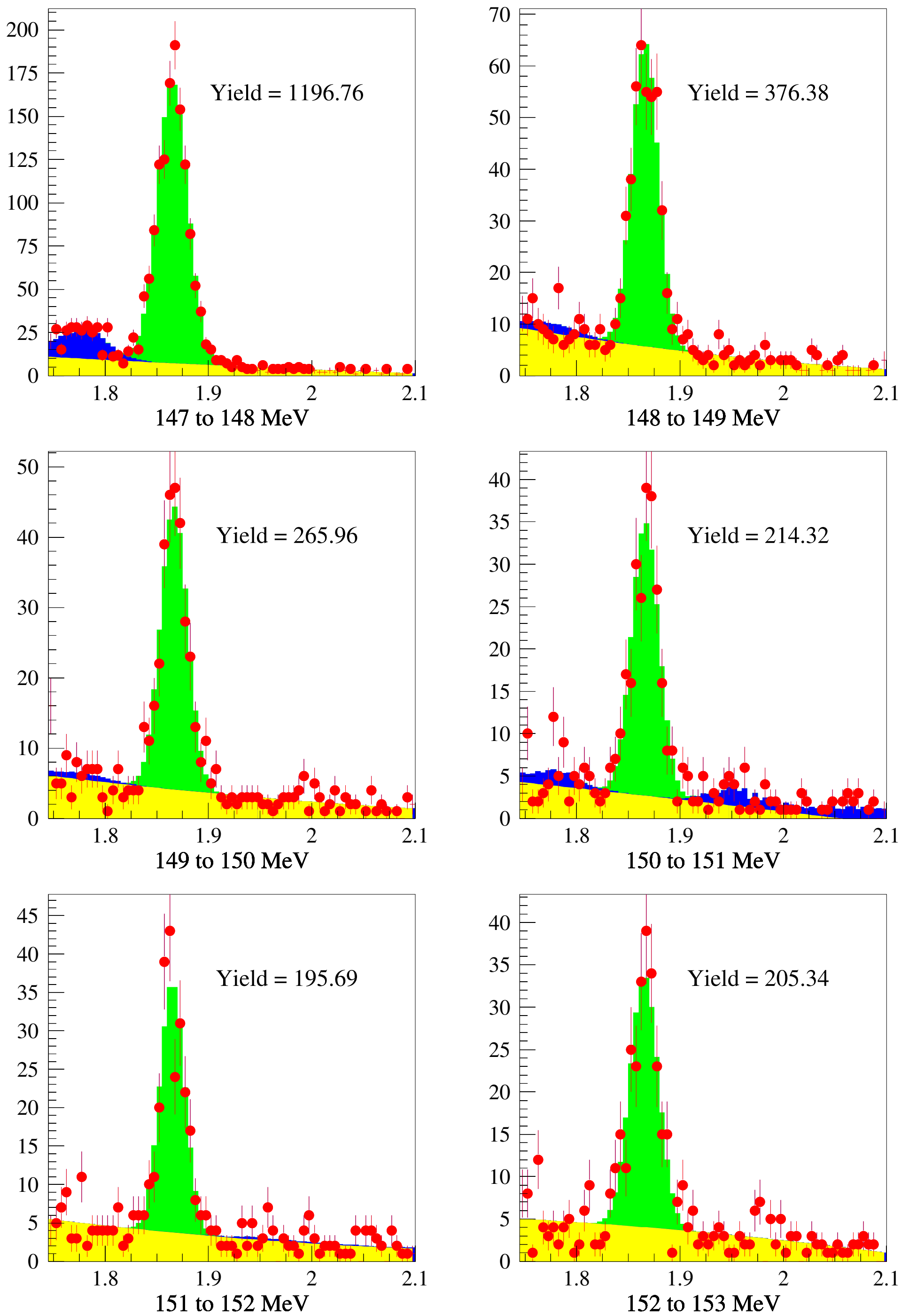
Yield = 1196.76
147 to 148 MeV
Yield = 376.38
148 to 149 MeV
Yield = 265.96
149 to 150 MeV
Yield = 214.32
150 to 151 MeV
Yield = 195.69
151 to 152 MeV
Yield = 205.34
152 to 153 MeV

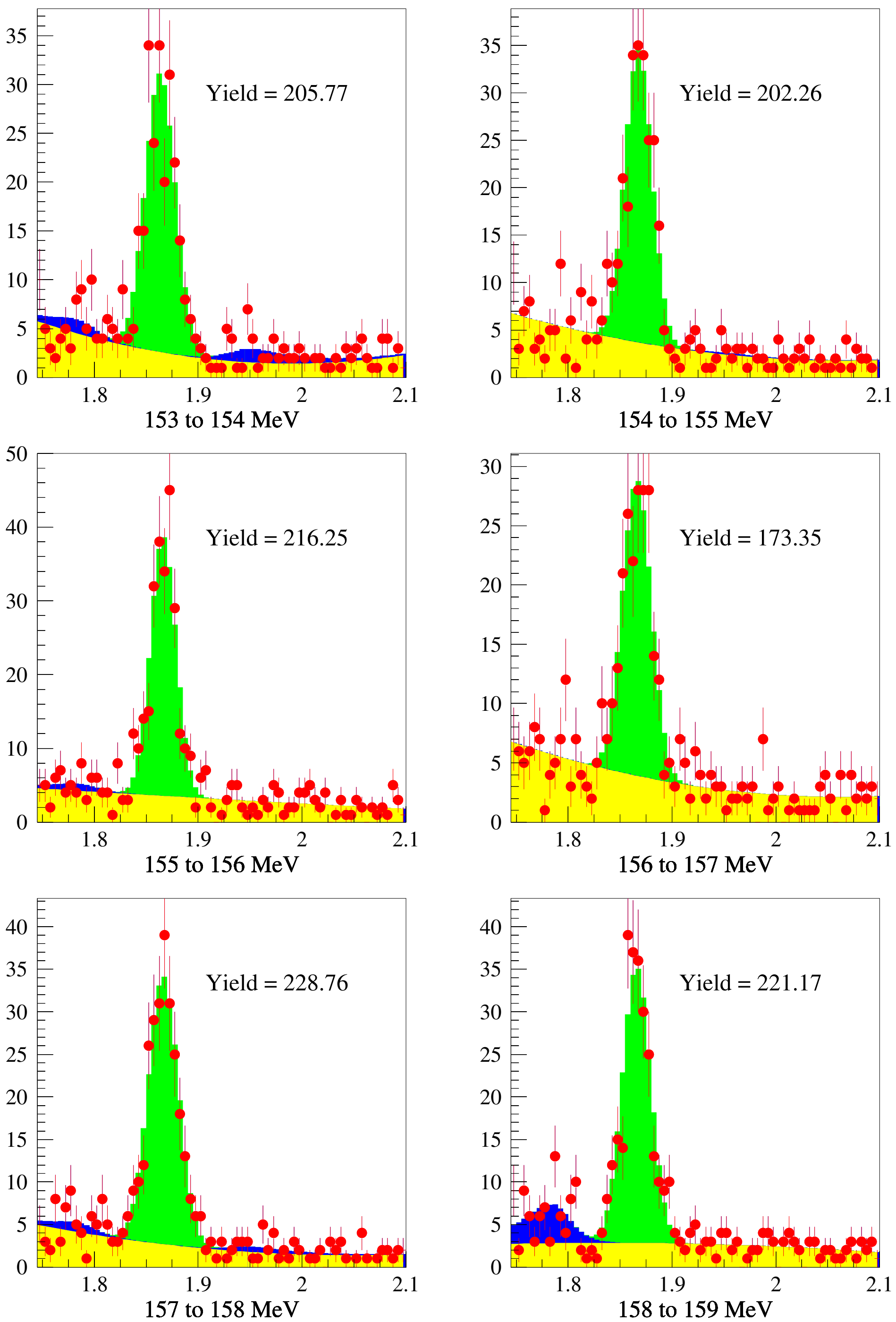
Yield = 205.77
153 to 154 MeV
Yield = 202.26
154 to 155 MeV
Yield = 216.25
155 to 156 MeV
Yield = 173.35
156 to 157 MeV
Yield = 228.76
157 to 158 MeV
Yield = 221.17
158 to 159 MeV
1.8
1.9
2
2.1

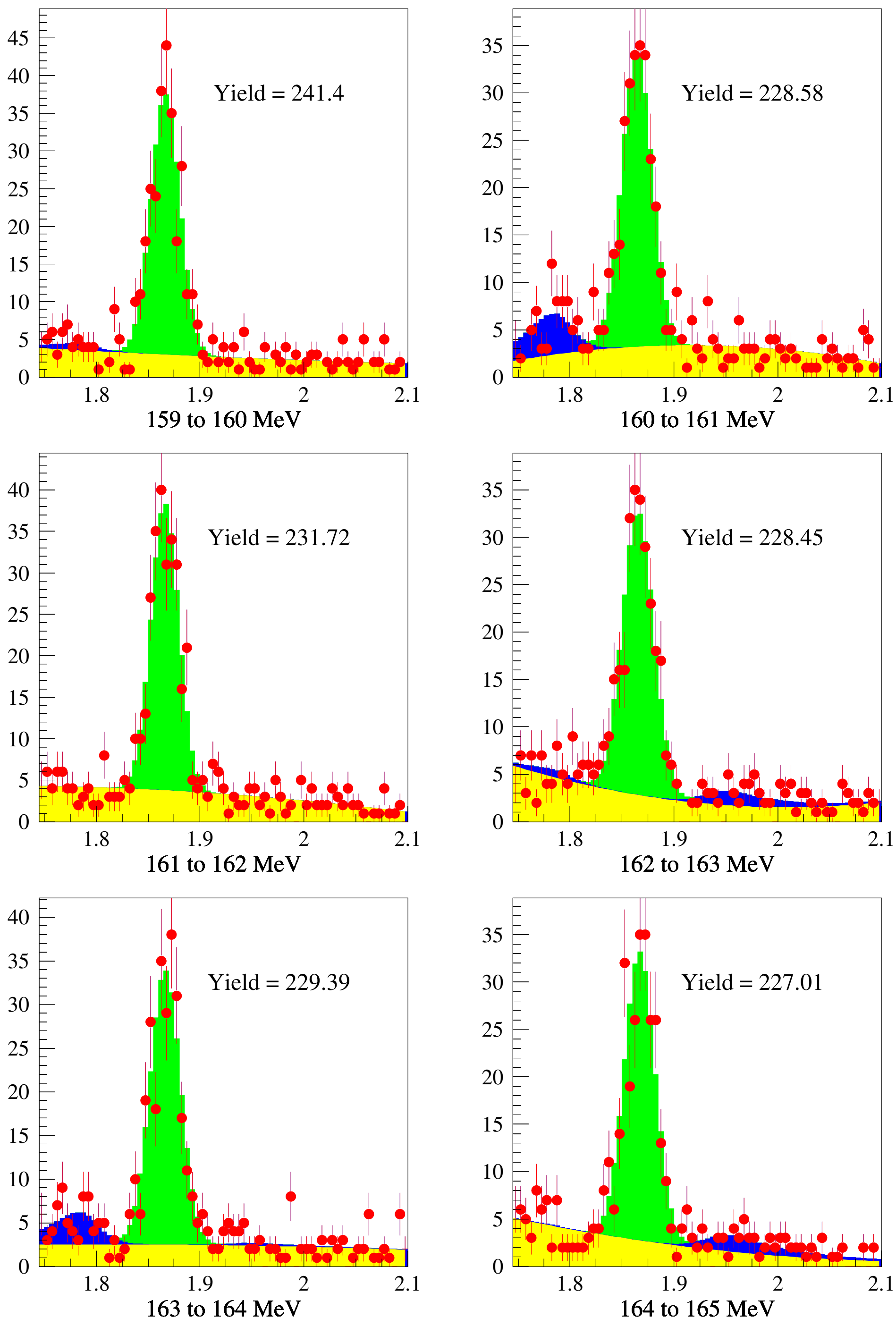
Yield = 241.4
159 to 160 MeV
Yield = 228.58
160 to 161 MeV
Yield = 231.72
161 to 162 MeV
Yield = 228.45
162 to 163 MeV
Yield = 229.39
163 to 164 MeV
Yield = 227.01
164 to 165 MeV
1.8
1.9
2
2.1

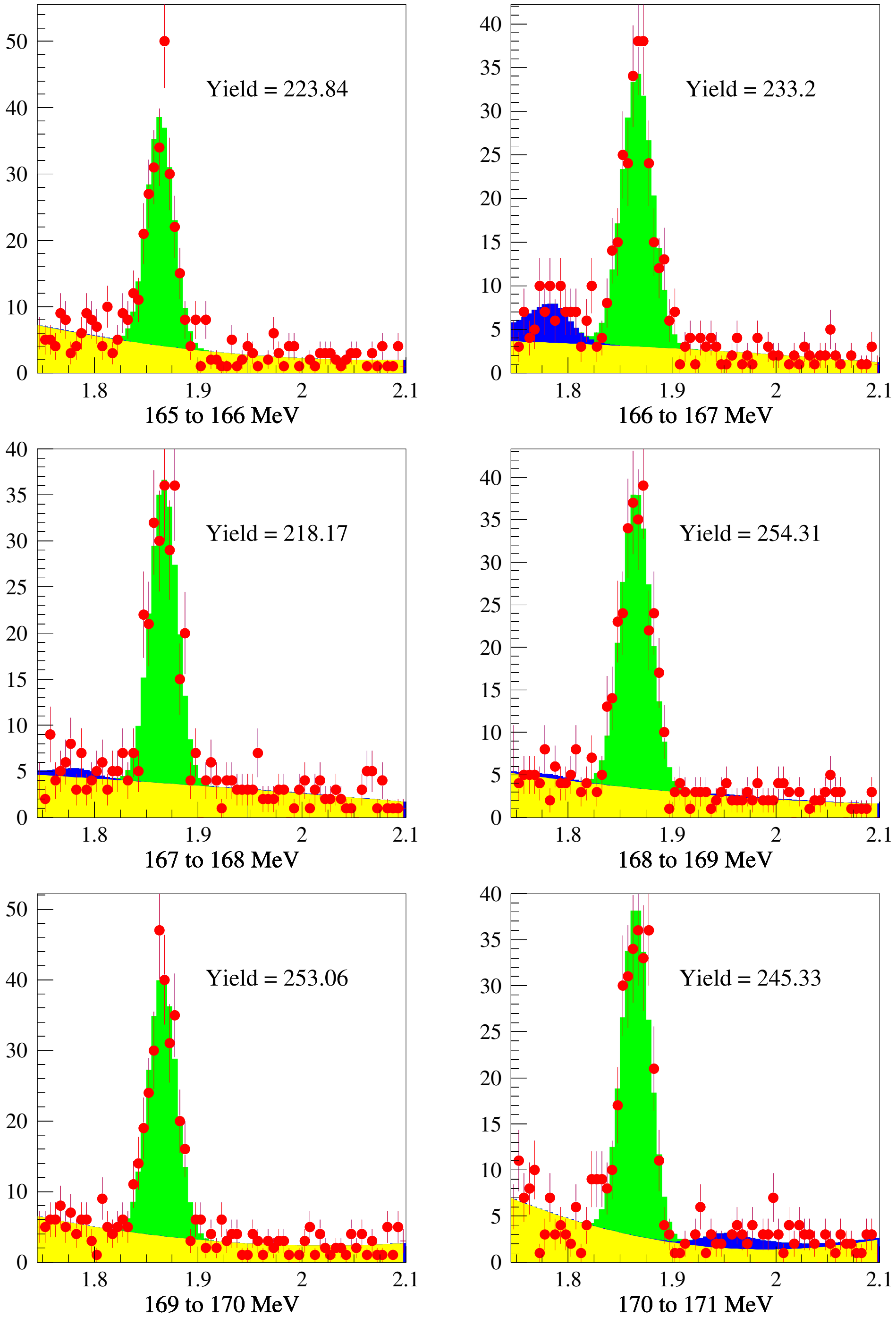
Yield = 223.84
165 to 166 MeV
Yield = 233.2
166 to 167 MeV
Yield = 218.17
167 to 168 MeV
Yield = 254.31
168 to 169 MeV
Yield = 253.06
169 to 170 MeV
Yield = 245.33
170 to 171 MeV

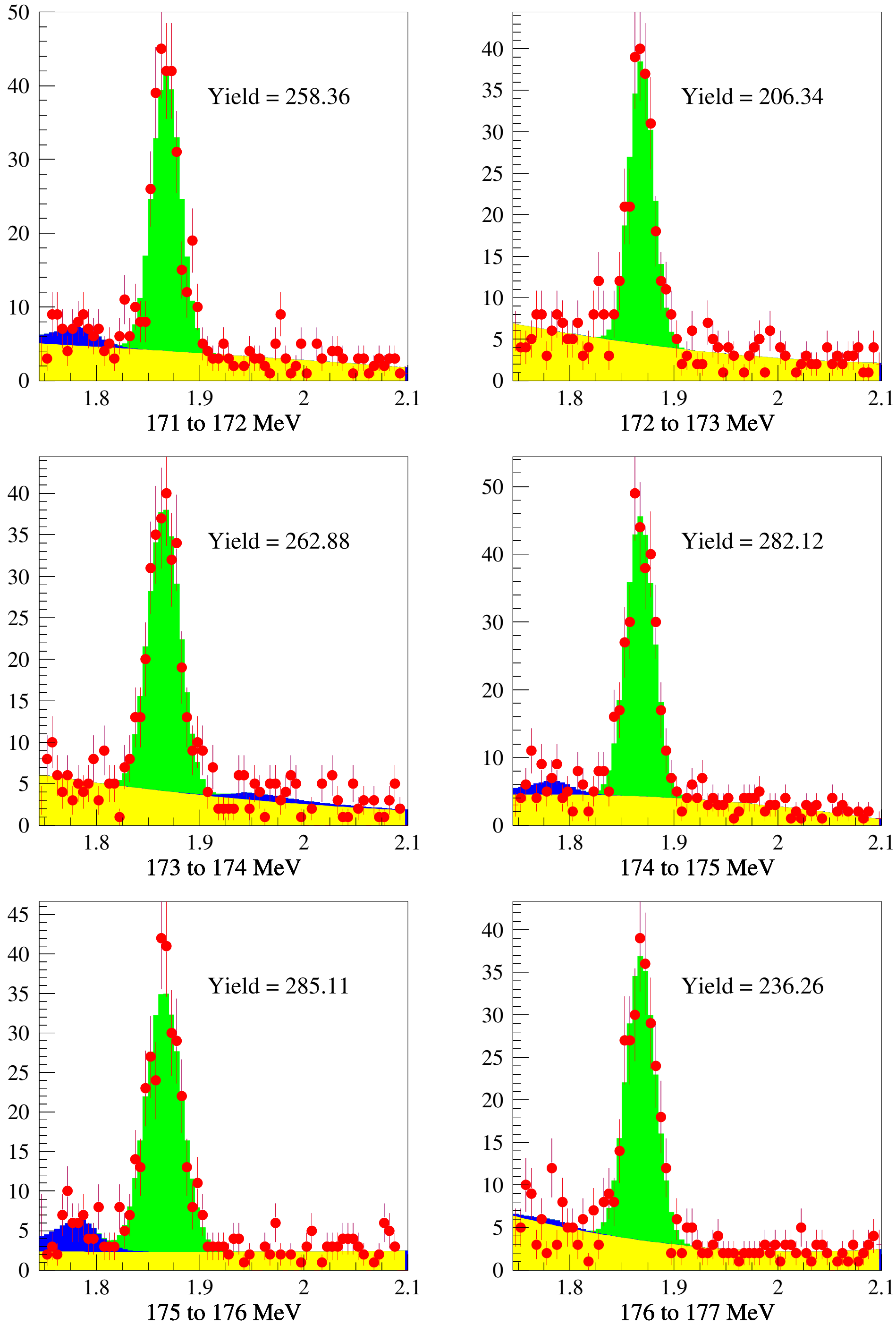
Yield = 258.36
171 to 172 MeV
Yield = 206.34
172 to 173 MeV
Yield = 262.88
173 to 174 MeV
Yield = 282.12
174 to 175 MeV
Yield = 285.11
175 to 176 MeV
Yield = 236.26
176 to 177 MeV

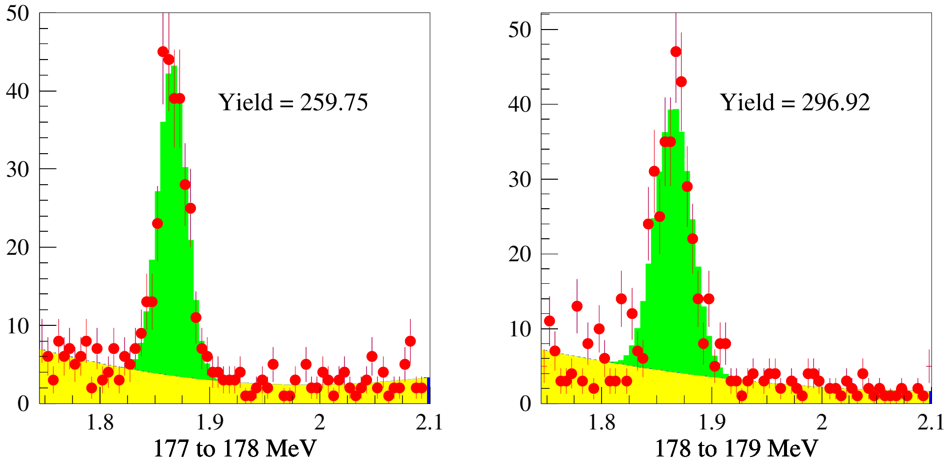

Yield = 259.75
177 to 178 MeV
Yield = 296.92
178 to 179 MeV

Bibliography

[1] S. L. Glashow, J. Iliopoulos, and L. Maiani, Phys. Rev. **D2**, 1285 (1970).

[2] N. Cabibbo, Phys. Rev. Lett. **10**, 531 (1963).

[3] P. L. Frabetti et al., Phys. Lett. **B359**, 403 (1995).

[4] D. Cinabro et al., Phys. Rev. Lett. **72**, 1406 (1994).

[5] E. M. Aitala et al., Phys. Rev. **D57**, 13 (1998).

[6] R. Barate et al., Phys. Lett. **B436**, 211 (1998).

[7] R. Godang et al., Phys. Rev. Lett. **84**, 5038 (2000).

[8] D. E. Groom et al., Eur. Phys. J. **C15**, 1 (2000).

[9] L. Moroni, First Results from FOCUS, in *Proceding of IECHEP*, 1999, Presented at the International Europhysics Conference on High Energy Physics, Tampere, Finland 1999.

[10] M. Kobayashi and T. Maskawa, Prog. Theor. Phys. **49**, 652 (1973).

[11] L. Wolfenstein, Phys. Rev. Lett. **51**, 1945 (1983).

[12] A. Pais and S. B. Treiman, Phys. Rev. **D12**, 2744 (1975).

[13] J. M. Link et al., Phys. Lett. **B491**, 232 (2000).

[14] A. Datta and D. Kumbhakar, Z. Phys. **C27**, 515 (1985).

[15] M. K. Gaillard and B. W. Lee, Phys. Rev. **D10**, 897 (1974).

[16] L.-L. Chau, Phys. Rept. **95**, 1 (1983).

[17] L. Wolfenstein, Phys. Lett. **B164**, 170 (1985).

[18] J. F. Donoghue, E. Golowich, B. R. Holstein, and J. Trampetic, Phys. Rev. **D33**, 179 (1986).

[19] H. Georgi, Phys. Lett. **B297**, 353 (1992).

[20] T. Ohl, G. Ricciardi, and E. H. Simmons, Nucl. Phys. **B403**, 605 (1993).

[21] H. N. Nelson, Compilation of $D^0-\overline{D}^0$ Mixing Predictions, An unpublished guide to $D^0-\overline{D}^0$ mixing predictions, 1999.

[22] G. Blaylock, A. Seiden, and Y. Nir, Phys. Lett. **B355**, 555 (1995).

[23] I. I. Bigi and A. I. Sanda, *CP Violation*, Cambridge University Press, 2000.

[24] L. Wolfenstein, Phys. Rev. Lett. **75**, 2460 (1995).

[25] A. F. Falk, Y. Nir, and A. A. Petrov, JHEP **12**, 019 (1999).

[26] T. E. Browder and S. Pakvasa, Phys. Lett. **B383**, 475 (1996).

[27] L.-L. Chau and H.-Y. Cheng, Phys. Lett. **B333**, 514 (1994).

[28] F. Buccella, M. Lusignoli, G. Miele, A. Pugliese, and P. Santorelli, Phys. Rev. **D51**, 3478 (1995).

[29] I. Hinchliffe and T. A. Kaeding, Phys. Rev. **D54**, 914 (1996).

[30] G. Goldhaber et al., Phys. Lett. **B69**, 503 (1977).

[31] T. T. Liu, (1995), Presented at Tau Charm Factory Workshop, Argonne, IL, Jun 21-24, 1995. In *Argonne 1995, Tau/Charm Factory* 447-480.

[32] E. M. Aitala et al., Phys. Rev. Lett. **77**, 2384 (1996).

[33] J. M. Link et al., Phys. Lett. **B485**, 62 (2000).

[34] S. Bergmann, Y. Grossman, Z. Ligeti, Y. Nir, and A. A. Petrov, Phys. Lett. **B486**, 418 (2000).

[35] P. Frabetti et al., Nucl. Instrum. Methods **A329**, 62 (1993).

[36] P. Kasper, R. Currier, P. Garbincius, and J. Butler, Wide Band to 'Double Band' Upgrade, Technical Report TM-1552, Fermilab, 1988.

[37] S. Bianco et al., The Upgraded Outer EM Calorimeter of FOCUS at Fermilab, in *Lisbon 1999, Calorimetry in high energy physics*, pages 527–541, 1999.

[38] V. Arena et al., Nucl. Instrum. Meth. **A434**, 271 (1999).

[39] H. W. Cheung, Proposal for a Programmable MG Module for FOCUS/E831, FOCUS Internal Memo, 1995.

[40] A. Kreymer and F. Prelz, DAQ Architecture for E831, FOCUS Internal Memo, 1997.

[41] C. Cawlfield, M. Ruesnink, and J. Wiss, Muon Identification χ^2 Confidence Levels, FOCUS internal memo, 1994.

[42] M. G. Hosack, Confidence Level for Outer Muons, FOCUS internal memo, 1998.

[43] M. Fausey et al., CPS and CPS Batch Reference Guide, Technical Report GA008, Fermilab, 1992.

[44] C. Caso et al., Eur. Phys. J. **C3**, 1 (1998).

[45] F. James, MINUIT Function Minimization and Error Analysis, Program Library Long Writeup D506, CERN, 1994, Version 94.1.

[46] P. R. Bevington and D. K. Robinson, *Data Reduction and Error Analysis for the Physical Sciences*, McGraw-Hill, Inc, 1992.

[47] E. Golowich and S. Pakvasa, Phenomenological Issues in the Determination of $\Delta\Gamma_D$, hep-ph/0102068, 2001.